FIELD-PROGRAMMABLE MICROFLUIDIC TEST PLATFORM FOR POINT-OF-CARE DIAGNOSTICS

A Thesis Submitted to the College of

Graduate Studies and Research

In Partial Fulfillment of the Requirements

For the Degree of Doctor of Philosophy

In the Department of Electrical and Computer Engineering

University of Saskatchewan

Saskatoon

By

Gary Wang

© Copyright Gary Wang, November, 2013. All rights reserved.

PERMISSION TO USE

In presenting this thesis in partial fulfilment of the requirements for a Postgraduate degree from the University of Saskatchewan, I agree that the Libraries of this University may make it freely available for inspection. I further agree that permission for copying of this thesis in any manner, in whole or in part, for scholarly purposes may be granted by the professor or professors who supervised my thesis work or, in their absence, by the Head of the Department or the Dean of the College in which my thesis work was done. It is understood that any copying or publication or use of this thesis or parts thereof for financial gain shall not be allowed without my written permission. It is also understood that due recognition shall be given to me and to the University of Saskatchewan in any scholarly use which may be made of any material in my thesis.

Requests for permission to copy or to make other use of material in this thesis in whole or part should be addressed to:

Head of the Department of Electrical and Computer Engineering
57 Campus Drive
University of Saskatchewan
Saskatoon, Saskatchewan
Canada S7N 5A9

ABSTRACT

Early work in electrowetting on dielectric (EWOD) devices has demonstrated their great potential in microfluidics; however, further work is needed to integrate EWOD technology into a system deployable for point-of-care (POC) diagnostics. This research is aimed at providing enabling technologies that foster a development path of EWOD devices using a process similar to the development of application-specific integrated circuits (ASICs). A field-programmable lab-on-a-chip (FPLOC), which allows designers to electrically program the prefabricated chip into EWOD applications, was fabricated and demonstrated based on novel microelectrode dot array (MEDA) architecture. The MEDA architecture proposes a standard EWOD component called "microelectrode cell", which can be dynamically configured into microfluidic components to perform microfluidic operations of the biochip. The FPLOC is the first EWOD biochip fabricated by the standard low-voltage complementary metal-oxide-semiconductor (CMOS) technology, which allows smooth on-chip integration of microfluidics and microelectronics. A total of 900 droplet detection electrical circuits were integrated into the chip and a real-time droplet location map could show shapes and locations of all droplets on the chip. The daisy-chained control structure of the MEDA architecture allowed individual control of 900 microelectrodes by only using three control pads. This control structure was also leveraged to add the built-in self-test (BIST), which was proven to be very useful in diagnosing the chip, of the FPLOC. The FPLOC successfully demonstrated seamless hierarchical field-programmability. Compared to conventional bottom-up and full-custom design approaches, the FPLOC brings microfluidic technology closer to POC diagnostics by providing biochip designers with CAD support at a level similar to that of the semiconductor industry, without the time-consuming and costly process of hardware design, testing, and maintenance.

ACKNOWLEDGMENTS

My first, and most earnest, acknowledgment must go to my supervisor, Dr. Daniel Teng. In every sense, none of my Ph.D. work would have been possible without him. I would like to express my deepest appreciation and gratitude to his encouragement and patient guidance, all the way from when I was considering applying to this Ph.D. program to the completion of this degree. Dr. Teng is the one professor who has truly made a difference in my ability to approach and to resolve research problems. His high scientific standards and unprejudiced attitude had a profound effect on me. His ability to adopt new concepts and to gain proficiency in new research interests influenced and motivated me. One simply could not have wished for a better or friendlier supervisor.

I am also deeply indebted to the members of the Ph.D. Advisory Committee, Dr. Ron Bolton, Dr. David Sumner, Dr. Catherine Niu and Dr. David Klymyshyn for their valuable advice, thought-provoking suggestions, and encouragement. In addition, I would like to thank my external examiner, Dr. Mu Chiao of University of British Columbia, who provided encouraging and constructive feedback.

I would also like to express my deeply-felt thanks to Dr. C. Y. Lee and Dr. Scott Feng of National Chiao-Tung University, Taiwan, who kindly allowed me to utilize their microfluidic labs and provided warm encouragement and help through the fabrications of the FPLOC.

I dedicate this work to

My father, King-Pong Wang,

My beloved mother, Jin-Shou Wu,

My wife, Judy Wang

For their absolute and infinite love, moral support and encouragements

and

My son, Derek Wang

To inspire him to be a great man

TABLE OF CONTENTS

LIST OF TABLES

LIST OF FIGURES

LIST OF ABBREVIATIONS

ASIC	Application-Specific Integrated Circuit
BIST	Built-In Self-Test
Bo	Bond number
CAD	Computer-Aided Design
CE	Capillary Electrophoresis
CerDIP	Ceramic Dual In-line Package
CMA	Configured Microelectrode Array
CMOS	Complementary Metal-Oxide-Semiconductor
CPU	Central Processing Unit
DAQ	Data Acquisition
DEP	Dielectrophoresis
DFF	D Flip-Flop
DFT	Design For Testability
DI	De-Ionized
DMFB	Digital Microfluidic Biochip
DNA	Deoxyribonucleic Acid
EDA	Electronic Design Automation
EDL	Electrical Double Layer
EWOD	Electrowetting On Dielectric
FPGA	Field-Programmable Gate Array
FPLOC	Field-Programmable Lab-On-a-Chip
HDL	Hardware Description Language
HIV	Human Immunodeficiency Virus

IC	Integrated Circuits
ITO	Indium-Tin-Oxide
LED	Light-Emitting Diode
LIF	Laser Induced Fluorescence
LOC	Lab-On-a-Chip
MEDA	Microelectrode Dot Array
MEMS	Micro Electro Mechanical Systems
MS	Mass Spectrometry
NAND	Not AND
NCTU	National Chiao-Tung University
NI	National Instruments
PCR	Polymerase Chain Reaction
PDMS	Polydimethylsiloxane
PFF	Pinched Flow Fractionation
POC	Point-Of-Care
PSA	Prostate-Specific Antigen
RPM	Revolutions Per Minute
SAR	Split-And-Recombine
SoC	System-on-Chip
SPICE	Simulation Program with Integrated Circuit Emphasis
SPR	Surface Plasmon Resonance
TFT	Thin-Film Transistor
TNT	Trinitrotoluene

TSMC	Taiwan Semiconductor Manufacturing Company
TSV	Through-Silicon Via
VLSI	Very-Large-Scale Integration
XOR	Exclusive OR
μTAS	Micro Total Analysis Systems

CHAPTER 1. INTRODUCTION

A lab-on-a-chip, or LOC, is a microfluidic device that scales multiple laboratory procedures down to a microchip format. LOC devices are essentially miniaturized laboratories that can perform simultaneous biochemical operations by using a very small amount of fluid from microliters to picoliters. The original concept of LOC devices came from "micro total analysis systems" (μTAS) proposed by analytical chemists for performing micro-volume chemistry on micro-scale devices [1]. It soon became obvious that the added value of μTAS was not limited to chemical analysis purposes. μTAS technologies are actually applicable to a wide range of applications. Therefore, researchers from other disciplines have also embraced μTAS technologies. The broader terms, microfluidics and LOC, are now commonly used in addition to μTAS. Interest in LOC, which has grown explosively over the last two decades, is reflected in the growing number of articles published, symposia and conferences [2, 3, 4, 5, 6, 7, 8, 9, 10]. Annual new publications are increasing steadily on top of almost 10,000 papers published over the last 10 years [11].

The first applications of microfluidics in the 1980s were triggered through the inkjet printers for computers. Lately, developments have been boosted by biotechnology [12]. LOC technology, specifically in the format of point-of-care (POC) diagnostic devices, is expected to grow into an essential part of the improvement effort of global health [13, 14, 15]. In developing countries, cost-effective POC diagnostic devices can become life-saving tools. POC diagnostics for the staging and monitoring of various diseases also has a profound impact on our healthcare systems. One of the most pervasive POC diagnostic devices is the blood glucose meter for diabetes patients. The glucose meter demonstrates how POC diagnostics can increase the quality of care by simplifying the monitoring of diseases. Typically, the change in concentrations of biomarkers is used in disease staging. Currently available POC diagnostic devices are almost exclusively

limited to qualitative detection of protein biomarkers [3]. There are many unmet needs for POC diagnostic capabilities for quantitative monitoring of disease-specific biomarkers: normally proteins, nucleic acids or cells [3]. Quantitative detection of these biomarkers requires more advanced methods fundamentally different from that of glucose measurements. For example, current POC diagnostic devices do not have the required amplification either of the signal or the target so they are not capable of checking targets present at low native concentrations (Table 1-1). These represent great opportunities for microfluidics, which is capable of performing reliable and accurate quantitative detection, specifically by developing user-friendly tests based on recent advancements in smaller, faster and fully integrated LOC devices [3].

1.1 The Development of Biochip and Microfluidics Technology

The term "biochips" refers to microarray biochips and microfluidic biochips [4, 16, 17]. Early biochips started with the concept of microarrays. A deoxyribonucleic acid (DNA) microarray is designed to evaluate thousands of DNA sequences simultaneously, and it is the most widely used biochip for genetic research. Microarray biochips cannot be reconfigured after manufacture. The scalability of microarray biochips is also limited by the complexity and the time required for microarray developments. Furthermore, microarray biochips cannot perform the sample preparation that is a very crucial function for field-deployable POC diagnostic devices [18].

Table 1-1. Classes of assays for POC diagnostics [3].

				Availability of POC products	
Class of Assays	Examples	Typical Concentration Range	Method of Detection	Qualitative	Quantitative
Chemistries	Glucose, HbA1c	µM - mM	Direct detection	Widespread	Widespread
Immunoassays	Troponin, PSA	fM - nM	Signal amplification	Widespread	Limited
Nucleic Acid Testing	HIV viral load	aM	Target amplification followed by signal amplification	Limited	Limited

Different from microarray biochips, microfluidic biochips are based on the basic idea that all required functions for biochemical applications are integrated into a single biochip using microfluidic technologies. Functions to be integrated include sample preparation, microfluidic operations, analyte-specific reaction and detection. Because of the full-integration nature, these microfluidic biochips are more salable and versatile than microarray biochips [18]. Two generations of microfluidic biochips have been developed so far. The first and most common microfluidic biochip is the continuous-flow microfluidic biochip [11]. The droplet-based microfluidic biochip is a new alternative that is positioned as state-of-the-art microfluidics [12].

1.1.1 Continuous-Flow Microfluidics

Continuous-flow microfluidic biochips are closed-channel and continuous-flow microfluidic systems. Conceptually, they are essentially resulting from macroscopic devices that consider the special needs brought by the reduction of the dimensions and the physical changes due to the influence of the solid walls. The manipulation of continuous liquid flow is typically implemented by integration of micromachined mechanical micropumps and microvalves [2], using external pressure sources [19], or electrokinetic mechanisms [20]. Continuous-flow microfluidic biochips are mainstream solutions for numerous well-established and less-complicated biochemical applications, but they might not be suitable for more complex applications that require complicated microfluidic manipulations, high configurability and flexibility [18, 21]. Nonetheless, complex continuous-flow microfluidic biochips, which contain very complex channel networks with hundreds of chambers and thousands of microvalves, have been reported by Thorsen et al. [19].

1.1.2 Droplet-Based Microfluidics

Droplet-based microfluidics manipulates discrete droplets rather than continuous liquid streams. Samples and reagents are divided into picoliter to nanoliter sized droplets to perform

microfluidic operations. Currently, there are two main platforms for droplet-based microfluidics: segmented flow microfluidics and droplet-based microfluidics. Droplets of segmented flow microfluidics are generated by dispensing the reagents into individual droplets surrounded by an immiscible liquid phase. These droplets are typically formed by co-flow in a capillary format and T-Junction or flow focusing in a planar chip format [22]. These systems are capable of performing most of the essential lab procedures [22, 23, 24], and they have been utilized in a variety of applications such as polymerase chain reaction (PCR) [25], protein expression [26], synthetic biology [27] and cell assays [28].

Droplet-based microfluidics is based on the concept that the liquid is divided into discrete droplets which can be independently actuated. These independently controllable droplets can be actuated to move in channels or on solid substrates [29, 30, 31, 32]. By manipulating discrete unit-volume droplets, which is therefore termed ‘‘digital microfluidics”, microfluidic functions can be mapped into a set of common microfluidic operations: e.g. creating, transport, cutting and mixing. In the literature, many droplet manipulating methods for droplet-based microfluidics have been proposed. These methods can be categorized as electrical, chemical, thermal, acoustical, opto-electrowetting, and magnetic methods. Among all methods, electrical techniques to actuate droplets have gained substantial interest in recent years [10, 33]. There are two main electrical droplet actuation methods: electrowetting on dielectric (EWOD) and dielectrophoresis (DEP). Both methods utilize an electric field across the droplet and the solid substrate to create electrostatic forces on the droplet to actuate droplets. The frequency of the applied electric field has a crucial impact on the induced droplet actuation force. The electric field redistribution through the droplet is frequency dependent and can result in either an EWOD or DEP force. To distinguish between EWOD and DEP forces, a critical actuation frequency f_c is typically used.

For low frequency actuations ($f << f_c$), only EWOD forces are induced. While in high frequency actuations ($f >> f_c$), DEP forces are induced [34, 35]. In addition, DEP typically requires much higher actuation voltages than EWOD. EWOD typically required the actuation voltage in the range of 11 to 100 V [36, 37, 38], but DEP would need a 50-to-200 V actuation voltage [39, 40, 41].

The electrowetting mechanism, especially in the configuration of EWOD, is a versatile tool in microfluidics because it enables control over fluid shape and flow through the use of electrical signals alone [29, 42, 43, 44]. For their simplicity and configurability, EWOD microfluidics have been implemented in a wide range of LOC applications including PCR amplification [45], immunoassays [46], enzyme assays [47], proteomics [48, 49], immunoassays [50], DNA-based applications [15], cell-based assays [51] and tissue engineering [52].

1.1.3 Electrowetting on Dielectric Microfluidics and Digital Microfluidic Biochip

Electrowetting-on-dielectric refers to physics describing electric forces caused by an electric field on the interface between a droplet and an electrode separated by a dielectric layer. By applying the electric field to the activated electrode and the droplet, an imbalance of the EWOD actuation force on the droplet can be formed. If this actuation force gradient is strong enough, it causes the droplet to move. More details about the EWOD actuation are covered in Chapter 2.

The term, digital microfluidic biochip (DMFB), is used specifically for the EWOD microfluidic device. A typical DMFB consists of two parallel plates. The droplet and the filler medium are sandwiched between the plates as indicated in Figure 1.1(a). Individually controllable electrodes are patterned on the bottom plate, and a continuous ground electrode is coated on the top plate. Glass substrates and transparent electrodes, which are formed by a material like indium tin oxide (ITO), are used to make the DMFB compatible with observation from a microscope. A dielectric layer is added on the bottom plate to separate the droplet and the

electrode array. A thin hydrophobic layer (e.g. Teflon AF1600) is coated on both plates to decrease the wettability of plate surfaces. To move a droplet by EWOD actuation, an electric potential is applied to activate the electrode at the leading edge of the droplet while other electrodes are deactivated (Figure 1.1(a)). By controlling activations of electrodes, droplets can be actuated to move along the electrodes. In the EWOD working range, speeds of actuated droplets increase with higher driving electric potential, and EWOD actuated droplets can reach the speed of 25 cm/s [30, 53, 54]. Figure 1.1(b) illustrates a fabricated DMFB designed for multiplexed bioassays [21].

In EWOD microfluidics, the droplet volume, which is decided by the size of the electrode and the gap height, defines the basic liquid unit for the microsystem. A microfluidic function is then mapped into a sequence of basic unit microfluidic operations, which are performed by specific designed microfluidic components. This ‘‘digitization’’ method facilitates the hierarchical architecture because biochip functions can be converted into basic unit microfluidic operations, and basic unit microfluidic operations can be accomplished with basic unit microfluidic components [18].

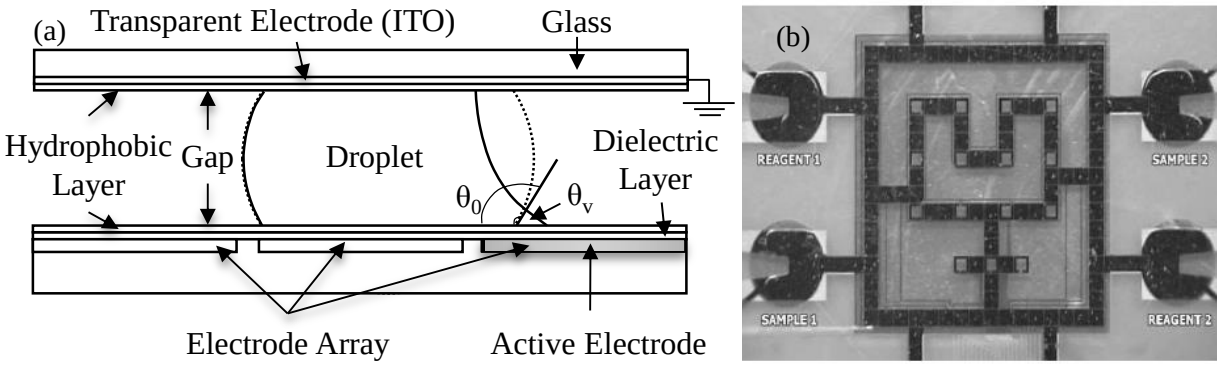

Figure 1.1. (a) The illustration of the structure of a DMFB (not to scale). (b) A fabricated DMFB designed for multiplexed bioassays [21] – Reproduced by permission of The Royal Society of Chemistry.

The DMFB offers promising capabilities for the future. The next step for the DMFB involves all major scientific and engineering disciplines including engineering (electrical, biomedical, mechanical and chemical), chemistry, physics, biology, computer science and manufacturing technology. In order to have a broader impact, the DFMB technology must turn into a commercial success. The impact of the DMFB will become apparent only when the general public can benefit from it. Among the potential applications of DMFBs, the commercialization of POC diagnostic devices is a much-discussed application [3]. The DMFB test needs to offer concrete value over centralized-lab testing for users who are not experts in microfluidics, such as police officers, field biologists, environmental scientists, and clinicians [55]. The POC format is particularly suitable for routine operation by untrained personnel. To convince these users to adopt DMFBs in their work, researchers must show values of DMFBs through improved quality-of-care, improved ease-of-use, and cost reduction. It is important to understand that the baseline analytical performance and the cost structure of the test are well established by centralized laboratories. Besides, there are drawbacks of DMFBs such as clinical practice changing and compliance with local regulations. The benefits of the DMFB need to outweigh its challenges through not only just technical solutions but also business strategies [3]. In addition, it is also important to work with a manufacturing partner early in the DMFB development cycle to define fabrication technologies and processes needed to fabricate high volume commercial devices [55].

The expectation of DMFB analytical techniques is to achieve improved performance and throughput, lower detection limits and better selectivity, and using small sample volumes at lower cost. The efficient integration of on-chip detection mechanisms has been a major bottleneck. The success of the DMFB technology for chemical and biological assays will depend heavily on the development of on-chip detection technologies amenable to chip-level integration

[56]. In addition, integrated DMFB devices must link a patient to a POC testing result. Besides the on-chip integration of biosensing detectors, other biochip functions such as sample collection, sample pre-treatment, sample preparation, analyte-specific reaction and result reporting should also be integrated into the devices. If true lab-on-a-chip systems are not feasible, compatible components must be designed for system integration [3].

1.2 Research Motivations and Objectives

Motivations and objectives of this research are strongly tied to the future trends of the DMFB. The integration of microelectronics and microfluidics through complementary metal-oxide-semiconductor (CMOS) technology provides one of the best ways to integrate advanced detection technologies into DMFB systems. CMOS technology is a good candidate for manufacturing DMFBs, especially the mass production of future fully integrated DMFBs or POC diagnostic devices. In addition, to speed up the development of future microfluidic systems, system wide top-down design automation and simulations will be essential. Different computer-aided design (CAD) tools and field-programmable devices will also likely happen along the advances of future DMFB developments.

1.2.1 Research Motivations

Motivated by the analogy and compatibility between DMFBs and digital integrated circuits, the goal of this research is to provide enabling technologies that pave a possible path for future DMFB developments by copying the success of the development of digital integrated circuits. Figure 1.2 illustrates the development history of system-on-chip (SoC) and the field-programmable gate array (FPGA). The standard cell methodology is an application-specific integrated circuit (ASIC) design approach that is based upon a library of predefined cells. The standard cell approach enables the design abstraction that component physical layouts are encapsulated into abstract logic representations (such as XOR gates, NAND gates). The standard

cell methodology, along with semiconductor fabrication advances, has helped to scale ASICs from simple ICs (few thousand gates) to very complex SoC devices (multimillion gates). The FPGA is a programmable logic device that has the ability to configure the logic function by a designer after the fabrication process. FPGAs can be electrically programmed to implement all logical circuits and systems. FPGAs have become one of the key digital circuit implementation tools based on their flexible field-programmability, fast turnaround time and low non-recurring engineering costs [57, 58]. Behind the ASIC and FPGA growth, the hierarchical top-down design approach and electronic design automation (EDA) tools enable larger scale IC and FPGA designs.

Traditionally, developments of DMFBs have been taking a bottom-up approach that discrete microfluidic components are designed and integrated together to perform a particular microfluidic application. Therefore, current DMFBs are typically developed by custom approaches instead of standard fabrication components and processes. The design complexity of future DMFBs will increase dramatically due to more concurrent bioassays, higher system integration and more sophisticated system control. In addition, time-to-market and mass

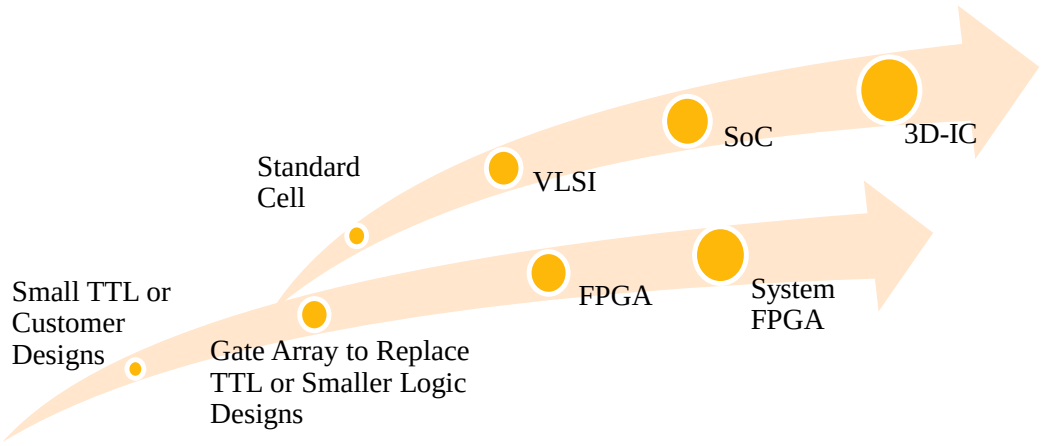

Figure 1.2. Development history of SoC. Standard cell architecture serves as the foundation of IC growth, and EDA tools enable large-scale IC design implementations (Courtesy of C.Y. Ho, VP of Synopsys).

production are also important design considerations for DMFBs. Current approaches in designing and fabricating DMFBs cannot scale well for these challenges. It is highly desirable to have a top-down design methodology, which has the same level of CAD support as the ASIC design, for DMFB developments. One viable solution will be a validated DMFB enabling technology that offers standard DMFB building elements to enable the top-down design automation for DMFB developments, similar to the gate array and the standard cell to the development of ASICs. The goal for this research is to provide the enabling technology to advance the development of DMFBs at least in the following areas:

1. The possibility to utilize low-voltage CMOS technologies to fabricate DMFB devices;
2. Large scale integration of microfluidics and microelectronics, and
3. Field-programmable DMFB.

1.2.2 Research Objectives

- Objective #1: To provide a validated DMFB enabling technology that could contribute to scale up the development of DMFBs, similar to the gate array and the standard cell to the development of ASICs.

The main objective for this research is to provide a new DMFB architecture as the enabling technology that offers standard DMFB building elements to enable the top-down design automation for DMFB developments.

- Objective #2: To construct a DMFB by low-voltage CMOS technologies.

One of the key success factors for the new DMFB architecture is that it can be realized by those fabrication technologies that can support the mass commercialization. Low-voltage CMOS fabrication technologies are well-established and commonly available. This objective is trying to identify and mitigate the technology gaps between DMFBs and low-voltage CMOS fabrication

technologies. The goal is to fabricate a DMFB based on the low-voltage CMOS technology to demonstrate the feasibility.

- Objective #3: To demonstrate integration of microfluidics and microelectronics based on CMOS technologies.

The success of DMFB technology for chemical and biological assays will depend heavily on the development of on-chip detection technologies amenable to chip-level integration. This objective is to demonstrate the integration of microfluidics and microelectronics by integrating detection circuitry into the chip.

- Objective #4: To demonstrate the field-programmable DMFB.

The field-programmable DMFB allows flexible implementations of DMFB applications by electrical programming. The field-programmability provides advantages much like well-established FPGAs. As a result, the field-programmable DMFB could present a compelling alternative for DMFB system implementations based on its flexible field-programmability, fast turnaround time and low non-recurring engineering costs. This objective is to demonstrate the seamless and easy configurations of microfluidic components and operations of the field-programmable DMFB by hierarchical software programming.

1.3 Research Methodology

To achieve the research objectives, the research work followed these main steps: (1) proposing a new DMFB architecture, (2) modeling and simulations of the new DMFB architecture, (3) proof-of-concept experiments of the new DMFB architecture, (4) CMOS fabrication technology selection, (5) design and fabrication of a field-programmable DMFB based on the new architecture, (6) system integration analysis, (7) system software development, (8) test system setup and system integration, and (9) validations and analyses of the field-

programmable DMFB. The steps were not all executed sequentially. Some steps were executed concurrently, and some steps took several iterations to complete. For example, the first generation system software was done for the test of ITO-glass prototypes, and a more complete version was revised for the CMOS-based DMFB validation. Overall, theoretical results and numbers were derived first, and then experiments were conducted to check whether the experimental results matched the theoretical predictions. If the process proved unsuccessful, then analyses, explanations or corrections were performed.

- Proposing a new DMFB architecture

The main works of proposing the new architecture were to define (1) the hierarchical structure of the new architecture, (2) the scaling design framework of the architecture, (3) the block diagram of the DMFB based on the architecture and CMOS fabrication technologies, (4) system software structure, (5) basic and advanced microfluidic operations based on the architecture, (6) design guidelines for standard DMFB building elements, and (7) system design guidelines.

- Modeling and simulations of the new DMFB architecture

The main purpose of modeling and simulations was to understand the EWOD actuation performance of the new DMFB architecture through theoretical analyses and numerical simulations. Crosschecking between theoretical analyses and numerical simulations was conducted to ensure the integrity of modeling and simulations. The simulated results became the predictions of microfluidic behaviors of the new architecture. This modeling was mainly used as a tool to understand the performance impact from the new architecture.

- Proof-of-concept experiments of the new DMFB architecture

To prove the concept of the new architecture, ITO-glass prototypes were fabricated to conduct extensive experiments for the architecture. Different levels of EWOD microfluidic operations

were performed to verify the microfluidic functionality of the architecture. Basic microfluidic operations, advanced microfluidic operations, and droplet motion performance experiments were performed mostly with deionized (DI) water with air as the filler medium. Silicone oil was also used as the filler medium for easier droplet actuation in situations of small gap heights and marginal actuation forces. Individually controllable DMFB building elements were fabricated for simple configuration tests. Configurations of standard DMFB building elements were simulated by grouping the elements together with thin hardwires. Predefined and fabricated hardwired configurations were used to perform most of the microfluidic operations.

- CMOS fabrication technology selection

Currently, no DMFB has been fabricated by low-voltage CMOS technologies because of the high-voltage requirement of EWOD droplet actuations. One of the research objectives is to demonstrate the feasibility of constructing the DMFB by the low-voltage CMOS technology. The objective set the priority on exploring the technology gap and possible solutions between low-voltage CMOS technologies and DMFB fabrications.

In addition, there are some identified issues for the CMOS-based DMFBs including incompatibility with optical detection (transparency), high cost, and size limitations [59]. For the optical transparency concern, if the CMOS sensing technology can be fully integrated into the DMFB, then the incompatibility with optical detection would not be an issue. The selection of the CMOS technology put a considerable amount of weight on the viability of on-chip detector integration. Also, when microelectronics and microfluidics integration advances the development of DMFBs into a higher level of complexity and sophistication that no current technologies can match, the cost model (including size limitations) for CMOS-based DMFBs will also be different.

Therefore, the selection of the CMOS technology also emphasized smooth integration of microfluidics and microelectronics.

- Design and fabrication of a field-programmable DMFB based on the new architecture

Main tasks for the DMFB design were (1) the EWOD actuation driver, (2) the implementation of standard DMFB building elements, and (3) on-chip detector integration. A new EWOD actuation driver based on the low-voltage CMOS technology was designed for the DMFB. In order to fully understand the technology gaps, the design and fabrication of the DMFB only used standard low-voltage CMOS technology and fabrication processes, including CAD tools, libraries, the die size and chip packaging. The implementation of the standard DMFB building element was taking the standard cell design approach, and the first step was to modularize the design. The scalability was the key design consideration of the standard DMFB building element. The strategy of detector integration was to integrate a one-bit detector into the standard DMFB building element as part of the microfluidic component for the demonstration of integration of microelectronics and microfluidics.

- System integration analysis

After the design of the field-programmable DMFB was completed, a system integration review was conducted to check the functional coverage of the DMFB. The goal was to make sure fundamental functional blocks were fully covered by the overall system design of the DMFB. If a true lab-on-a-chip microsystem is not feasible, compatible components would be designed for system integration

- System software development

The new architecture is a hierarchical architecture. The system software development was for the demonstration of the hierarchical architecture and the software support of operations of the

biochip. Also, the graphical programming language approach simplified the system software development, so National Instruments' graphical programming language LabVIEW was leveraged to develop the necessary system software.

- Test system setup and system integration

The test system setup was used to perform the system integration from both the hardware and software point of view. On the hardware side, the test fixture design and the droplet delivery mechanism were two main tasks. From the software point of view, software tools required by the test system were also demonstrations of the hierarchical programming and key functions of the field-programmable DMFB and the new architecture.

- The validations and analyses of the field-programmable DMFB

There were three main areas of validations for the field-programmable DMFB: (1) built-in self-test, (2) droplet actuation capability validation, and (3) droplet detection validation. The built-in self-test was implemented for the quick self-test of electrical circuits to ensure the integrity of the biochip. The droplet actuation capability validation was performed for the proof-of-concept test and analysis of the new EWOD actuation driver, which enabled the DMFB fabrication by using the low-voltage CMOS technology. The droplet detection validation was used to demonstrate the integrated droplet detector as well as integration of microelectronics and microfluidics.

CHAPTER 2. BACKGROUND

This chapter presents an overview of the theoretical framework, system structures and applications of DMFBs based on a review of the related literature. The aim of the first section is to provide the theoretical background of droplet EWOD actuations. DMFB operations depend heavily on microfluidic principles. Many of the physical principles are not new discoveries but the development of microfluidics brings new interest and attention. Lippmann discovered the electrowetting effect in 1875, and Berge revisited it to give the first demonstration of EWOD in 1993. The first section starts with the discussion of the droplet and then covers EWOD actuations, including different actuation models and the working range. The second section is devoted to the architecture of the DMFB. Furthermore, relevant applications of DMFBs are discussed in the third section.

2.1 Theoretical Framework

2.1.1 Theory of Droplet

Two types of droplets are most relevant in the study of DMFBs. One is the sessile droplet on a solid substrate and another is the droplet constrained between two parallel plates. These micro-scale droplets are governed by microfluidic principles such as surface tension, Bond number and Laplace's law. In the following subsections, these physical principles are discussed and concluded with an application example.

2.1.1.1 Surface Tension

Surface tension is responsible for the shape of droplets, so the discussion of droplets starts with it. Surface tension γ is a measurement of energy on the interface of two immiscible fluids, such as water and air, and it is caused by unbalanced intermolecular forces. Molecules at the surface of the droplet do not have neighbor molecules on all sides of them, and exhibit stronger cohesive forces on neighbor molecules on the surface. Surface tension usually is estimated from

the energy loss per unit area at the interface. Its dimension is energy per unit surface (J/m^2), or energy per unit length (N/m). If U is the total molecule cohesive energy per molecule, then the energy loss of a flat-interface molecule is half of the total molecule cohesive energy. If R is the molecular dimension, and R^2 is the surface area, then the surface tension is estimated [60] as

$$\gamma \approx \frac{U}{2R^2}. \tag{2-1}$$

One consequence of surface tension is that sessile droplets (Figure 2.1) will always have a shape as close as possible to a spherical cap to minimize surface areas. Another consequence is that it requires an adequate amount of energy to change the shape of the interface or to create a new interface, such as cutting a droplet by EWOD actuation.

Surface tension is typically represented by the symbol γ with capital subscripts for components forming the interface. For instance, a liquid-gas surface tension is indicated as γ_{LG}. Commonly, a liquid-gas interface uses "surface tension", and a liquid-liquid interface uses "interfacial tension". Sometimes, the subscripts are omitted for a liquid-air interface, or for situations without confusion. In addition, surface tension is temperature dependent. The temperature coefficient α is always negative for surface tension, which decreases with temperature.

2.1.1.2 Bond Number

The Bond number is a dimensionless number which indicates the relative importance of gravitational forces to surface tension. A droplet would have a spherical shape when the Bond number is far less than 1 that means the gravitational force is negligible. The Bond number (B_o) is defined by

$$B_O = \frac{\text{gravity}}{\text{surface tension}} = \frac{\Delta\rho g h^2}{\gamma}, \tag{2-2}$$

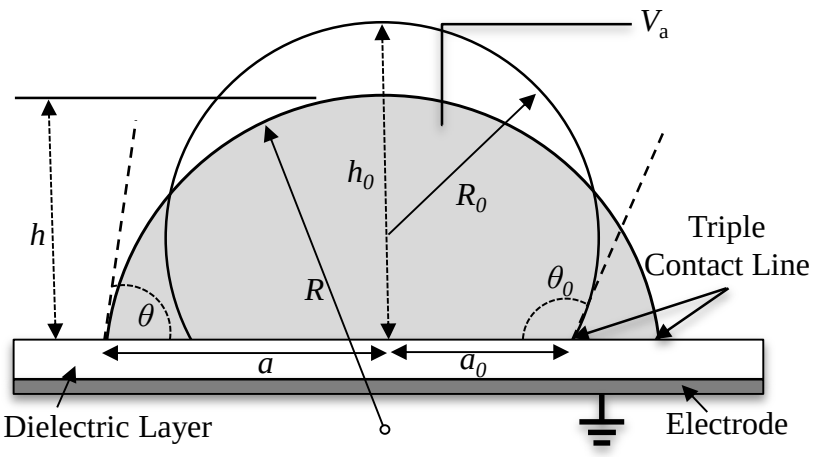

Figure 2.1. Side view of a sessile droplet which is small enough to have a spherical cap shape. Actuation voltage V_a deforms the droplet. Relations between geometrical quantities (V, h, a, R, and θ) can be yielded by the spherical cap shape and fixed volume V. Variables with the subscript 0 represent values of $V_a = 0$. (Image courtesy of Prof. T.B. Jones [33].)

where $\Delta\rho$ is the liquid-fluid density difference, g the gravitational acceleration, h the height of droplet, and γ the surface tension.

2.1.1.3 Sessile Droplet and Droplet Constrained Between Two Plates

In engineering applications, the interface of two immiscible fluids, such as water and air, is an ideal mathematical surface as indicated in Figure 2.1. The contact angle θ is the tangent line angle of the droplet surface on the triple-phase contact line. For h = 500 μm (Figure 2.1), which is typical in EWOD microsystems, the Bond number is about 0.03. Therefore, sessile drops in open EWOD microsystems can be assumed spherical. Figure 2.1 shows cross sections of sessile droplets, which are small enough to have spherical cap shapes, on non-wetting and wetting surfaces. A set of useful relationships between geometrical quantities (the volume V, the height h, the contact radius a, the curvature radius R, and the contact angle θ) of the droplet can be yielded [12, 33]

$$h = R(1 - \cos\theta), \tag{2-3}$$

$$V(a,h) = \frac{\pi}{6} h(3a^2 + h^2)\,, \tag{2-4}$$

$$R = \frac{a^2 + h^2}{2h}\,, \tag{2-5}$$

$$\cos(\theta) = \sqrt{1 - (a/R)^2}. \tag{2-6}$$

Among all geometrical quantities used in equations (2-3) to (2-6) for the spherical cap, the contact radius a is possibly the best choice for an electromechanical formulation because it reflects physical interface changes due to capillary and actuation forces of the contact line [33].

For a micro-scale droplet constrained between two parallel plates, the free surface, which is the surface area between the droplet and the filler medium, is also spherical (Figure 2.2). Therefore, the vertical radius *r* of the free surface is geometrically related to the contact angle of the top plate θ_t, the contact angel of the bottom plate θ_b, and the gap height *d* [61],

$$r_1 = \frac{-d}{cos\theta_t + cos\theta_{b1}}, \tag{2-7}$$

$$r_2 = \frac{-d}{cos\theta_t + cos\theta_{b2}}, \tag{2-8}$$

where the contact angle of the top plate θ_t is unchanged. The contact angle of the bottom plate θ_{b2} is decreased by the activation of the electrode on the bottom plate.

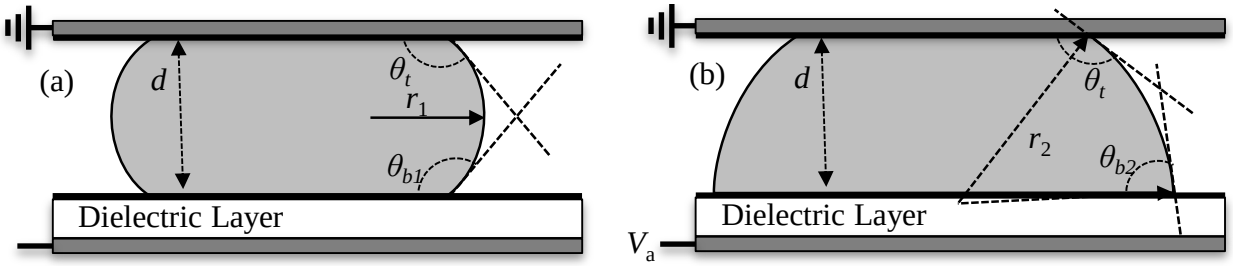

Figure 2.2. Droplets constrained between two parallel plates that are small enough to have spherical shapes for free surfaces: (a) non-actuated droplet; (b) actuated droplet.

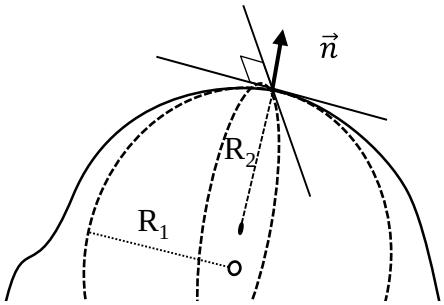

Figure 2.3. Schematic view of two radii R_1 and R_2 of principal curvatures of a surface.

2.1.1.4 Laplace's Law and Applications

2.1.1.4.1 Laplace's law

Laplace's law defines the relation between the pressure in a droplet and curvatures of the droplet, and it is fundamentally important in the study of droplet manipulations. For a two-dimensional curve, the osculating circle is the closest tangent circle at the given point of the curve. The curvature radius R is defined by the osculating circle radius. The curvature of the curve is the reciprocal of the radius

$$k = \frac{1}{R}. \tag{2-9}$$

Curvature can be positive (a convex curve) or negative (a concave curve). A surface is more complex than a curve because it has many curvatures at the given point of the surface. Among all surface curvatures, the most important ones are principal curvatures, which are the maximum and minimum curvatures of the surface point. The two planes for principal curvatures are always perpendicular to each other (Figure 2.3). The pressure change ΔP across the fluid interface, which is defined by two radii R_1 and R_2 of principal curvatures, is given by Laplace's law

$$\Delta P = \gamma \left(\frac{1}{R_1} + \frac{1}{R_2} \right). \tag{2-10}$$

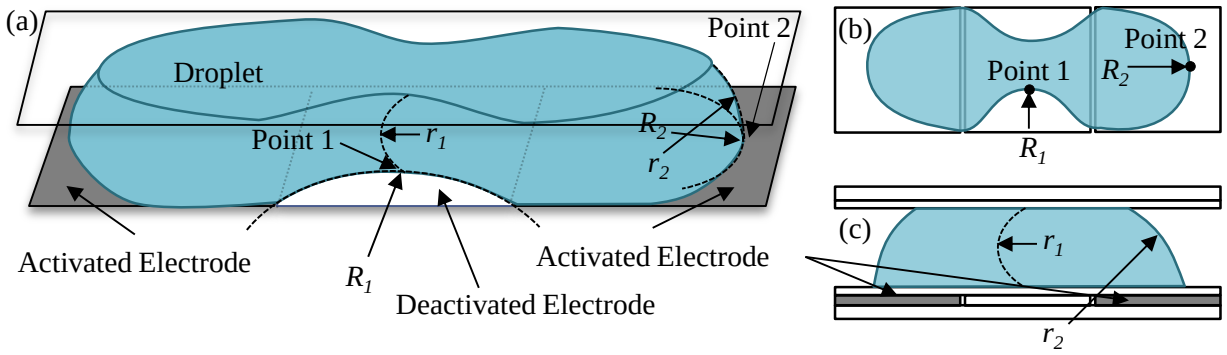

Figure 2.4. Sketches of cutting a droplet constrained between two parallel plates: (a) 3-D illustration; (b) top view; (c) side view.

Laplace's law introduces a very useful equation that can determine droplet internal pressures and interface changes in a droplet formation. An application of Laplace's law to analyze cutting a droplet constrained between two parallel plates is given in the next subsection.

2.1.1.4.2 Hydrostatic pressures of cutting a droplet constrained between two plates

Laplace's law can be used to study microfluidic operations of the DMFB. One basic microfluidic operation for the DMFB is three-electrode droplet cutting (Figure 2.4). Hydrostatic pressures at Point 1 and Point 2 in the droplet are given by Laplace's law,

$$P_1 - P_0 = \gamma\left(\frac{1}{R_1} + \frac{1}{r_1}\right), \tag{2-11}$$

$$P_2 - P_0 = \gamma\left(\frac{1}{R_2} + \frac{1}{r_2}\right), \tag{2-12}$$

$$P_1 - P_2 = \gamma\left(\left(\frac{1}{R_1} - \frac{1}{R_2}\right) + \left(\frac{1}{r_1} - \frac{1}{r_2}\right)\right), \tag{2-13}$$

where R_1 and r_1 are the two radii of principal curvatures at Point 1; R_2 and r_2 are the two radii of principal curvatures at Point 2; P_0 is the exterior pressure. When performing three-electrode droplet cutting, the deactivated middle electrode forms a hydrophobic band, and two outer activated electrodes form two hydrophilic bands. If $P_1 - P_2 > 0$, the droplet is stretched by two

hydrophilic bands and pinched by the hydrophobic band. The cross section of Point 1 can be viewed as Figure 2.2(a). Substitutions of r_1 and r_2 in equation (2-13) with contact angles and the gap height by using equations (2-7) and (2-8) result the droplet cutting equation

$$P_1 - P_2 = \gamma\left(\left(\frac{1}{R_1} - \frac{1}{R_2}\right) + \left(\frac{cos\theta_{b2} - cos\theta_{b1}}{d}\right)\right) > 0\,, \tag{2-14}$$

where R_1 is concave and negative. To satisfy equation (2-14), it requires a large contact angle change which means a large positive value of $(cos\theta_{b2} - cos\theta_{b1})$, a small gap d, and a large radius R_2. R_2 is mainly decided by the size of the electrode. Therefore, EWOD cutting can only be performed with appropriate gap heights and electrode sizes [61].

2.1.2 Theory of Electrowetting on Dielectric

Electrowetting refers to physics describing the spreading of a liquid onto a solid surface and the contact angle reduction induced by the electric force. Electrowetting on dielectric is an electrowetting configuration in which solid actuation electrodes are coated with a dielectric layer to separate them from the droplet [62, 63]. When an electric voltage is applied to an EWOD device, electric charges accumulate at the interface between the dielectric layer and the droplet. The interfacial electric charges couple the electric field to induce the interfacial electrostatic force. The density of the interfacial force is most strongly peaked at a very short distance above the contact line [10, 12]. The interfacial force deforms the droplet to cause the decrease of the contact angle at the contact line. For EWOD actuations, the thickness and material properties of the dielectric layer are the most important parameters because they decide the electric field distribution and associated EWOD actuation forces [10].

2.1.2.1 Lippmann-Young Equation

Electrocapillarity, which means the presence of electric charges causing a difference of the mercury capillary rise, was first observed in 1857 by Gabriel Lippmann [64]. He formulated a

theory of the electrocapillary effect with the famous Lippmann's equation. According to Lippmann's equation [64], the electric potential V across the liquid-solid interface can control the interfacial tension γ_{LS},

$$\gamma_{LS}(V) = \gamma_{LS}(V = 0) - \frac{C}{2}V^2 , \tag{2-15}$$

where C is the capacitance (F/m^2) of the dielectric layer. $\gamma_{LS}(V)$ is the interfacial tension with the applied voltage V, and $V = 0$ means no external voltage. Lippmann's equation contains the principle of EWOD. Berge pioneered the EWOD technique to actuate liquid droplets on solid substrates in the 1990s [62]. He combined Lippmann's equation and Young's equation to yield the Lippmann-Young equation. Young's equation describes the contact angle and the interfacial force balance at the triple-phase contact line (Figure 2.5),

$$\gamma_{LF}cos\theta + \gamma_{LS} - \gamma_{SF} = 0 , \tag{2-16}$$

where γ_{LF} is the liquid-filler-medium interface tension. By substituting (2-16) into (2-15) and replacing C with the capacitance formulation, the relation between the contact angle and the electric potential can be formulated as

$$\cos\theta(V) - \cos\theta_0 = \frac{\varepsilon_0\varepsilon}{2\gamma_{LF}t}V^2 , \tag{2-17}$$

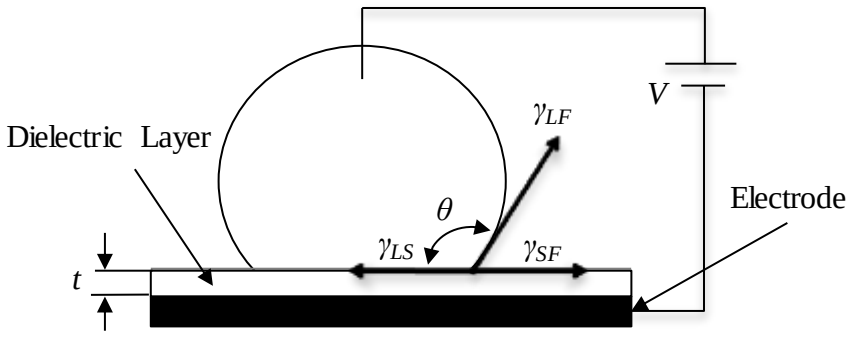

Figure 2.5. Principle of electrowetting on dielectric (EWOD)

where θ_0 is the V = 0 contact angle, ε_0 the vacuum permittivity, ε the dielectric constant and t the thickness of the dielectric layer. Equation (2-17) is the Lippmann-Young equation. The equation shows the relationship between the electrical energy at the liquid-solid interface and the interfacial energy at the liquid-fluid interface. The right-hand-side dimensionless electrowetting number of the equation expresses the amount of interfacial energy of the solid-liquid interface reduced. The implication of "V = applied voltage" is that the voltage drops within the liquid, such as electrical double layer (EDL), are negligible [10]. The phenomenon of the liquid-solid contact angle change induced by the applied voltage in EWOD actuation is apparent, and it has been quantified as a voltage-dependent variable $\theta(V)$. Nonetheless, it is important to be aware that the contact angle change is not the cause of the EWOD actuation or the spreading of the droplet. The contact angle change is merely a corresponding consequence of the interfacial electrostatic force acting on the droplet [33].

From equation (2-17), the applied voltage causes the contact angle change $\theta(V)$. In reality, from a closer look (Figure 2.6), the contact angle is still the Young contact angle θ_0 but not the Lippmann contact angle. However, at a very small distance (on the order of 1 μm) from the solid surface, the observed angle decreases to $\theta(V)$ given by the Lippmann-Young equation [65, 66].

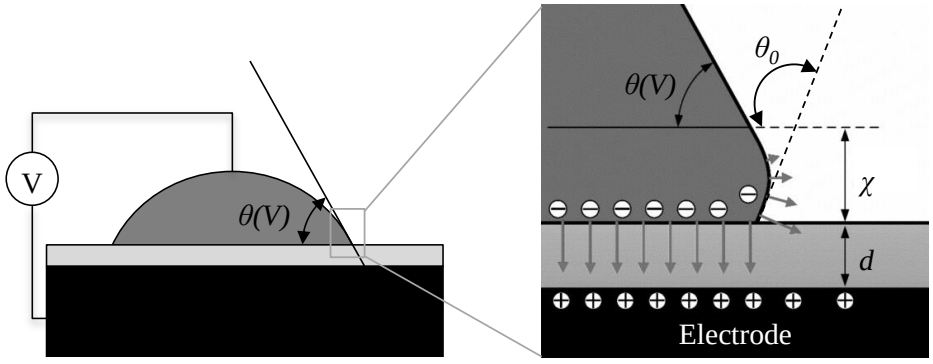

Figure 2.6. The static contact angle of an EWOD actuated droplet. θ_0 is Young contact angle. (Image courtesy of Prof. C.J. Kim [10].)

The density of the interfacial force is most strongly peaked at the liquid-gas interface within a distance of χ from the contact line (Figure 2.6) [10]. For most EWOD microsystems, χ is on the order of 1 μm and less than 1% of the gap height such that the actuation force is often treated as if it were acting exactly at the contact line [35, 67, 68]. In addition, equation (2-17) is only valid for static contact angles. Dynamic contact angles observed during EWOD actuated droplet motion are different from the static theory [69].

The Lippmann-Young equation can be derived using different approaches (thermodynamic, energy minimization, and electromechanical), which are detailed by Mügele et al. [70] and Berthier's book [12]. The thermodynamic and energy minimization approaches only address the static contact angle change, but do not cover the electric force aspects. The electromechanical approach, first by Jones et al. [34, 71], explicitly addresses EWOD actuation forces caused by the electric field. The electromechanical approach is based on either the capacitance model or the Maxwell stress tensor model. EWOD force calculations based on both models, both by Jones [33, 34], correctly predict the change in shape of the droplet. In both electromechanical models, contact angle is not needed or included in force calculations.

2.1.2.2 EWOD-Driven Droplet Actuation

2.1.2.2.1 Physical descriptions of droplet actuation

In the literature, there are three different physical descriptions of a droplet movement by EWOD actuation: (1) electrostatic forces, (2) surface tension forces, and (3) hydrostatic pressures.

- Electrostatic forces: This could be the most fundamental level among the three. The droplet is actuated by the electrostatic force induced by the EWOD effect. In the process, the contact angle is decreased. The net electrostatic force by the actuation voltage V is $F_e(V)$ [10, 33].

- Surface tension forces: With the decreased contact angle, the decreased slope of the liquid-fluid interface on the actuated side of the droplet pulls the droplet forward. The unbalanced liquid-fluid surface tension is $\gamma\cos\theta(V)$ [10, 12].
- Hydrostatic pressures: The reduced contact angle also changes the liquid-fluid curvature to reduce the Laplace pressure inside the droplet on the actuated side of the droplet. The liquid then flows toward the low-pressure region, so that the droplet is moved forward. The unbalanced hydrostatic pressure is $[P_r - P_a(V)]h$, where P_r is the pressure from the receding end, P_a the advancing ends, and h the gap height [10].
- All three expressions for the EWOD actuation force are interchangeable [10]

$$F_e(V) = \gamma\cos\theta(V) = [P_r - P_a(V)]h\,. \tag{2-18}$$

Depending on the purpose, one method could be more suitable than others. For example, the study of back and forth EWOD motion of droplets between the open and covered region uses the pressure interpretation because it needs to understand the flow distribution in the droplet [72, 73]. The hydrostatic pressure model has been discussed in section *2.1.1.4.2*. In the following subsections, the electrostatic model and the surface tension model are discussed.

2.1.2.2.2 Electrostatic model: EWOD circuit models

Electrical circuit models are simple but useful in predicting the behavior of EWOD microsystems. EWOD circuit models have become key tools in EWOD actuation force analyses through works by Jones [33, 34] and others [67, 74, 75, 76, 77]. In general, an EWOD device can be modeled as an electrical circuit, which has proper arrangements of equivalent resistors and capacitors. Figure 2.7 represents a simplified EWOD circuit model of a dielectric layer and a droplet in series between a top ground plate and the activated bottom electrode. Resistances of the dielectric layers and the filler medium are not included in the simplified circuit because they

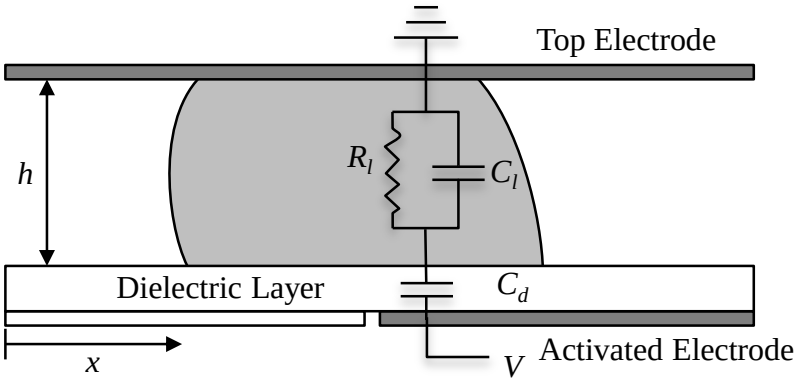

Figure 2.7. Side view of a DMFB configuration. A simplified electrical circuit model is overlaid on the bi-planar DMFB. The circuit parameters depend on the area, which is a function of *x*, of the droplet overlapping with the activated electrode.

are typically several orders of magnitude more than the droplet resistance. For a fixed applied voltage *V*, the droplet actuation energy is [10]

$$E = \int_0^V C_{EQ}(x) U dU = \frac{1}{2} C_{EQ}(x) V^2 , \tag{2-19}$$

where $C_{EQ}(x)$ is the equivalent capacitance, which is a function of the droplet moving distance *x*. The actuation force *F* of the droplet is

$$F = \frac{dE}{dx} = \frac{V^2}{2} \frac{dC_{EQ}(x)}{dx} . \tag{2-20}$$

Capacitance $C_{EQ}(x)$ is mainly determined by the droplet-electrode covered area and it is not sensitive to shapes of the droplet, fringing fields, and contact angle changes. Therefore, this electromechanical modeling (the capacitive lumped-element model) is robust, simple and versatile [33]. Another key benefit of this modeling approach is that it can be used to model the related frequency dependence by using a resistor-capacitor based circuit model [34].

2.1.2.2.3 Surface tension model: effective length of the contact line

An EWOD droplet has a triple-phase contact line, which describes the intersection of three interfaces involving the droplet, the ambient fluid, and the solid surface. When the droplet is

actuated, the unbalanced liquid-fluid surface tension on the triple-phase contact line can be defined as a line force density f_w [78],

$$f_w = \gamma_{LF} \cos\theta(V)\,, \tag{2-21}$$

where γ_{LF} is the liquid-filler-medium interfacial tension and $\theta(V)$ is the contact angle with applied voltage V. As shown in Figure 2.8(a), f_w is on the solid surface and is in the perpendicular direction of the triple-phase contact line. The total capillary force F_x acting on the droplet in the unit vector $\vec{\imath}$ direction is expressed as

$$F_x = \gamma_{LF} \cos\theta(V) \int_L dl\vec{n} \cdot \vec{\imath} = \gamma_{LF} \cos\theta(V) e\,, \tag{2-22}$$

where dl is a unit element of the triple-phase contact line, $\vec{n}$ the unit vector normal to the contact line, e the effective length of the contact line (Figure 2.8(a)). From equation (2-22), the total capillary force F_x is independent of the shape of the droplet, but defined only by the effective length of the triple-phase contact line. So, two droplets having different shapes but the same effective length would have the same capillary force on the droplets (Figure 2.8(b)) [12].

2.1.3 Critical Actuation Frequency of Electrowetting on Dielectric and Dielectrophoresis

The frequency of the actuation voltage has a crucial impact on the EWOD droplet actuation behavior. In an AC (f > 0 Hz) voltage situation, the droplet impedance and the dielectric layer

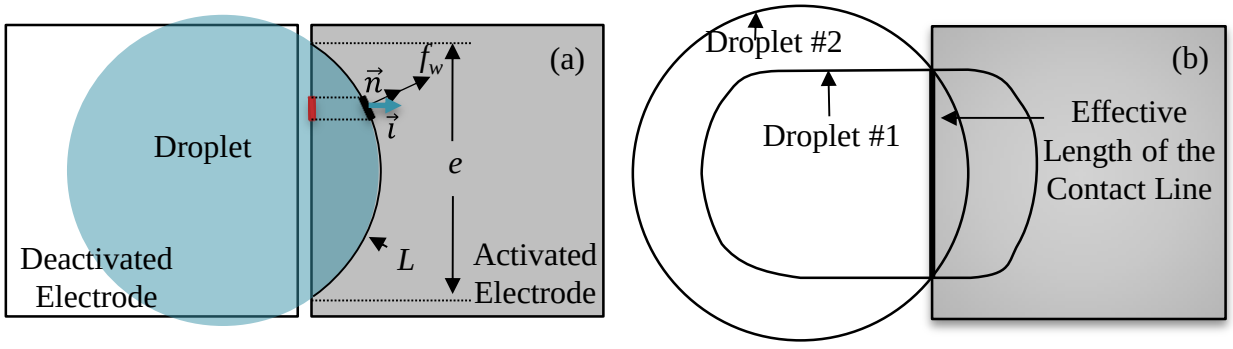

Figure 2.8. (a) The contact line and the capillary force acting on the droplet in the unit vector $\vec{\imath}$ direction. (b) Two different shapes of droplets have the same effective length and have the same capillary force on the droplets.

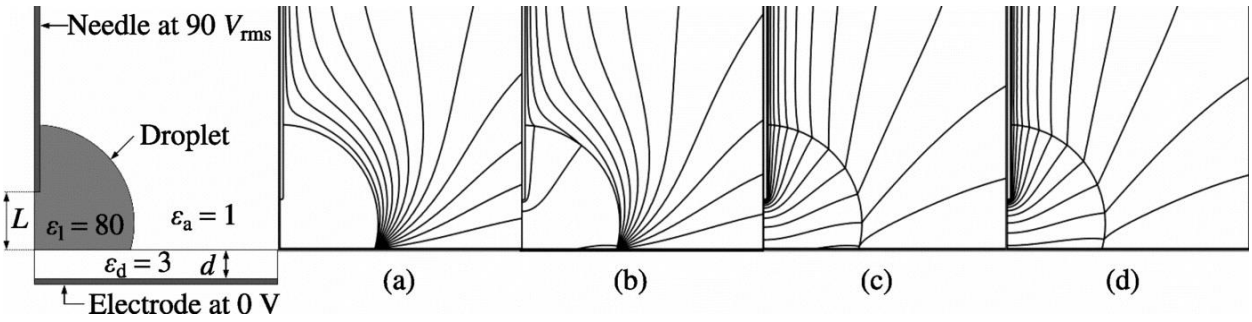

Figure 2.9. Potential redistributions vs. frequencies (contour interval = 10 V): (a) DC, (b) f = 10 kHz, (c) f = 100 kHz, (d) f = 1 MHz. (Reprinted with permission from [35]. Copyright 2009, AIP Publishing LLC.)

impedance are both frequency dependent, so that the electric field redistribution through the droplet can result in either an EWOD or DEP force. To distinguish between EWOD and DEP forces, a critical actuation frequency f_c can be used. When droplet actuations happen in low frequency regimes ($f << f_c$), the electric field is formed only in the dielectric layer such that only EWOD forces are induced. While operating in high frequency actuation regimes ($f >> f_c$), the electric field is redistributed through the droplet to form the DEP force [34, 77]. The frequency-dependent electric field redistribution under the EWOD actuation is illustrated clearly in Figure 2.9 by Lee et al. [35]. The critical frequency f_c is about 85 kHz. The simulations of electric field redistributions show that for DC or low frequency AC ($f < 10$ kHz) actuations, the electric field intensifies at the contact line. Increasing the actuation frequency causes more electric field redistributions within the droplet. At a high frequency ($f = 1$ MHz) the electric field at the contact line is mostly disappeared [35].

2.1.4 Working Range of Electrowetting on Dielectric

The dependence between the contact angle change and the actuation voltage (the Lippmann-Young equation) works well until a voltage threshold where contact angle decreasing stops. “Contact angle saturation” is used to describe this contact angle change limit. The static contact angle cannot be decreased to 0°, and the saturation usually takes place in the range of 30° - 60°

[12, 79]. Therefore, the maximum actuation voltage (V_{max}) for the EWOD actuation exists, and it is defined by the contact angle saturation voltage (V_{sat}), above which the droplet actuation force does not increase anymore; that is $V_{max} = V_{sat}$.

On the other hand, it is also observed that the actuation voltage needs to reach a certain actuation voltage threshold (V_{min}) to be able to move the droplet [80]. The minimum actuation voltage needed to move the droplet is determined by the resistance force on the contact line. This resistance is governed by the nature of the droplet, the solid surface, and the fluid medium, and it is usually quantified as contact angle hysteresis (α) [10, 12].

EWOD actuation is only effective between the two limits V_{min} and V_{max} [29, 43, 61]. Mechanisms of V_{min} and V_{max} limitations with respect to the contact angle saturation and hysteresis are not well understood [10, 12]. However, the estimates of V_{min} and V_{max} have been derived as [12]

$$V_{min} \approx 2\sqrt{\gamma_{LF}\alpha \sin\theta_0 / C} \quad \text{and} \tag{2-23}$$

$$V_{max} = \sqrt{2(\gamma_{SF} - \gamma_{LF}\cos\theta_0)/C}\,, \tag{2-24}$$

where C is the dielectric layer capacitance, γ_{LF} the liquid-filler-medium surface tension, γ_{SF} the solid-filler-medium interfacial tension, α the contact angle hysteresis, and θ_0 the Young contact angle. To minimize the actuation voltage required to move droplets, it would need a large capacitance and Young contact angle θ_0 ($\text{small}\sin\theta_0$), a small surface tension γ_{LF} and hysteresis α. Although a small V_{min} is typically desirable in EWOD actuation, an acceptable V_{min} actually prevents unwanted movement of droplets and stabilizes the system [10]. Similarly, the value of V_{max} depends on the capacitance, C, the interfacial tensions, γ_{SF} and γ_{LF}, and the Young contact angle, θ_0. It is important to get a balance between the optimization of V_{min} and V_{max} because some adjustments might work against each other.

2.2 Digital Microfluidic Biochip Microsystems

2.2.1 Architecture of Digital Microfluidic Biochips

There are fundamental functional blocks needed for a DMFB. These functional blocks are a method of introducing reagents and samples (I/O ports), a way to prepare samples for tests (sample preparation), methods for microfluidic operations (droplet manipulations), and a way to detect micro-analytical work (detections). Each of the functional blocks is discussed in the following subsections, beginning with I/O ports.

2.2.1.1 I/O ports

The input/output ports are the interface between the external world and the DMFB. Potentially, there are four types of input/output ports as shown in Figure 2.10: the Sample Input port, the Droplet I/O port, the Detection I/O port, and the System Control I/O port. The Sample Input port is problematic to implement due to the huge discrepancy between sizes of real world samples (microliters) and DMFB droplets (nanoliters). Loading samples and reagents onto the biochip typically involves a special interface between the outside world and the DMFB. Reagent cartridges can be connected to the DMFB by using Droplet I/O ports. Wastes can be stored in waste reservoirs or can be flushed out through the Droplet I/O port.

The integration of detection into microfluidic biochips, especially for those technologies that scale better upon miniaturization such as electrochemical detection, is a clear goal for the development of biochips. However, some mature and stable detection technologies like optical detection and magnetic nanoparticle detection, which cannot be easily integrated into the chip, will still be used with DMFBs. One useful approach is a modular system design in which the detector is decoupled from the microfluidics, and detection is performed through the Detection I/O port. The Detection I/O port can also serve the purpose of optical droplet location sensing for monitoring the rapidly moving droplets on the biochip.

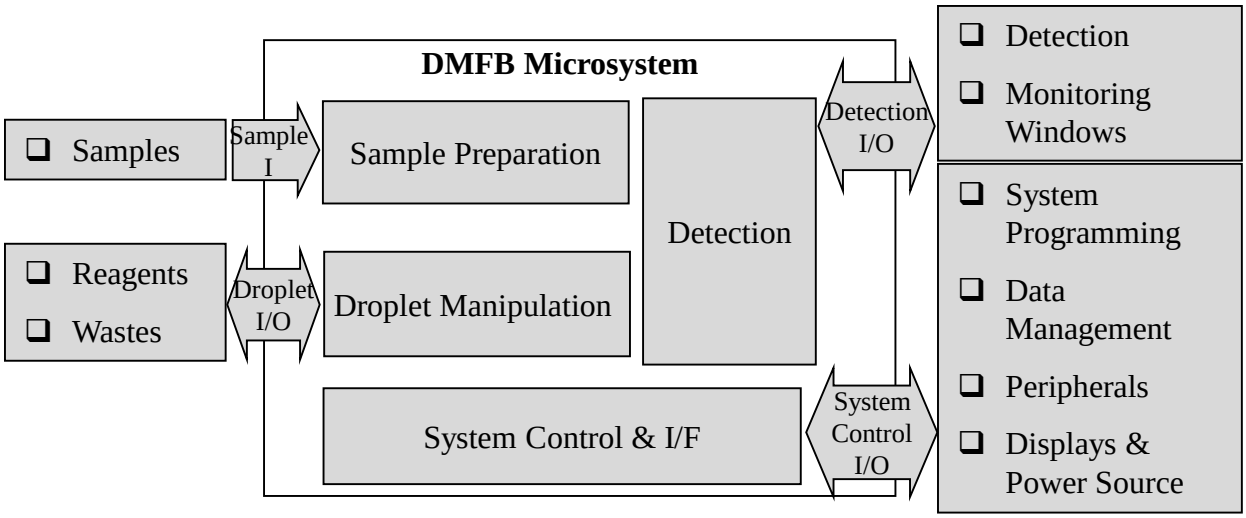

Figure 2.10. Block diagram of a DMFB microsystem.

The System Control I/O port will be needed for programming the chip, displaying the test results, calibration, data management, and many other system tasks. If necessary, a printer, USB memory storage, and a wired/wireless network can be connected to the DMFB through the System Control I/O port. The DMFB microsystem also connects to AC/DC power sources through the System Control I/O port.

2.2.1.2 Sample Preparation

Sample preparation refers to the techniques in which a sample is prepared to make it suitable for its analysis. Typically, sample preparation is performed to increase the test responsiveness of analytes or to reduce the effect from interfering substances. For DMFBs, on-chip sample preparation is very challenging because of the miniaturization of the system. Sample preparation for DMFBs may involve particle separation, purification, dissolution, dilution, concentration, labeling, and filtering. Sample pre-concentration becomes essential in DMFB assays where the molecules to be detected become very small in number due to the small-volume sample in the droplet. Sample dilution can be used to increase the measurement linear range and to lessen the

influence from interfering substances. One example of particle separation is separating blood cells from whole blood to obtain serum or plasma. A wide range of particle separation techniques for microfluidic systems have been demonstrated, including EWOD [81], DEP [82], capillary electrophoresis (CE) [83], and magnetic forces [84]. These particle separation techniques might cause particle damage because they typically require external force fields and possible bead attachments before separation. Therefore, size-based separation techniques, which are based exclusively on the particle size and fluidic flow such as pinched flow fractionation (PFF) [85] and deterministic lateral displacement [86], have been proposed as alternatives for sample preparation. In addition, continuous particle separation can be performed by these size-based separation techniques to allow large scale sample processing.

2.2.1.3 Droplet Manipulation

One clear advantage of the DMFB platform over full-custom and bottom-up solutions is that all DMFB microfluidic operations can be performed by a set of basic microfluidic unit operations [11]. Fundamental microfluidic operations of DMFBs, such as droplet creating, transport, cutting, merging, and mixing, are discussed as follows.

2.2.1.3.1 Liquid storage and droplet creating

Liquids loaded from the Sample Input ports are stored in reservoirs. Reservoirs are typically large special-shaped electrodes that have enough liquid storage areas and structures for droplet creating. A basic DMFB might have only three reservoirs: the sample reservoir, the reagent reservoir, and the waste reservoir. Depending on the application, more or other reservoirs might be needed.

Droplet creating is the process of creating droplets from reservoirs. Droplet creating is the most critical operation of a DMFB because it decides the system basic unit—the droplet. EWOD droplet creating occurs by activating droplet creating electrodes, which typically are adjacent

serial electrodes, and the pull-back electrode. These activated electrodes extrude and pull a droplet out from the reservoir [87]. A reliable and repeatable droplet creating process depends heavily on detail physical designs of the reservoir, the pull-back electrode, the creating electrodes, and the gap height.

2.2.1.3.2 Transport of fluids

Droplet transport is the most common microfluidic operation in DMFBs. EWOD droplets, from 1 to 1,000 nL volume, have been actuated to a speed at around 10 cm/s by 60-V actuation voltages [87]. Droplet pathways consist of an array of electrodes that connect different areas of the DMFB. As the number of electrodes increases, the complexity of the control circuit is also increased dramatically. A scalable electrode-control mechanism with a small number of control pads would be crucial for large-scale DMFBs, which might have over a thousand electrodes.

Droplet routing is used to move multiple droplets simultaneously from multiple beginning locations to the designated destinations without fixed pathways. DMFB routing is very different from very-large-scale integration (VLSI) routing because droplet properties are fundamentally different from electron properties. The DMFB routing path selection needs to schedule droplet actuations under physical constraints such as contaminations, unreliable actuations, and timing restrictions.

2.2.1.3.3 Droplet cutting and merging

Normally, three electrodes are used to perform droplet cutting. During droplet cutting, the middle electrode is deactivated and the outer two electrodes are activated. Consequently, the droplet is stretched by EWOD actuation forces of the two activated electrodes, and it is pinched off into two daughter droplets by hydrophobic forces from the middle electrode. For merging two droplets into one, the outer two electrodes with droplets are deactivated and the middle

electrode is activated. However, EWOD cutting by three electrodes can only be performed under a bi-planar structure with appropriate gap heights and electrode sizes [61]. For a coplanar EWOD structure, the lack of the cover plate makes cutting impossible [88]. Moreover, EWOD cutting is not very uniform cutting and its volume variation is around 7% [87].

2.2.1.3.4 Mixing, incubation and reaction

In DMFBs, droplets are also used as virtual chambers for mixing, incubation and reaction. Mixing occurs by transporting and merging two droplets together. Effective droplet mixing is difficult to achieve in DMFBs due to small Reynolds numbers of droplets. The ability to mix droplets quickly while only utilizing a small area can significantly improve the performance of the microsystem. There are two fundamental principles to improve mixing. The first one is to create a turbulent flow inside the micro-scale droplet. Mixing two droplets together at high motion speeds to create internal turbulent flows is at least 10 times faster than passive diffusional mixing. Fowler et al. demonstrated a square movement pattern for fast droplet mixing [89]. Alternatively, multilaminates can be created to achieve fast mixing via multilaminated diffusion. Wang et al. proposed a very efficient split-and-recombine lamination mixer based on the microelectrode dot array (MEDA) architecture [90]. In incubation steps, if elevated temperatures are required, such as PCR amplification, a micro-heating element should be prepared on the substrate surface for the purpose [15, 45].

2.2.1.4 Detection

The success of DMFB microsystems depends heavily on suitable detection technologies that are capable of reliable and repeatable measurements. There are two main approaches of performing detection for DMFBs: (1) coupling existing detection technologies to DMFBs, and (2) on-chip detection. Detection technologies that can be applied to DMFB devices are categorized into three main principles: optical, mass spectrometry, and electrochemical [56].

Optical detection has been commonly incorporated in DMFBs because to date most DMFBs are fabricated by transparent materials and can be readily used for optical detection. There are several advantages to use optical detection in DMFBs: no interconnection, nondestructive detection mode, multiple detection capability, and rapid signal generation/reading. However, the small amount of sample in the DMFB could have relatively poor detection limits with optical detection [91]. From the technology point of view, there are four categories of optical detection for DMFBs: absorbance detection, fluorescence detection, chemiluminescence detection, and surface plasmon resonance (SPR) detection. Absorbance detection is a well-established detection technique in analytical chemistry and laboratory diagnostics and absorption spectroscopy is commonly used in DMFBs [92]. Fluorescence detection is the dominant optical method used in DMFBs, due to superior signal-to-noise ratio, selectivity, sensitivity, and easy incorporation [93]. With high sensitivity and selectivity, chemiluminescence detection is also an attractive alternative for DMFBs [92, 93]. SPR is a powerful tool for the real-time label-free measurement of bio-molecular interactions [94, 95].

Mass spectrometry (MS) is always a strong alternative to optical detection methods. Recent interest in molecular biology has led to the development of miniaturized and enhanced analysis that interface microfluidics with MS. Coupling DMFB devices to MS techniques can yield improved sample preparation (by microfluidics) and enhanced analysis (by MS) [96]. However, the integration of MS on the chip will not happen in the foreseeable future, and therefore efforts will remain on the interfacing of the DMFB to MS for off-line analysis. An open DMFB system without the cover plate can accommodate MS from above and thus allows increased flexibility for on-line monitoring [56, 88].

Electrochemical detection is based on the oxidation (chemical reaction) or antibody-antigen

reaction that can be detected electrically as changes of potential, current, conductance or capacitance. Electrochemical detection is the technology most amenable to the miniaturized DMFB, especially through CMOS fabrication technologies. It also has very low instrumentation costs. This detection technology represents the true possibility to perform completely integrated biochemical assays on a DMFB. CMOS-based capacitive sensing technologies have recently created substantial interest for a wide variety of biochemical detection applications [97]: DNA detection [98, 99], antibody-antigen recognition [46, 100, 101], and cell monitoring [102, 103].

2.2.1.5 System Control

The system control block integrates and manages other on-chip function blocks. It can be a simple interface circuitry to a PC or other controllers, or it can be a fully integrated control system. Also, the complexity of a DMFB could vary considerably and it drives the requirements of the system control performance. A manual control through on/off switches of a mechanical relay box could be enough for a single and simple microfluidic basic operation. However, a DMFB system performing concurrent biomedical assays would require a much more complex control system which might obtain significant central processing unit (CPU) power and software programmability.

2.2.2 Open and Covered Digital Microfluidic Biochips

From the mechanical structure point of view, there are two different types of DMFB microsystems: open DMFBs and covered DMFBs. For covered DMFBs, the droplet is confined between two plates. For open DMFBs, the cover plate is removed and the sessile droplet is sitting freely on the bottom plate as shown in Figure 2.11(c). Often, an open DMFB is also referred as a coplanar DMFB and a covered DMFB is also called a bi-planar DMFB. Both terminologies are used in this research. Each of these microsystems has its own advantages. Droplet creating, transport, and cutting are preferably performed in covered DMFBs, but droplet

mixing and evaporation are rather performed in open DMFBs [12].

Initially, open DMFBs were built with catenae, which were used as the reference electrodes. The EWOD actuation voltage is established between the activated electrode on the bottom plate and the catena. Physically, it is very difficult to mount and align catenae in micro-scale systems [12]. There are two new developments for the coplanar EWOD actuation: buried catena, or no catena. In the no-catena coplanar EWOD actuation, the next electrode is used as the reference electrode. The electric field is established in which the activated electrode is at the potential V+, and the next electrode is at reference potential (V = 0). Jones has shown the capacitance and voltage model of the EWOD force acting on a coplanar droplet [33, 79]. No-catena coplanar EWOD actuations, as indicated in Figure 2.11(c) and (d), have been successfully demonstrated [88]. The results validate the possibility that open DMFBs can be made with just electrodes on the bottom plate without the cover plate or catenae. Another coplanar EWOD actuation technique is to bury catena (the ground electrode) in the substrate. This coplanar EWOD

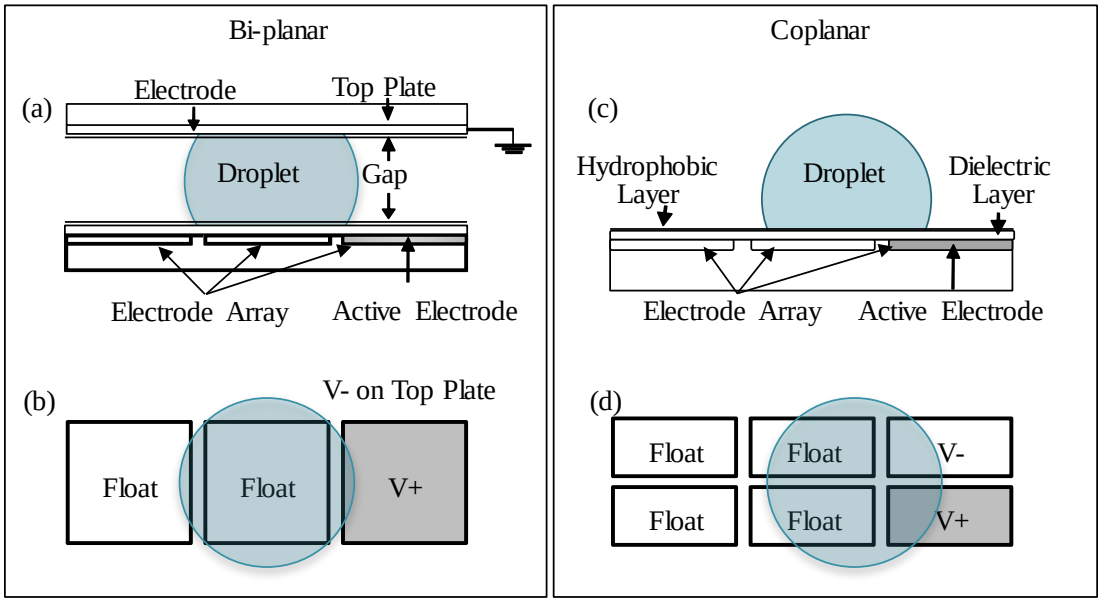

Figure 2.11. Two different types of EWOD-based microsystems: (a) side view of a covered system where the droplet is confined between two plates; (b) top view of the covered system; (c) side view of an open system where the sessile droplet is sitting freely on a horizontal solid substrate; (d) top view of the open systems.

actuation technique has also been demonstrated, where the ground electrodes are routed in gaps between the electrodes [104].

In a covered DMFB, the droplet and the filler medium are sandwiched between the top plate and the bottom plate (Figure 2.11(a)). Individually controllable electrodes are patterned on the bottom plate, and a continuous ground electrode is coated on the top plate. Glass substrates and transparent electrodes, which are formed by a material like indium tin oxide (ITO), are used to make the microsystem compatible with observation from a microscope. A dielectric layer is added on the bottom plate to separate the droplet and the electrode array. A thin hydrophobic layer (e.g. Teflon AF1600) is coated on both plates to decrease the wettability of plate surfaces. In addition, a covered DMFB could be implemented with a passive cover and the coplanar EWOD actuation. Basic EWOD microfluidic operations (e.g. moving, cutting and merging) have been demonstrated in a covered EWOD configuration where the top plate has no electrodes [104].

2.3 Applications of Digital Microfluidic Biochips

Because of their versatility, DMFBs have been applied to a wide range of diverse applications [56, 105] such as particle manipulation [81], electronic cooling [106], optical display and lens systems [107], micro viscometer [108], microconveyor systems [109], and micro-air bubble manipulation [110]. However, the most popular DMFB applications reside within biomedical applications that require small amounts of sample, high flexibility, and high reconfigurability [55, 56]. In the following subsections, these biomedical applications are reviewed and the areas where on-chip CMOS sensors can contribute are specifically mentioned.

- Chemical and Enzymatic Assays

DMFBs have been used for chemical and enzymatic reactions due to their ability to independently control multiple droplets, which are used as reaction chambers. This DMFB

application typically involves droplet creating and mixing to form reaction chambers for precise measuring of reactants. Chemical and enzymatic reactions have been performed in DMFBs for applications including clinical diagnostics, chemical assays for environmental detection, studying reaction kinetics, and the synthesis of new compounds. One example of the diagnostic applications was the DMFB glucose assay on human biofluids with an integrated absorbance detector [21, 111]. As a chemical assay for environmental detection, the detection of 2,4,6-trinitrotoluene (TNT) was reported [112]. Also, DMFBs are used for analyzing enzyme kinetics and activity [113, 114]. The enzymatic and chemical synthesis of new compounds is an emerging application of DMFBs [115, 116]. An integrated CMOS-based capacitive sensor was demonstrated using standard chemical solutions [117]. This demonstration reveals the viability of a fully integrated DMFB for chemical and enzymatic assay applications.

- Immunoassays

An immunoassay is a biochemical test that detects relevant analytes through the use of specific antibody-antigen interactions. Antibodies are primarily used in immunoassays to bind to the targeted analyte with high selectivity. Immunoassays are very popular in clinical tests and it has recently been the subject of interest for DMFB applications [44]. Electrochemical immunoassays, which combine antigen-antibody reactions with electrochemical detection [118], are of particular interest to this research because potentially they can be fully integrated into CMOS-based DMFBs. Biosensors based on amperometric, potentiometric, impedimetric, and capacitive approaches can be easily found [119, 120, 121], among which CMOS-based capacitive sensors have lately generated enormous interest for antibody-antigen recognition [46, 100, 101, 122].

- DNA-Based Applications

Manipulating and characterizing samples of DNA have become critical steps in a wide range of fields, for instance, medical diagnostics, pharmaceutical research, and forensics. DNA-based applications are typically handling small samples and require greatly multiplexed operations. Thus, it is not surprising that DMFBs are attractive to develop microfluidic operations and micro-scale reaction chambers (droplets) for DNA-based applications [105]. To date, DMFBs have been used for purifying and extracting DNA samples [15, 123], generating recombinant DNA [124, 125], DNA hybridization assays [126, 127], pyrosequencing (DNA sequencing) [128], and polymerase chain reaction [129, 130, 131].

- Proteomics

Proteomics has been a growing field of interest for applications such as vaccine and drug discovery [132]. The sample preparations for proteomic experiments typically are very tedious, lengthy and inefficient due to multi-step sample processing. Assay automation and the ability to individually address multiple reagents make DMFBs a good fit for proteomic experiments [48, 133, 134, 135, 136].

- Cell-Based Applications

DMFBs are advantageous for cell-based applications because of assay automation, multiple reagents, reduced reagent use, and fast analysis time. DMFB approaches for cell sorting, cell monitoring and cell assays have recently gained a lot of interest [105]. Many different cell assay DMFB systems have been demonstrated [105]. Also, DMFB systems have been used to manipulate and sort cells by use of electrical [82], magnetic forces [137], and optical [138]. The emerging CMOS-based capacitive sensing technology for cell monitoring [102, 103] is of specific interest to this research.

CHAPTER 3. MICROELECTRODE DOT ARRAY ARCHITECTURE

To achieve the research objectives, a novel EWOD based MEDA architecture was proposed [90, 139]. This chapter covers the MEDA architecture. The first section gives an introduction to the MEDA architecture. The block diagram of the architecture is discussed in Section 3.2. The MEDA architecture has a hierarchical structure which is discussed in Section 3.3. An important issue for the MEDA architecture is the control of individual microelectrodes, and the proposed daisy-chained control structure is illustrated in Section 3.4. Designing microelectrodes by the self-contained structure is an important step of implementing the MEDA architecture. This self-contained structure is reviewed in Section 3.5. Other aspects of the MEDA architecture are taken into account in Section 3.6, including scalability considerations, cover structures and others. A summary of design guidelines is listed in Section 3.7. The last section presents modeling and simulations of EWOD actuation forces and motion performances of the MEDA architecture.

3.1 Introduction

Traditionally, developments of DMFBs have been taking a bottom-up approach that discrete microfluidic components are designed and integrated together to perform a particular microfluidic application. Therefore, current DMFBs are typically developed by custom approaches instead of standard fabrication components and processes. The design complexity of future DMFBs will increase dramatically due to more concurrent bioassays, higher system integration, and more sophisticated system control. In addition, time-to-market and mass production are also important design considerations for DMFBs. Current approaches in designing and fabricating DMFBs cannot scale well for these challenges. It is highly desirable to have a top-down design methodology, which has the same level of CAD support as the ASIC design, for DMFB developments. One viable solution will be a validated DMFB enabling technology that offers standard DMFB building elements to enable the top-down design

automation for DMFB developments, similar to the gate array and the standard cell to the development of ASICs. In addition, it is also important that these validated DMFB building elements are amenable to well-established and commonly available fabrication technologies. The lack of standard DMFB components makes the implementation of the hierarchical top-down design approach for DMFBs difficult.

Configurability, scalability, and portability of standard DMFB building elements are critical aspects for the success of the hierarchical design approach of DMFBs. Unlike other DMFBs, which use fix-patterned and fix-sized electrodes to perform predefined bioassays, the proposed MEDA architecture is based on the concept that bioassay functions can be implemented by dynamic configurations of a sea-of-microelectrode array. In this configuration, an array of identical DMFB building elements called "microelectrode cells" are dynamically configured and activated to define microfluidic components, operations and applications of the biochip. The electrode configured from microelectrodes is called "configured microelectrode array", or CMA, to distinguish it from a conventional (solid) electrode.

Figure 3.1(a) shows the basic concept of the MEDA architecture that a DMFB could be built through the configuration of microelectrodes. Figure 3.1(b) illustrates an example of a reservoir CMA and associated square CMAs. Similar to the development of the ASIC that all logic gates and digital circuits are made of CMOS field-effect transistors, microfluidic components and microfluidic operations are configured from microelectrode cells in the development of the MEDA-architecture DMFB. The architecture is designed in a way that it opens the possibility of utilizing commonly available fabrication technologies, specifically the CMOS technology, to fabricate DMFBs. Among all droplet actuation methods, the focus is on EWOD microfluidics.

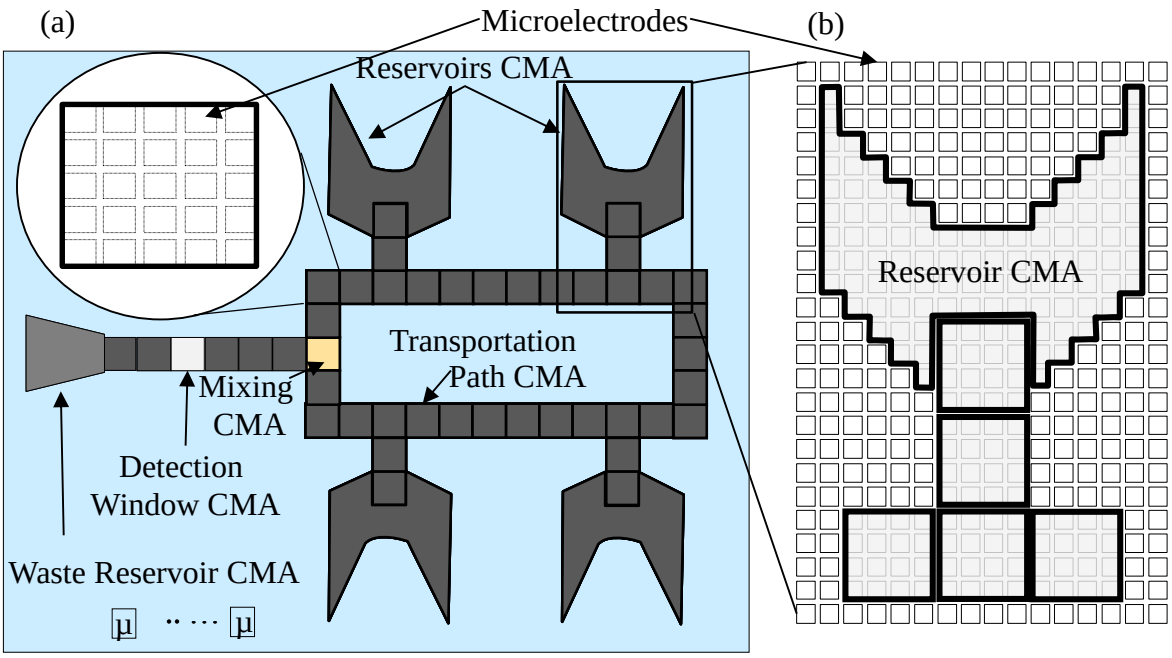

Figure 3.1. The MEDA architecture: (a) microelectrodes are configured into various shapes and sizes of CMAs to build a LOC device; (b) the illustration of an enlarged reservoir CMA.

Not only is it one of the most common electrical droplet actuation methods, but it is also the one most compatible to standard CMOS technologies.

The MEDA architecture can be implemented by using the typical DMFB system structure with scaled-down EWOD electrodes. Although coplanar, bi-planar or hybrid (a combination of coplanar and bi-planar) system structures are possible for the MEDA architecture, the typical configuration uses two parallel plates (i.e. bi-planar structure) [29, 43]. A simplified MEDA-architecture biochip with a bi-planar structure is shown in Figure 3.2. It is very similar to the typical EWOD bi-planar structure, but there are two major differences: (a) in the MEDA architecture, the droplet is actuated by a CMA, which is composed of a group of microelectrodes, instead of just one electrode in the conventional way; (b) the reference potential applied to the top reference plate is not necessary to be 0 V but could be the high actuation voltage V. No polarity indicators on the voltage source V in Figure 3.2 reflects the possibility that the EWOD

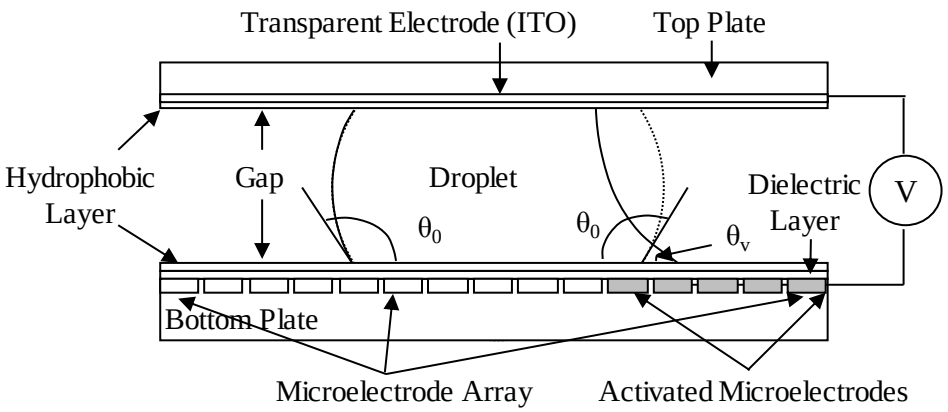

Figure 3.2. The illustration of the MEDA architecture by using scaled-down electrodes as microelectrodes based on EWOD bi-planar structure (not to scale)

actuation could be done by applying the high voltage to the top plate and grounding (0 V) the activated microelectrodes. Regardless of the polarity, once an actuation voltage is applied between the top electrode and the bottom actuation microelectrodes, the EWOD effect causes the movement of the droplet [40, 61, 140].

3.2 Architecture Block Diagram

The block diagram of a DMFB based on the MEDA architecture and CMOS fabrication technologies is illustrated in Figure 3.3. The two main blocks are the system control block and the microelectrode cell. Normally, a DMFB has only one system control block, but a plurality of microelectrode cells. The number of microelectrode cells depends on application needs and the limitation of fabrication technologies. Microelectrode cells are daisy-chained together to simplify internal wiring and to maximize the scalability. One microelectrode cell is composed of a droplet actuation microelectrode, 1-bit cell data, 1-bit map data and the control circuit. The droplet actuation microelectrode is the physical microelectrode which can be activated to cause the EWOD effect to move the droplet. The 1-bit cell data holds the logic value of the activation of the microelectrode where typically a “one” means activation and a “zero” means deactivation of

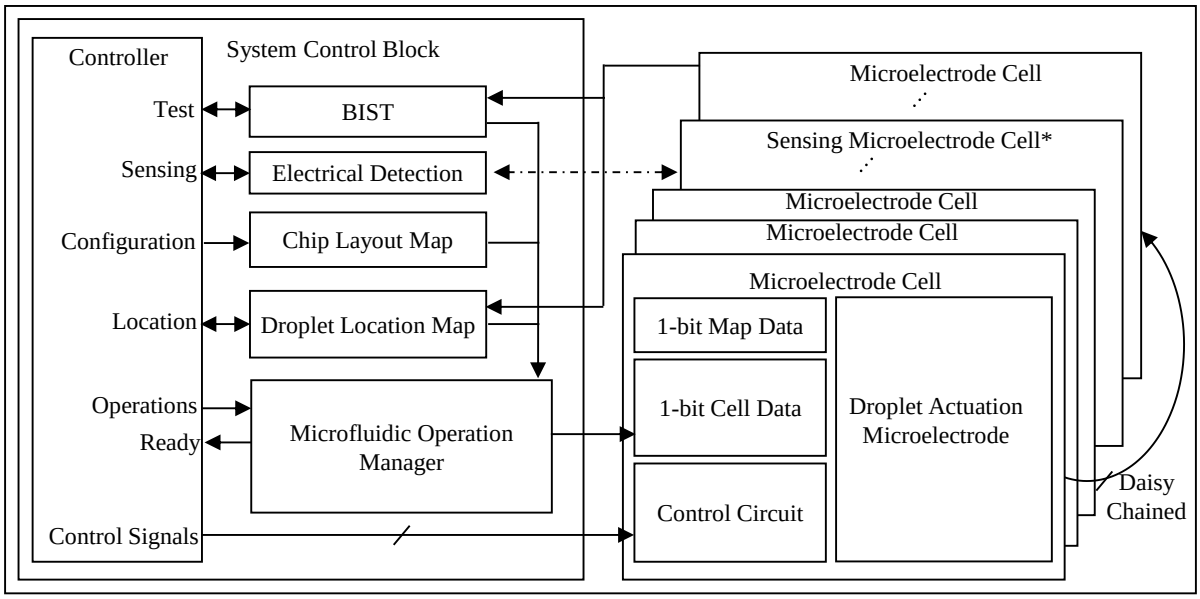

Figure 3.3. Block diagram of a DMFB based on the MEDA architecture and CMOS fabrication technologies.

the microelectrode. Before applying the actuation voltage, 1-bit cell control data are shift-loaded into all microelectrode cells. The control circuit manages control logics, droplet detection, microelectrode activation and the daisy-chained structure of the microelectrode cells. The 1-bit map data collects the logic value of the droplet detection result. Typically, a "one" means droplet detected and a "zero" means no droplet detected. The physical representation (the layout view) of the microelectrode cell is usually designed first. Then the microelectrode cell is duplicated to form a microelectrode array with a daisy-chained connection.

In the system control block, the controller can be implemented in many different ways. A PC with an appropriate hardware interface card, a micro-controller or other control platforms can do the job as long as it has a CPU, programmable input/output peripherals, enough memory, and software programmability. The chip layout map manages configuration data, the layout of the chip and design details of microfluidic components. The droplet location map reflects the real-time locations of droplets on the DMFB. The microfluidic operation manager translates the

layout map, the droplet location map and the DMFB applications from the controller into a map of 1-bit cell data. For example, if not all droplets are in the desired locations after the actuation, the last actuation cycle might be executed again or different routes would be decided for the next actuation cycle. Therefore, the first thing for each actuation cycle is performing the droplet detection. Then, the next actuation data are decided accordingly. Physical actuations are performed by shift-loading the 1-bit cell data into microelectrode cells followed by activating the actuation driver. The built-in self-test (BIST) block is used to verify the internal electrical functionality of the DMFB. The electrical detection block represents a fully integrated electrical detection circuitry for measuring the test results. Special arrangements would be required to tie the electrical detection function to one or multiple special microelectrode cells. Depending on fabrication technologies and application needs, the system controller can be entirely or partially integrated into the DMFB.

3.3 Hierarchical Structure

To improve the design efficiency of traditional bottom-up design methods, DMFB top-down design methods have been proposed [18, 87, 141]. It is an anticipated goal to leverage DMFB architectural designs to cover as many applications as possible. The concept is that the wide varieties of biomedical applications need to be mapped into a set of microfluidic operations to manage the design complexity. Consequently, this set of microfluidic operations are then performed by dedicated microfluidic components [87]. To accomplish this DMFB architectural design goal, the architecture has to be hierarchical. At the first level, descriptions of biomedical applications are translated into a set of microfluidic operations. The second level manages the microfluidic operations, including routing algorithms, types of microfluidic operations and timing sequences. The third level configures and manages microfluidic components to implement the microfluidic operations. At the bottom level, these microfluidic components are

mapped into different groups of identical microelectrodes. This hierarchical design approach is shown in Figure 3.4. The MEDA hierarchical architecture has advantages in implementing the top-down system-level design methodology because the identical microelectrode cells work as the foundation of building the entire DMFB hierarchically.

3.3.1 Biomedical Microfluidic Function Layer

A top-down design methodology of the MEDA architecture starts from the biomedical microfluidic function layer. At this layer, application-level functions and bioassays are described and specified using a DMFB protocol. For example, one DMFB could perform multiple immunoassays such as a 12-in-1 drug-of-abuse check or cell monitoring. It is anticipated that progresses in DMFB developments will yield well-defined DMFB design protocols. High-level description languages, such as hardware description language (HDL) or SystemC, can also be used to model the high-level design. This application-level design is then used to perform

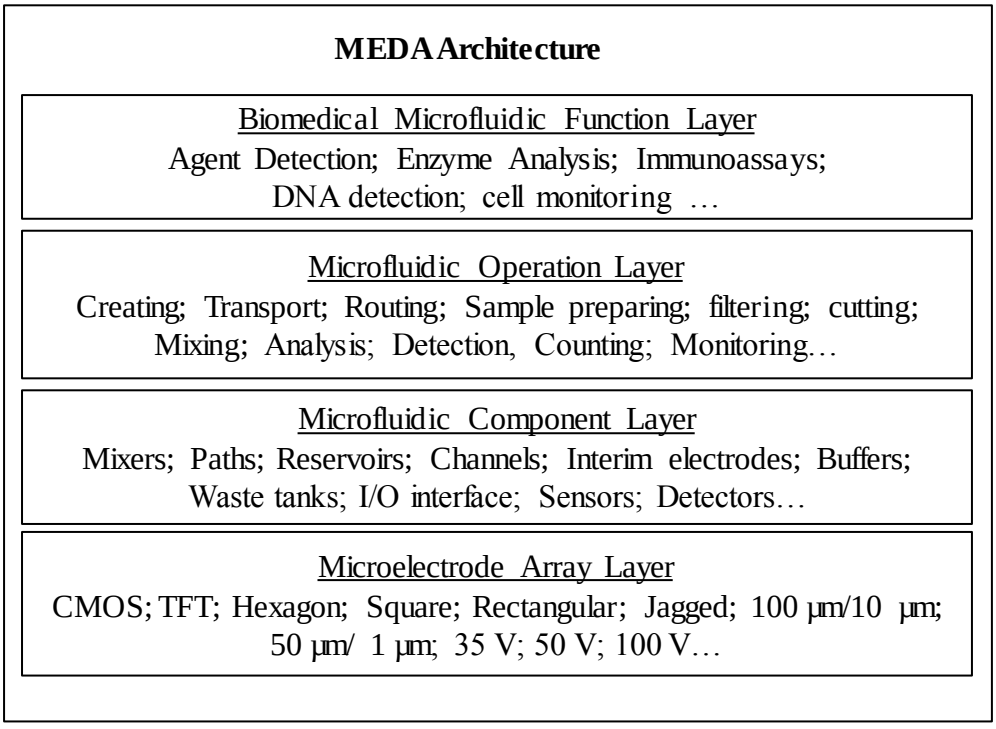

Figure 3.4. The hierarchical structure of the MEDA architecture.

behavioral-level simulations and verifications for assay functions. Next, these assay functions are converted into detailed implementations of a sequence of microfluidic operations of the DMFB by a synthesis tool. As high design complexity and large-scale system integration of DMFBs are anticipated to happen, synthesis tools are desperately required to cope with design challenges. Synthesis tools for DMFBs can be developed by leveraging classical ASIC CAD synthesis techniques, which are well-established today [18].

3.3.2 Microfluidic Operation Layer

The microfluidic operation layer controls and manages sequences of microfluidic operations such as creating, transport, mixing, and detection. After biomedical microfluidic functions being translated into specific sequences of microfluidic operations, the microfluidic operation layer optimizes sequences of microfluidics operations based on biochip resource constraints and adds actuation timing aspects to these microfluidic operations. It then converts these microfluidic operations into corresponding microfluidic components and actuation timing sequences of these microfluidic components. Practically, both the biomedical microfluidic function layer and the microfluidic operation layer are methodologies of design abstraction, whereby low-level microfluidic component configurations and layouts are encapsulated into abstract microfluidic representations (such as “Cutting” or “Diagonal Transport”). Along with microfluidics advances, this top-down design methodology will help designers to scale DMFBs from comparatively simple single-function DMFBs to complex multi-function DMFBs.

3.3.3 Microfluidic Component Layer

At the microfluidic component layer, physical representations of microfluidic components required for microfluidic operations and the final layout of the biochip are generated at the geometrical level. The final layout includes physical shapes, sizes and locations of all microfluidic components. One of the key tasks for this architectural layer is to map microfluidic

components into groups of microelectrodes and other physical design details such as the dimensions of the top cover and the height of the gap. Actuation timing sequences of microfluidic components are further converted into activating/deactivating timing sequences of each individual microelectrode.

3.3.4 Microelectrode Array Layer

The microelectrode array layer is the foundation of the hierarchical structure. Microelectrode arrays can be physically implemented in many different ways. The shapes of microelectrodes can be hexagonal, square, or jagged [29]. Other dimensional details are also important for the microelectrode array layer such as fabrication technologies, sizes of microelectrodes, and the spacing between microelectrodes. As indicated in Figure 3.4, for example, 100 μm/10 μm means the microelectrode has a 100 μm length and 10 μm spacing; CMOS means the fabrication technology is CMOS; and 35 V indicates the maximum actuation voltage.

3.4 Daisy-Chained Control Structure

In addition to physical microelectrodes, several other aspects of the system architecture must be taken into consideration. An important issue for the microelectrode array design is the independent control of individual microelectrodes. An m × n array generally requires m + n pads in order to control individual electrodes simultaneously, where m and n are numbers of rows and columns, respectively. Traditional DMFB control circuits are similar to semiconductor memory designs where a column decoder and row decoder are used to control the electrodes. One electrode in the array can be addressed at a time by a corresponding row pad and a corresponding column pad. The number of required pads is $\log_2 m + \log_2 n$. Besides the big number of control pads, the complexity of signal routing among electrodes will also increase significantly with the increasing number of electrodes. Fundamentally, this traditional control design will not work well with the MEDA architecture, which commonly has a big number of microelectrodes.

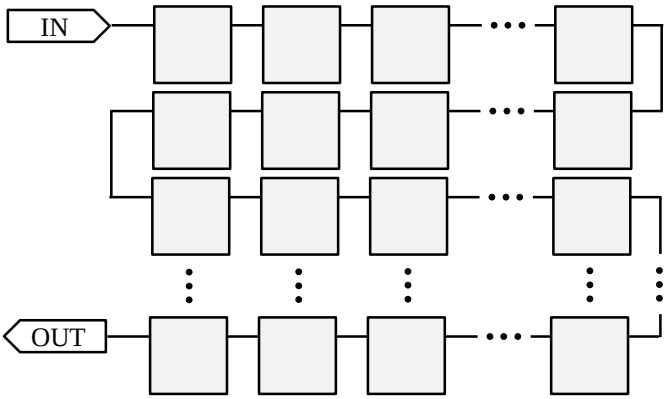

Figure 3.5. The daisy-chained control structure of the MEDA architecture.

A viable solution is to connect microelectrodes in a daisy-chained configuration as shown in Figure 3.5. Each small block in the figure represents a microelectrode cell. These microelectrode cells are daisy-chained in a similar way to a scan-chain. The activation of individual microelectrodes is controlled by serially shifting control data into the one-bit control register of each microelectrode cell. Using this highly scalable daisy-chained control structure, the MEDA architecture can achieve 100% individual-controllability of each microelectrode with a minimum number of control pads. The minimum number of control pads could be only three for the daisy-chained control structure, i.e. IN, CLK and OUT. Also, this daisy-chained control structure dramatically simplifies the BIST design because the scan-chain provides an easy way to set and verify every register in the DMFB. In addition, the same scan-chain is used to read out the one-bit droplet detection result of each microelectrode. All logic values of droplet detection are first clocked into the daisy-chained registers and then serially shifted out. Because the daisy-chained registers are used to control the actuation data as well as the readout of the droplet detection data, the sequence and timing of each control step is critical and will be explained in details in the "Timing of control signals" section.

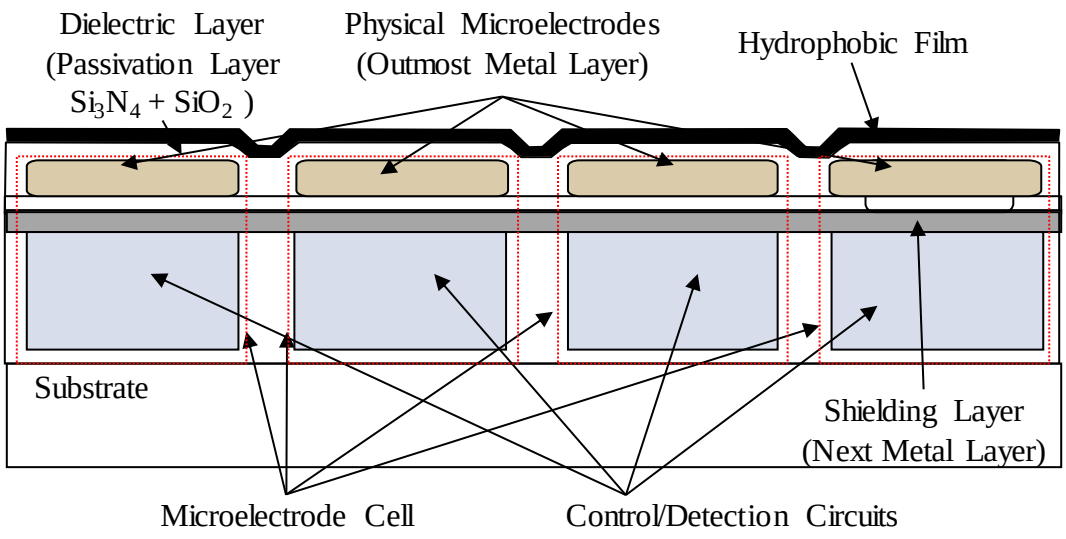

Figure 3.6. Side view of self-contained microelectrode cells.

3.5 Self-Contained Structure

Another important design of the MEDA architecture is the self-contained structure of the microelectrode cell. The self-contained structure contains all electrical circuits (including the control circuit, flip-flops, the droplet detection circuit, and the actuation driver) in the area directly beneath the physical microelectrode as illustrated in Figure 3.6. The design goal of the microelectrode cell is to implement the standard cell approach. The first necessary step for the goal is to modularize the microelectrode cell design by the self-contained structure. The modular design of the microelectrode cell through the self-contained structure directly provides the scalability in the fabrication of the microelectrode array.

The size and the shape of the physical microelectrode are important design aspects of the self-contained structure. The minimum size of the physical microelectrode is defined by the area needed to contain all electrical circuits. The shape of the physical microelectrode also has impacts on the design of the self-contained structure because a microelectrode with the hexagonal or jagged shape would have a higher geometrical complexity in containing circuitries.

In the long term, this self-contained structure of the microelectrode cell will be responsible for providing accurate 3-D geometrical modeling and physical-level simulations, which are key elements in implementing top-down design automation for DMFBs. To reflect the importance of the modular design of the microelectrode cell, basic design steps are illustrated as follows.

The step one is to design the microelectrode cell in the form of a transistor netlist which implements required functions and relevant parameters. This netlist is generally represented in a schematic view that can be generated with many CAD/EDA programs. A simulation tool, usually "simulation program with integrated circuit emphasis" (SPICE), is then used to simulate the behavior of the netlist. The simulations verify whether the design meets the functional and timing requirements.

The second step is to design the physical representation, the layout view, of the microelectrode cell. The layout view is the closest physical design to an actual fabrication blueprint of the microelectrode cell. The layout of the microelectrode cell is organized into microelectrode layers, base layers, interconnect wiring layers and via layers. Microelectrode layers, as illustrated in Figure 3.6, are the physical microelectrode layer (the outmost metal layer) and the shielding layer (the next metal layer). The base layers are for transistors, and interconnect wiring layers and via layers create interconnections to join together the entire circuit. One of the key design tasks in this design step is to decide the size and shape of the physical microelectrode to ensure the self-contained structure. After the layout of the microelectrode cell is created, a set of common validations are performed to verify the layout.

The last design step is to check inter-cell connections and system timing. After the design of the individual microelectrode cell is done, the layout of the microelectrode cell is duplicated to form the microelectrode array based on the die size and the desired array formation. Inter-cell

connections are added and checked. Then signal propagation delays are simulated again for the entire chip.

3.6 Other System Design Considerations

3.6.1 Scalability Considerations

The MEDA architecture can be implemented by using the typical DMFB system structure with scaled-down EWOD electrodes. The scaling model of the MEDA architecture mainly depends on the studies of scaling models of EWOD droplet actuations by Song et al. [142] and Berthier [12]. Based on their studies, reliable EWOD actuations for scaled DMFBs are possible as long as they are within the working range of the Lippmann–Young equation. From the discussion of "Working Range of Electrowetting on Dielectric" in Section 2.1.4, the most important constraints of EWOD actuations are: (1) the saturation limit (V_{max}) of the EWOD effect at high voltages, and (2) the threshold voltage (V_{min}) which hinders droplet movements at low voltages. EWOD actuations are only effective between the two limits: V_{max} and V_{min}. The threshold voltage V_{min} for the EWOD droplet actuation, based on equation (3-1) [12], is defined mainly by the filler medium, which can reduce both the hysteresis angle α and the interface tension γ, and consequently decreases the value of V_{min}. For a given filler medium, a larger capacitance C, which is decided by the thickness and the dielectric constant of the dielectric layer, would yield a smaller value of V_{min}. Also, a very hydrophobic solid surface (large Young angle θ_0) can contribute to a small value of V_{min}.

$$V_{min} \approx 2\sqrt{\gamma\alpha \sin\theta_O / C}\,. \tag{3-1}$$

The upper limit of the actuation voltage V_{max} can be calculated by using equation (2-24). For different filler media (air and silicone oil), the values of V_{max} are basically the same [12]. What equation (2-24) does not deal with is the minimum 3-electrode cutting voltage, which could

exceed V_{max}. The minimum 3-electrode cutting voltage is a function of the aspect ratio and the filler medium. Aspect ratio is the ratio of gap height d and CMA length L, and typically d/L is smaller than 1 in DMFBs. The minimum 3-electrode cutting voltage for an oil medium is always less than V_{max} when $d/L < 1$. Nonetheless, for an air medium, to keep the minimum voltage for 3-electrode cutting less than V_{max}, d/L cannot be larger than 0.4 ($d/L < 0.4$). This suggests that reliable 3-electrode droplet cutting sets some limits on the aspect ratio, and cutting in air requires tighter limits. Since droplet creating is cutting droplets from the reservoir, similar conclusions apply to droplet creating [142].

Song et al. [142] showed that scaling of droplet cutting and creating depends on the number of $[t/\varepsilon\,(d/L)]^{1/2}$, where t and ε are dielectric layer thickness and constant, respectively. The model means that EWOD actuations would work properly in a scaled-down system, as long as the gap height d can be scaled down proportionally with the electrode length L. This assumes that the dielectric layer (t/ε) is unchanged, and (d/L) keeps the same so that $t/\varepsilon\,(d/L)$ is constant [142].

3.6.1.1 Microelectrode Shape and Spacing

Physically, there are many ways to design microelectrodes. They can be square, rectangular, hexagonal, jagged or other shapes. The reduced force from the spacing should be minimized by reducing the spacing or increasing the effective length of the contact line, such as the interdigitated electrodes [143]. The spacing/length ratio s/L is the ratio of the spacing and the CMA length. The smaller the spacing/length ratio, the stronger the EWOD actuation force. This spacing/length ratio should also be included in the scaling of the MEDA architecture. The design guideline for the MEDA architecture is $s/L \leq 0.1$. Based on experimental results of this research, all basic and advanced microfluidic operations have performed smoothly under this s/L ratio.

3.6.1.2 Scalability of Microelectrode Size

Although the smallest size of the microelectrode is not well defined at this moment, it is not recommended to go below 30 μm. Based on empirical data, for $L \leq 30$ μm, the implementation of the MEDA microelectrode cell would be very difficult even if using 0.18 micron CMOS fabrication process. Also, it is becoming more difficult to follow scaling design guidelines, such as the aspect ratio d/L and the spacing/length ratio s/L, for the system design. In addition, scaling the microelectrode should also consider the concentration level of analytes or bio-markers in samples to maintain a meaningful detection. Overall, a 30 μm microelectrode length should provide enough resolution to form CMAs for typical droplets, which are around 1 mm in diameter. Therefore, the design guideline for the microelectrode length is: $L \geq 30$ μm.

3.6.2 Cover Structures

The cover structure is an important design factor for microfluidic operations. The design of the cover structure should be done as an essential part of MEDA-architecture microsystems and it should not be treated as an afterthought.

3.6.2.1 Dielectric Layer for the Cover Plate

In general, the MEDA architecture does not suggest a dielectric layer for the cover plate. The dielectric layer should only be applied to the bottom plate. All the modeling and simulations for the MEDA architecture were based on no cover dielectric layer.

3.6.2.2 Dynamic Aspect Ratios

There are two most important aspect ratio design guidelines ($d/L < 1$ for oil medium, and $d/L \leq 0.4$ for air medium) for the MEDA architecture to keep cutting voltages less than V_{max}. The complication comes from the dynamic configurability of CMAs. The sizes of CMAs can be varied in a wide range in a microsystem, so a fixed gap height would mean a set of very different aspect ratios for the system. Therefore, MEDA-architecture microsystems should be designed in

such a way that all possible droplet sizes are factored into the calculations of aspect ratios in order to meet the aspect ratio design guidelines for the entire system.

3.6.3 Microsystem Packaging

Ideally, MEDA-architecture microsystems should physically be in a monolithically integrated way. In reality, sample collection, sample pre-treatment, and reagent loading are challenging due to the huge size discrepancy between real world samples (microliters) and DMFB droplets (nanoliters). Loading samples and reagents onto the biochip typically involves a special interface between the outside world and the DMFB. A fluidic interface platform, which allows a seamless and simple integration of different fluidic modules for MEDA-architecture microsystems, is highly desirable. One possibility is the "Inter-Chip Bridge" [73] (details in Appendix A), which enables the seamless and simple integration of fluidic modules by its inter-chip droplet transport capabilities. This fluidic interface technology provides a viable modular DMFB design solution before a monolithically integrated DMFB can be achieved. In a modular system design, the DMFB system can be partitioned into different function modules, which are then packaged together by the fluidic interface platform. This modular DMFB design not only solves immediate sample-reagent loading issues but also has advantages in flexibility and reliability. Moreover, incompatible modules, such as glass-based and CMOS-based, could be combined into a DMFB microsystem for heterogeneous integration. Consequently, the microsystem can be optimized (technical or cost wise) to a much better solution than if it were built only on CMOS technology.

3.6.4 Timing of Control Signals

Based on the daisy-chained control structure, the sequence and timing of each control step is critical for the performance of MEDA-architecture microsystems. Figure 3.7 illustrates the timing sequence of the droplet actuation cycle. The actuation cycle starts with a Detection/Control window as soon as an actuation cycle is triggered by a system event. During

this Detection/Control window, the high voltage signal applied to the microsystem is disabled and the control circuit is placed in the detection mode. In the detection mode, droplet detection is performed by every microelectrode. The individual droplet detection result is then clocked into the shift-register and becomes the 1-bit Map Data for each microelectrode. All droplet detection results are serially clocked out from the shift registers to form a droplet location map. The microfluidic operation manager uses the droplet location map for deciding the next actuation control data. If not all of the droplets are in the desired locations, the last actuation cycle might be executed again. Otherwise, 1-bit Cell Data are generated for each microelectrode and the actuation control data is loaded into the shift-registers serially. When the high voltage signal on the top plate is enabled again, the loaded 1-bit Cell Data determine the activation or deactivation of each microelectrode.

Depending upon the clock speed, the data loading of the daisy-chained registers can be very fast in comparison with the time scale (several hundred ms) of physical movements of droplets. Typically, a total Detection/Control window time less than 10 ms, which is in the range of a

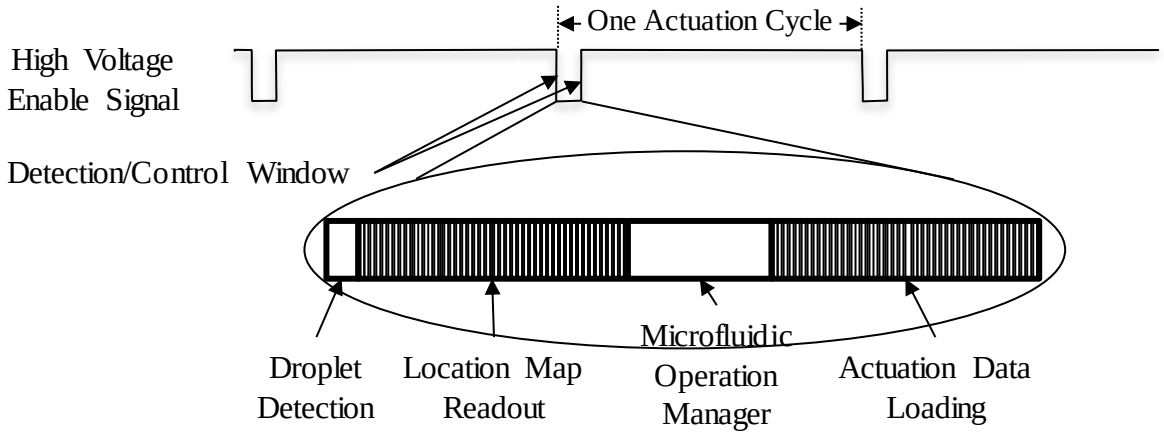

Figure 3.7. Timing diagram of droplet actuation cycles of the MEDA architecture.

mechanical relay settling time (about 6 ms), is very acceptable. Practically, using mechanical relay boxes for sequencing actuation voltages to ITO-glass based or other EWOD microfluidic systems is a very common practice in performing microfluidic operations. To meet the timing requirement for larger-scale DMFBs, higher frequency clocks can be used to handle the loading and readout. A 10 MHz clock, which is not considered as a very high frequency in modern electrical circuit design, can read/write 50-kilobit data in 10 ms.

3.7 Design Guidelines of the Microelectrode Dot Array Architecture

1. The threshold voltage V_{min} for the EWOD droplet actuation is defined mainly by the filler medium. For a given filler medium, a larger capacitance, which is decided by the thickness and the dielectric constant of the dielectric layer, would yield a smaller value of V_{min}. Also, a very hydrophobic solid surface can contribute to a small value of V_{min}.
2. The upper limit of the applied voltage V_{max} is associated with contact-angle saturation. For different filler media (air and silicone oil), the values of V_{max} are basically the same. For an oil medium, MEDA-architecture microsystems should keep the aspect ratio $d/L < 1$, so that cutting voltages are less than V_{max}. For an air medium, MEDA-architecture microsystems should keep $d/L \leq 0.4$, so that cutting voltages are less than V_{max}.
3. Scaling of droplet cutting and creating depends on the number of $[t/\varepsilon\,(d/L)]^{1/2}$. The model means that EWOD actuations would work properly in a scaled-down system, as long as the gap height d can be scaled down proportionally with the electrode length L. This assumes that the dielectric layer (t/ε) is unchanged, and (d/L) keeps the same so that $t/\varepsilon\,(d/L)$ is constant.
4. Due to the dynamic configurability of CMAs, the sizes of CMAs can be varied in a wide range in a microsystem, so a fixed gap height would mean a set of very different aspect ratios

for the system. Therefore, MEDA-architecture microsystems should be designed in such a way that all possible droplet sizes are factored into the calculations of aspect ratios in order to meet the aspect ratio design guidelines for the entire system.

5. The reduced force from the spacing should be minimized by reducing the spacing or increasing the effective length of the contact line. The spacing/length ratio *s/L* is the ratio of the spacing and the CMA length. The smaller the spacing/length ratio, the stronger the EWOD actuation force. The design guideline is: $s/L \leq 0.1$.
6. Although the smallest size of the microelectrode is not well defined at this moment, it is not recommended to have the length of the microelectrode below 30 μm; that is: $L \geq 30$ μm.
7. The total time of data loading and readout of the daisy-chained registers needs to be controlled so that it does not exceed a maximum total Detection/Control window time. If necessary, the clock speed of the daisy-chained control needs to be increased to meet the time requirement. A total Detection/Control window time should be less than 10 ms.

3.8 Modeling of the Microelectrode Dot Array Architecture

The main purpose for this modeling was to understand the significance of the shape and spacing of microelectrodes in droplet actuations. Modeling and simulations were also used as tools to understand EWOD actuation behaviors of the MEDA architecture. In the discussions of modeling, the methodology of modeling is introduced first. Then, energy-based modeling and contact-line-effective-length-based modeling in conjunction with a square droplet are covered in the subsequent two subsections. Numerical simulations are covered in Subsection 3.8.4 for both square and circular droplets. The impact from different spacing/length ratios is studied in Subsection 3.8.5. MEDA droplet motion simulation results are presented in Subsection 3.8.6 and then a summary is given in the last subsection.

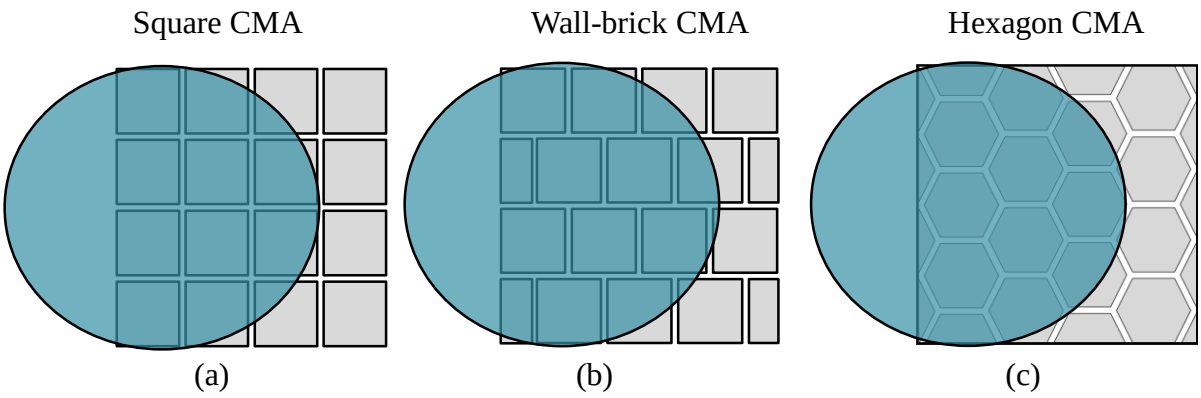

Figure 3.8. Three different CMAs studied for the MEDA architecture: (a) the square CMA is composed of square microelectrodes; (b) the wall-brick CMA is composed of square microelectrodes in the wall-brick layout; (c) the hexagon CMA is composed of hexagon microelectrodes.

3.8.1 Methodology of Modeling

Square CMA (Figure 3.8(a)), wall-brick CMA (Figure 3.8(b)) and hexagon CMA (Figure 3.8(c)) were studied in modeling. The EWOD droplet actuation force of the MEDA architecture is expected to be different from a solid electrode as a result of the spacing between microelectrodes. Two different modeling approaches (energy-based modeling and contact-line-effective-length-based modeling) were performed. MATLAB was used as a software tool to implement the numerical simulations. The methodologies of modeling and simulations are listed as following:

1. The focus of modeling was on the study of the EWOD droplet actuation force of the MEDA architecture. The main effort of modeling was to find the model best suitable for the architecture so that the impacts from the spacing could be examined carefully. The effort of droplet motion modeling was not aimed at a better droplet motion model. Instead, the goal was to develop a simplified motion model, which was capable of presenting the simulated droplet actuation forces into a measureable format, such that predicated droplet actuation behaviors could be compared with actual experimental results.

2. Both analytical modeling and numerical modeling were performed in the study. Some assumptions were made to make modeling possible. For example, the droplet was assumed to move as a rigid body so that it maintained its shape during the transition. The effects of the dynamic contact angle and the dynamic droplet shape during the transition were not taken into account in the simulations. In addition, droplets being in perfect square or circular shapes in conjunction with physically perfect electrodes and CMAs were assumed.
3. A perfect square-shaped droplet was used for both analytical modeling and numerical modeling. Although a perfect square-shaped droplet might not be realistic, it approximated the actuated droplet better than a circular droplet. More importantly, it made analytical modeling possible in dealing with the geometrical complexities associated with different CMAs. As analytical modeling was only possible by using the perfect square-shaped droplet, two analytical modeling approaches (energy-based modeling and contact-line-effective-length-based modeling) were performed first. The results were then compared and confirmed by numerical simulations. Crosschecking between analytical modeling and numerical simulations by using the square droplet provided a solid foundation for more complicated simulations of actuation forces and speeds in the study of the MEDA architecture.
4. Because the main modeling purpose was to understand the performance impact from the MEDA architecture, the modeling performances of a solid electrode defined the baselines for all modeling measurements. All modeled actuation forces/speeds of different CMAs were only studied with comparisons to the baselines. Modeling of the solid electrode was for the purpose of comparisons, but not for the fundamental EWOD actuation study of a conventional (solid) electrode.

Table 3-1. Physical numbers used in modeling of the MEDA architecture.

Descriptions	Dimensions
Size of the square microelectrode	100 µm × 100 µm
Size of the hexagon microelectrode	57.735 µm for all six sides
Spacing between microelectrodes	10 µm
Height of CMA	1090 µm
Width of CMA	1090 µm
Height (# of microelectrodes)	10
Width (# of microelectrodes)	10
Travel distance of the droplet	1090 µm
Size of the square droplet	1090 µm × 1090 µm
Radius of the circular droplet	545 µm
s/L for ITO-glass prototypes	0.1
s/L for FPLOC prototypes	0.027

5. Although general cases were described in analytical modeling, eventually a set of real numbers (Table 3-1) were plugged in for the numerical computations of the force and speed distributions. This set of numbers reflected the physical dimensions of the fabricated ITO-glass based prototypes so that comparisons and analyses between the simulated numbers and the experimental data could be performed.

3.8.2 Energy-Based Model

The energy-based model from Bahadur and Garimella's paper [76] was modified to model the MEDA architecture because its formulation is in terms of derivatives of the droplet-electrode covered area and the actuation voltage. The modified model can be extended to any specified shapes of droplets and CMAs during the droplet transition. In modeling the MEDA architecture, the actuation voltage was fixed, and the area derivatives during the droplet transition can be calculated analytically or numerically.

The DMFB shown in Figure 3.9(a) has two plates separated by a gap d. Actuation microelectrodes are fabricated on the bottom plate such that two square equal-sized CMAs are

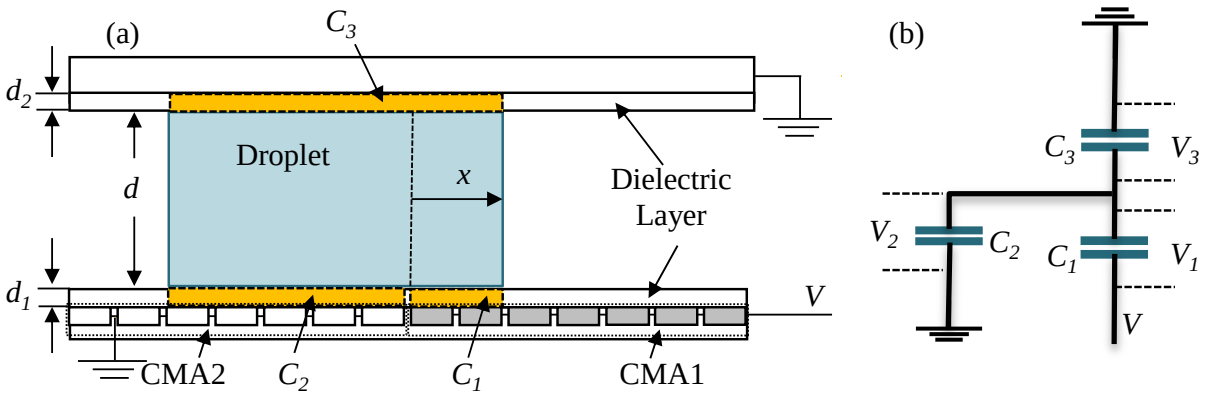

Figure 3.9. Energy-based modeling for the MEDA architecture: (a) side view schematic diagram of an actuated droplet, and (b) the capacitive circuit model for calculating voltages across dielectric layers.

configured. The top plate has a single electrode plane. Both plates have a dielectric layer and a thin hydrophobic layer. The square droplet is sandwiched between two plates with the droplet length set equal to the CMA width. An actuation V applied to CMA1 on the bottom plate. CMA2 on the bottom plate and the top plate electrode are grounded. The thicknesses of dielectric layers are d_1 and d_2. The droplet moves toward the activated CMA1, and the traveling distance is indicated by the droplet position x. The droplet is electrically conductive and is surrounded by silicone oil or air.

This energy-based model analyzes the static surface energy of a droplet during the transition. The EWOD actuation force on the droplet can be calculated from the negative derivative of the energy. Based on the discussion of the Lippmann-Young equation in Chapter 2, the amount of solid-liquid interfacial energy reduced is related to the amount of electric energy across the dielectric layers. The amount of electric energy across the dielectric layers can be calculated through a modeled capacitive circuit of the system. An equivalent capacitive circuit, which represents the EWOD microsystem, is shown in Figure 3.9(b). Three parallel-plate capacitors are connected together by the droplet, which is assumed to be perfectly conductive, to form the

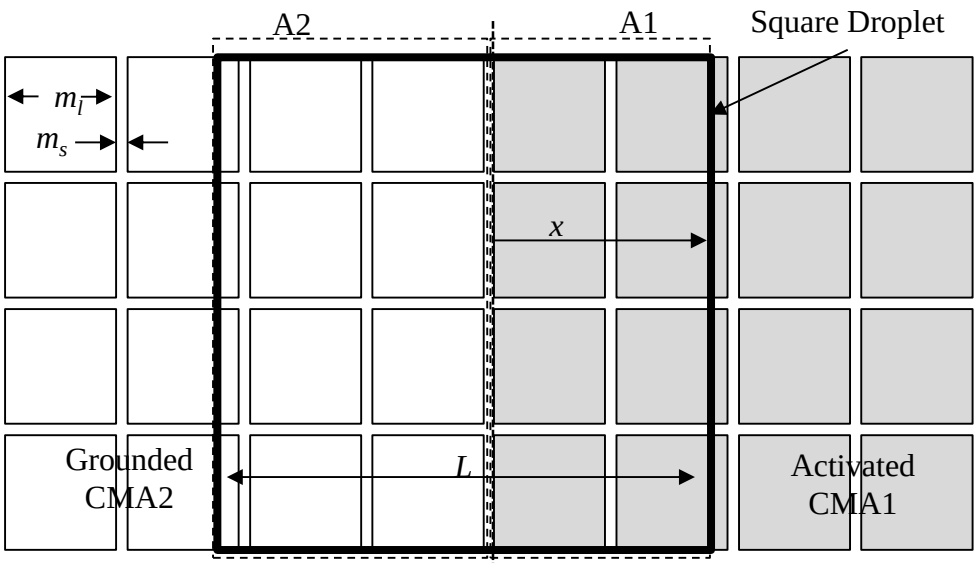

Figure 3.10. Top view of a square droplet undergoing EWOD actuated transition. Two CMAs, which composed of 4 × 4 microelectrodes, are shown as CMA1 and CMA2.

capacitive circuit. In typical DMFBs, the thickness of the EDL is much thinner than the thickness of the dielectric layer so that voltage drops within the droplet are negligible. Consequently, the voltage drops fall only across the dielectric layers. The fringing effects at the sides of the three parallel-plate capacitors are negligible for modeling. The capacitances of the three capacitors are

$$C_1(x) = \frac{k_1 A_1(x) \varepsilon_0}{d_1} \ , \tag{3-2}$$

$$C_2(x) = \frac{k_1 A_2(x) \varepsilon_0}{d_1} \ , \tag{3-3}$$

$$C_3(x) = \frac{k_2 A_3(x) \varepsilon_0}{d_2} \ , \tag{3-4}$$

where k_1, k_2, d_1, and d_2 are dielectric constants and thicknesses of the lower and upper dielectric layers respectively (Figure 3.9(a)). C_1 is the dielectric layer capacitance with area A_1, which is the area covered by the droplet and the activated CMA1 of the bottom plate (Figure 3.10). C_2 is the dielectric layer capacitance with area A_2, which is the area covered by the droplet and the

deactivated CMA2 of the bottom plate. C_3 is the dielectric layer capacitance between the top plate and the droplet (Figure 3.9(a)). From the capacitive circuit, the voltage drops of the three capacitors are

$$V_1(x) = \frac{(C_2 + C_3)V}{(C_1 + C_2 + C_3)} \quad , \tag{3-5}$$

$$V_2(x) = V_3(x) = \frac{C_1 V}{(C_1 + C_2 + C_3)} \, . \tag{3-6}$$

According to Lippmann's equation (equation (2-15)), the solid-liquid interfacial tension γ_{SL} can be controlled by the electric potential V across the interface, so the sum of all interfacial energies is the droplet actuation energy

$$E(x) = \left(\gamma_{SL} - \frac{k_1 \varepsilon_0 V_1^2}{2d_1}\right) A_1 + \left(\gamma_{SL} - \frac{k_1 \varepsilon_0 V_2^2}{2d_1}\right) A_2 + \left(\gamma_{SL} - \frac{k_2 \varepsilon_0 V_3^2}{2d_2}\right) A_3 + \gamma_{LF} A_{LF} \, , \tag{3-7}$$

where γ_{SL} is the solid-liquid interfacial tension. γ_{LF} is the liquid-filler-medium interfacial tension, and A_{LF} is the liquid-filler-medium interfacial area, which remains unchanged during the transition. The EWOD actuation force $F_{act}(x)$ on the droplet can be derived from the negative derivative of the energy $E(x)$ as a function of x [76],

$$F_{act}(x) = -\frac{dE(x)}{dx} , \tag{3-8}$$

$$F_{act}(x) = F_1(x) + F_2(x) + F_3(x) \, , \tag{3-9}$$

$$F_1(x) = \frac{k_1 \varepsilon_0 V_1^2}{2d_1} \frac{dA_1}{dx} + \frac{k_1 \varepsilon_0 V_1 A_1}{d_1} \frac{dV_1}{dx} , \tag{3-10}$$

$$F_2(x) = \frac{k_1 \varepsilon_0 V_2^2}{2d_1} \frac{dA_2}{dx} + \frac{k_1 \varepsilon_0 V_2 A_2}{d_1} \frac{dV_2}{dx} \, , \tag{3-11}$$

$$F_3(x) = \frac{k_2 \varepsilon_0 V_3 A_3}{d_2} \frac{dV_3}{dx} . \tag{3-12}$$

These forces are contributed from the change rates of both area and voltage along the coordinate *x*. In this research, there is no dielectric layer of the top plate. So, for subsequent discussions, the actuation effect of the top dielectric layer is ignored. For $d_2 = 0$, $V_1(x) = V$ and $V_2 = V_3 = 0$, the EWOD actuation force for the energy-based analysis results in

$$F_{\text{act}}(x) = \frac{k_1 \varepsilon_0 V^2}{2d_1} \frac{dA_1}{dx} \ . \tag{3-13}$$

For a square droplet, the rate of area (A_1) change along *x* is the concern during the entire transition. Assuming k_1, ε_0, V and d_1 are unchanged during the transition, then $F_{\text{act}}(x)$ is proportional to the rate of change of area A_1 (Figure 3.10). Because of the geometrical repeatability of microelectrodes in CMAs, the force distribution is expected to be periodic. So the base period of the distribution curve was analyzed then the results were duplicated to complete the full distribution curve. The technique of analytical modeling was to identify the base period of each CMA so that the base period can be further divided into different regions for the analysis.

For square CMAs, the base period is shown by the thick red line, and it is divided into two regions as shown in Figure 3.11(a). The area of each region $A_{1\text{r}}(x)$ is a function of *x*, where r is the region number. The two area functions associated with the two regions can be expressed as

$$A_{11}(x) = nm_l x \qquad \text{(Region 1)}, \tag{3-14}$$

$$A_{12}(x) = nm_l^2 \qquad \text{(Region 2)}, \tag{3-15}$$

where *n* is the number of microelectrodes in the column of square CMAs. For example, in Figure 3.11(a) $n = 4$. m_l is the length of the microelectrode. The derivatives of the above two equations are

$$\frac{dA_{11}(x)}{dx} = nm_l \qquad \text{(Region 1)}, \tag{3-16}$$

$$\frac{dA_{12}(x)}{dx} = 0 \qquad \text{(Region 2).} \qquad (3\text{-}17)$$

As mentioned before, all modeled numbers were compared to the actuation force of the solid electrode. For a solid electrode with a square droplet during the transition, the area change along x is $A_1(x) = Lx$ where L is the electrode length. And the actuation force is the derivative of $A_1(x)$, which is a constant $dA_1/dx = L$. Applying the numbers in Table 3-1 and taking the percentage of the actuation forces of the solid electrode, the results of the square CMA are plotted in Figure 3.12. In the figure, the solid electrode (blue solid line) has a constant value of 100%. The Square CMA (double green line) has 92% strength when the leading edge of the square droplet is not in the spacing between microelectrodes. However, the actuation force drops to zero when the leading edge is in the spacing.

For wall-brick CMAs, the base period was divided into four regions for the actuation force analysis as indicated in Figure 3.11(b). Area functions $A_{1r}(x)$ for the wall-brick CMA are

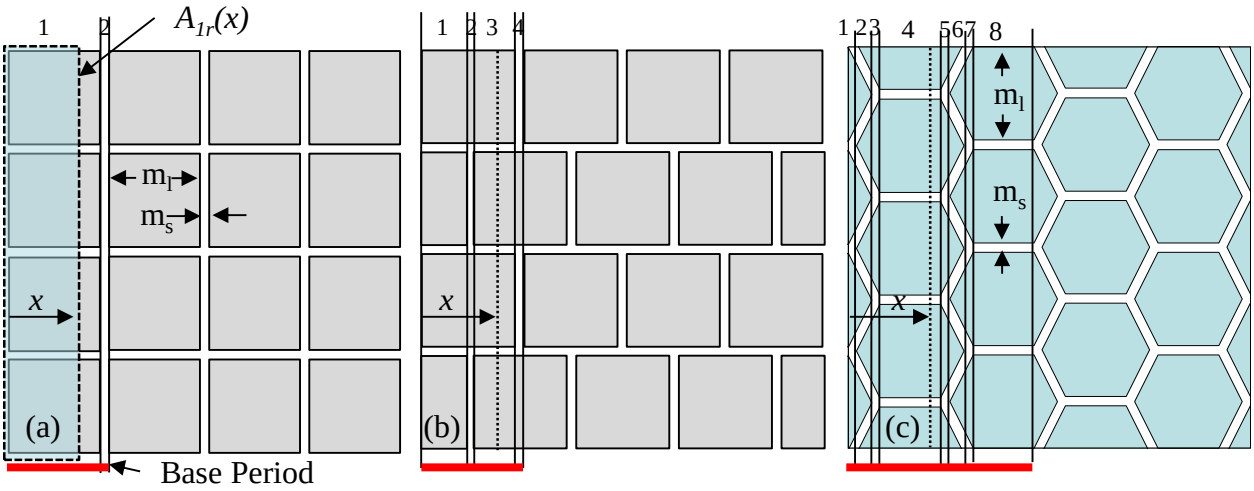

Figure 3.11. Analytical region partitions for CMAs: (a) square CMAs (2 regions); (b) wall-brick CMAs (4 regions); (c) hexagon CMAs (8 regions).

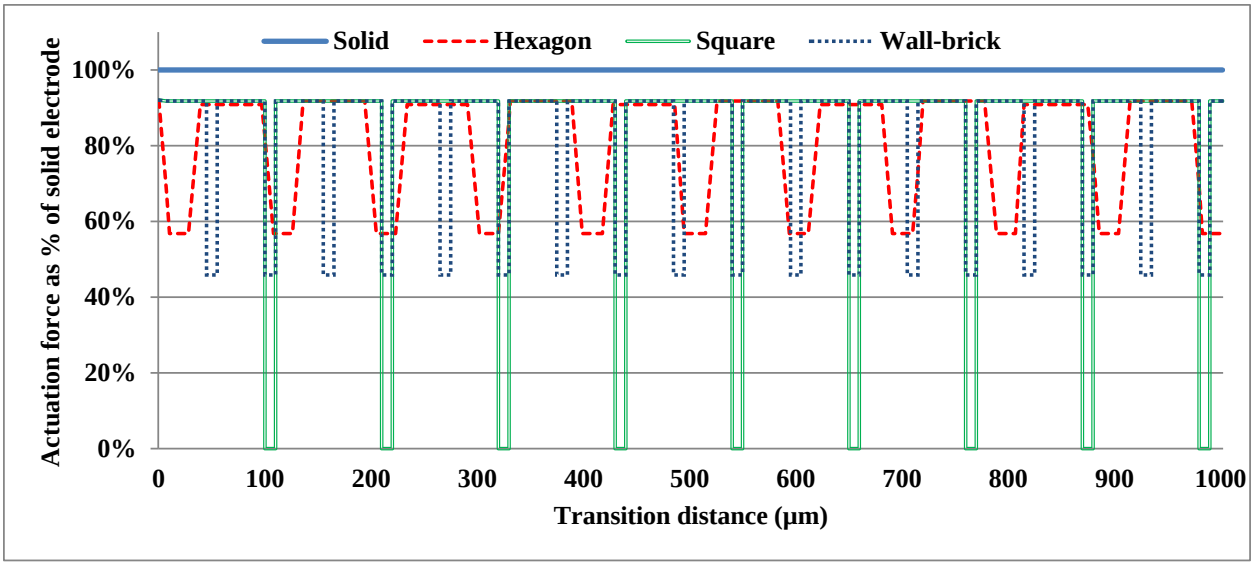

Figure 3.12. Actuation force distributions of the square droplet by the energy-based model. The x-axis is the distance traveled by the droplet. The y-axis is the actuation force in the percentage of the solid electrode. Numbers in Table 3-1 were used for the actuation force calculations.

$$A_{11}(x) = nm_l x \quad \text{(Region 1)}, \tag{3-18}$$

$$A_{12}(x) = \frac{1}{2} nm_l \left(x - \frac{1}{2}(m_l - m_s)\right) \quad \text{(Region 2)}, \tag{3-19}$$

$$A_{13}(x) = nm_l \left(x - \frac{1}{2}(m_l + m_s)\right) \quad \text{(Region 3)}, \tag{3-20}$$

$$A_{14}(x) = \frac{1}{2} nm_l (x - m_l) \quad \text{(Region 4)}. \tag{3-21}$$

The derivatives of these equations are:

$$\frac{dA_{11}(x)}{dx} = nm_l \quad \text{(Region 1)}, \tag{3-22}$$

$$\frac{dA_{12}(x)}{dx} = \frac{1}{2} nm_l \quad \text{(Region 2)}, \tag{3-23}$$

$$\frac{dA_{13}(x)}{dx} = nm_l \quad \text{(Region 3)}, \tag{3-24}$$

$$\frac{dA_{14}(x)}{dx} = \frac{1}{2} nm_l \quad \text{(Region 4)}. \tag{3-25}$$

Table 3-2. The boundaries of the eight regions for the actuation force analysis of hexagon CMAs.

$0 <$ Region $1 \leq d_1$	$d_1 <$ Region $2 \leq d_{12}$
$d_{12} <$ Region $3 \leq (d_{12} + d_1)$	$(d_{12} + d_1) <$ Region $4 \leq (3d_{12} + d_1)$
$(3d_{12} + d_1) <$ Region $5 \leq (3d_{12} + 2d_1)$	$(3d_{12} + 2d_1) <$ Region $6 \leq (4d_{12} + d_1)$
$(4d_{12} + d_1) <$ Region $7 \leq (4d_{12} + 2d_1)$	$(4d_{12} + 2d_1) <$ Region $8 \leq (6d_{12} + 2d_1)$

Applying the numbers in Table 3-1 and the blue dotted line in Figure 3.12 shows the actuation force distribution for the wall-brick CMA.

The hexagon CMA analysis was more complicated and difficult to present in details but the same analytical technique was applied to the analysis. Totally, eight regions (Figure 3.11(c)) were divided in the base period to analyze the hexagon CMA. As a pre-work, two key numbers for separating these eight regions were calculated,

$$d_1 = \left(\sqrt{4/3} - 1/12\right) m_s \qquad (0 \leq \text{Region } 1 < d_1), \tag{3-26}$$

$$d_{12} = \sqrt{(m_l/2)^2/3} \qquad (0 \leq \text{Region } 12 < d_{12}), \tag{3-27}$$

where d_1 is the length (x distance) of region 1 and d_{12} is the length of region 1 plus region 2. By using these two numbers, the boundaries of the eight regions were defined in Table 3-2.

Area functions $A_{1\mathrm{r}}(x)$ for the eight regions indicated in Figure 3.11(c) are

$$A_{11}(x) = n(m_l x - \sqrt{3}x^2) \qquad \text{(Region 1)}, \tag{3-28}$$

$$A_{12}(x) = (n\left(m_l - 2\sqrt{3}d_1\right) - m_s)(x - d_1) \qquad \text{(Region 2)}, \tag{3-29}$$

$$A_{13}(x) = (n\left(m_l - 2\sqrt{3}d_1\right) - m_s)(x - d_{12}) + \mathrm{n}\sqrt{3}(x - d_{12})^2 \qquad \text{(Region 3)}, \tag{3-30}$$

$$A_{14}(x) = (nm_l - m_s)(x - d_{12} - d_1) \qquad \text{(Region 4)}, \tag{3-31}$$

$$A_{15}(x) = (nm_l - m_s)(x - 3d_{12} - d_1) - \mathrm{n}\sqrt{3}(x - 3d_{12} - d_1)^2 \qquad \text{(Region 5)}, \tag{3-32}$$

$$A_{16}(x) = (n\left(m_l - 2\sqrt{3}d_1\right) - m_s)(x - d_1) \qquad \text{(Region 6)}, \tag{3-33}$$

$$A_{17}(x) = n\left(m_l - 2\sqrt{3}d_1\right)(x - 4d_{12} - d_1) + \mathrm{n}\sqrt{3}(x - 4d_{12} - d_1)^2 \quad \text{(Region 7)}, \tag{3-34}$$

$$A_{18}(x) = nm_l(x - 4d_{12} - 2d_1) \quad \text{(Region 8)}. \tag{3-35}$$

Then the derivatives of these equations are

$$\frac{dA_{11}(x)}{dx}(x) = n(m_l - 2\sqrt{3}x) \quad \text{(Region 1)}, \tag{3-36}$$

$$\frac{dA_{12}(x)}{dx} = n\left(m_l - 2\sqrt{3}d_1\right) - m_s \quad \text{(Region 2)}, \tag{3-37}$$

$$\frac{dA_{13}(x)}{dx} = n\left(m_l - 2\sqrt{3}d_1\right) - m_s) + \mathrm{n}2\sqrt{3}(x - d_{12}) \quad \text{(Region 3)}, \tag{3-38}$$

$$\frac{dA_{14}(x)}{dx} = nm_l - m_s \quad \text{(Region 4)}, \tag{3-39}$$

$$\frac{dA_{15}(x)}{dx} = (nm_l - m_s) - \mathrm{n}2\sqrt{3}(x - 3d_{12} - d_1) \quad \text{(Region 5)}, \tag{3-40}$$

$$\frac{dA_{16}(x)}{dx} = n\left(m_l - 2\sqrt{3}d_1\right) - m_s \quad \text{(Region 6)}, \tag{3-41}$$

$$\frac{dA_{17}(x)}{dx} = n\left(m_l - 2\sqrt{3}d_1\right) + \mathrm{n}2\sqrt{3}(x - 4d_{12} - d_1) \quad \text{(Region 7)}, \tag{3-42}$$

$$\frac{dA_{18}(x)}{dx} = nm_l \quad \text{(Region 8)}. \tag{3-43}$$

Applying the numbers in Table 3-1 and the red dash line in Figure 3.12 shows the actuation force distribution of the hexagon CMA.

3.8.3 Contact-Line-Effective-Length-Based Model

The second modeling approach was calculating the effective length of the contact line, which is discussed in Chapter 2. From equation (2-22), the calculation of the effective length $e(x)$, which is a function of the traveling distance x of the moving droplet, can be used to obtain the EWOD droplet actuation force F_x as

$$F_x = \gamma_{LG} \cos\theta(V) e\,(x). \tag{3-44}$$

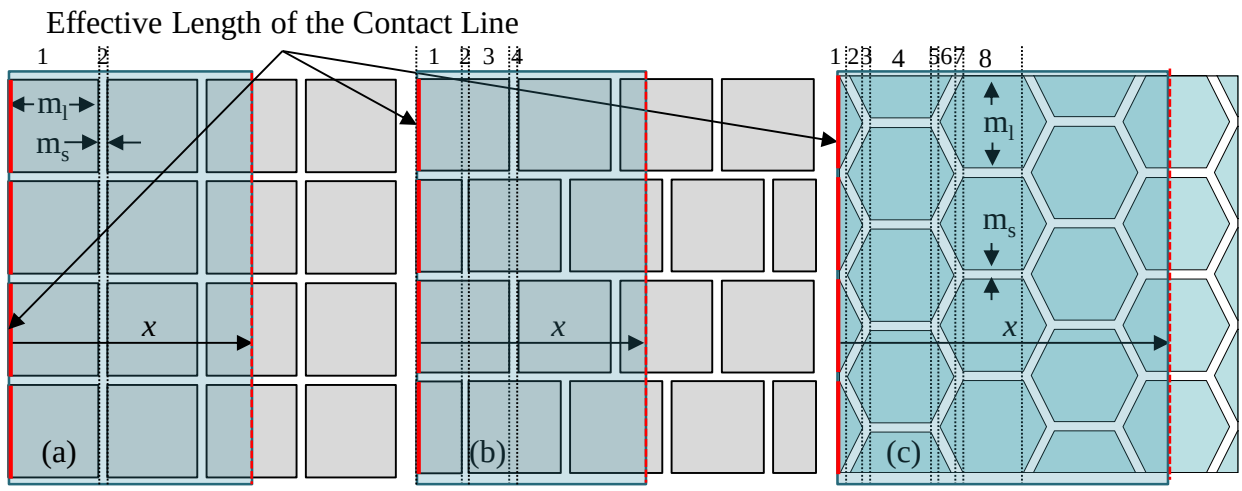

Figure 3.13. Effective lengths of contact lines: (a) Square CMAs, (b) Wall-brick CMAs, and (c) Hexagon CMAs.

γ_{LG} and $\cos\theta(V)$ are unchanged during the transition, thus F_x is proportional to the effective length $e(x)$. For a square droplet actuated by a solid electrode, the effective length of the contact line is a constant L, which is the electrode length, through the entire transition. From Figure 3.13(a), the effective lengths $e_n(x)$ in region n of square CMAs are

$$e_1(x) = nm_l \qquad \text{(Region 1)}, \qquad (3\text{-}45)$$

$$e_2(x) = 0 \qquad \text{(Region 2)}. \qquad (3\text{-}46)$$

The results (equations (3-45) and (3-46)) from the calculations of effective lengths of contact lines are identical to equations (3-16) and (3-17) from the energy-based modeling approach for square CMAs. From Figure 3.13(b), effective lengths $e_n(x)$ in region n of wall-brick CMAs are

$$e_1(x) = e_3(x) = nm_l \qquad \text{(Region 1,3)}, \qquad (3\text{-}47)$$

$$e_2(x) = e_4(x) = \frac{1}{2}nm_l \qquad \text{(Region 2,4)}. \qquad (3\text{-}48)$$

Again, equations (3-47) and (3-48) from the calculations of effective lengths of contact lines are identical to equations (3-22) to (3-25) from the energy-based modeling approach of wall-

brick CMAs. From Figure 3.13(c) and the help from the region boundaries defined in Table 3-2, the effective lengths $e_n(x)$ of hexagon CMAs are

$$e_1(x) = n(m_l - 2\sqrt{3}x) \quad \text{(Region 1)}, \tag{3-49}$$

$$e_2(x) = n\left(m_l - 2\sqrt{3}d_1\right) - m_s \quad \text{(Region 2)}, \tag{3-50}$$

$$e_3(x) = n\left(m_l - 2\sqrt{3}d_1\right) - m_s) + \text{n}2\sqrt{3}(x - d_{12}) \quad \text{(Region 3)}, \tag{3-51}$$

$$e_4(x) = nm_l - m_s \quad \text{(Region 4)}, \tag{3-52}$$

$$e_5(x) = (nm_l - m_s) - \text{n}2\sqrt{3}(x - 3d_{12} - d_1) \quad \text{(Region 5)}, \tag{3-53}$$

$$e_6(x) = n\left(m_l - 2\sqrt{3}d_1\right) - m_s \quad \text{(Region 6)}, \tag{3-54}$$

$$e_7(x) = n\left(m_l - 2\sqrt{3}d_1\right) + \text{n}2\sqrt{3}(x - 4d_{12} - d_1) \quad \text{(Region 7)}, \tag{3-55}$$

$$e_8(x) = nm_l \quad \text{(Region 8)}. \tag{3-56}$$

Predictably, equations (3-49) to (3-56) from the calculations of effective lengths of contact lines are identical to equations (3-36) to (3-43) from the energy-based modeling approach for hexagon CMAs. As presented by Nelson et al. [10], expressions for the EWOD driving force are interchangeable, i.e., Pressure force = Electrostatic force = Surface tension force. So it was not a surprise that the two models would have identical results.

3.8.4 Numerical Modeling

Two different models, the energy-based model (electrostatic force) and the contact-line-effective-length-based model (surface tension force), showed exactly same results of modeling the MEDA architecture based on an ideal square droplet. If both models could work then naturally the more convenient one was chosen for further numerical modeling. In modeling a circular droplet, MATLAB was used as a software tool to implement the numerical calculations of effective lengths of contact lines. The radius of the circular droplet was set as R = 545 μm which would match the CMA length of 1090 μm based on Table 3-1. Figure 3.14(a)

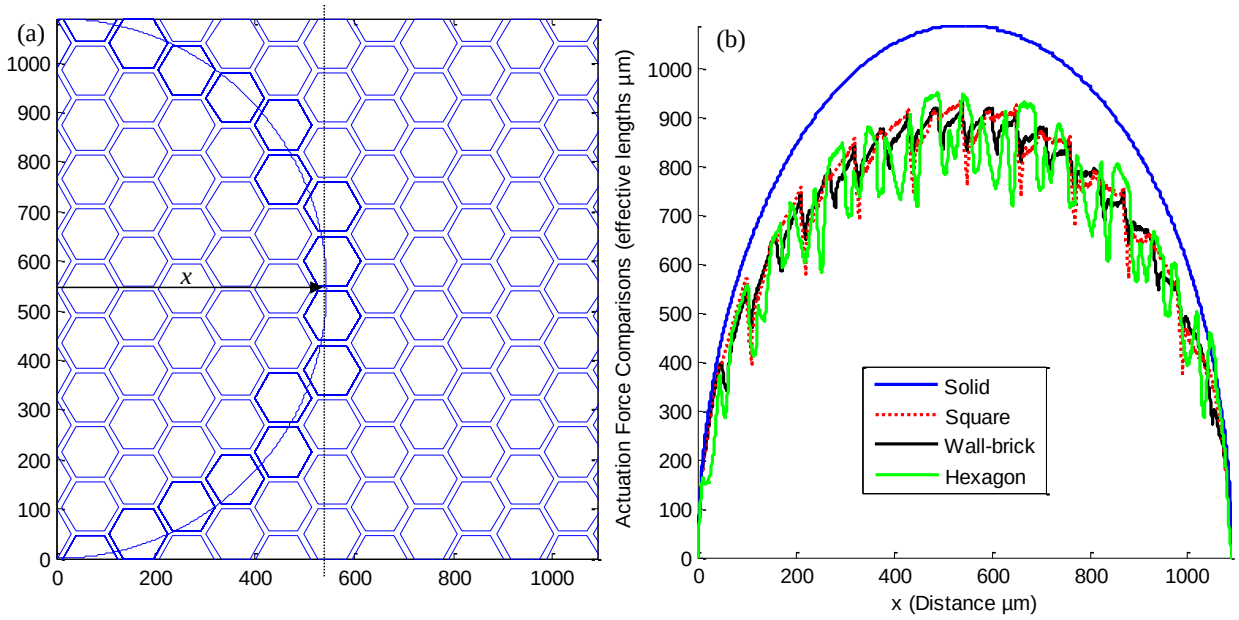

Figure 3.14. MATLAB calculation results of actuation force distributions of a circular droplet: (a) the snapshot of the circular droplet on the hexagon CMA; (b) comparisons of actuation force distributions. The blue curve at the top is the actuation force distribution of the solid electrode. The numbers of the y-axis are calculated effective lengths for actuation force comparisons.

shows a snapshot of a circular droplet moving onto a hexagon CMA with a traveling distance *x* of 545 µm. The blue curve at the top of Figure 3.14(b) is the actuation force distribution of the circular droplet on a solid electrode. Actuation force distributions of the three CMAs show parabolic trends similar to the blue curve, but complicated by the spacing between microelectrodes.

The same numerical simulation was applied to model the square droplet for the CMAs, and the results were identical to Figure 3.12. Crosschecking between analytical results and numerical results not only ensured the analytical model, but also verified the numerical simulations. In addition, simulations with a vertical direction droplet motion of the hexagon CMA were performed to verify the differences between the horizontal and vertical droplet actuations. Unlike the square CMA, geometrically the vertical pattern and the horizontal pattern of the hexagon CMA are different. Simulations showed that actuation force distributions, droplet speed

distributions and overall motion performances of both directions were very close (within 4%). Figures of these simulations are shown in Appendix B.

3.8.5 Spacing/Length Ratio Impacts Modeling

The simulation of the circular droplet was applied to model the impacts from different spacing and microelectrode length *s/L* ratios. There were five different *s/L* ratios (0, 0.027, 0.1, 0.2 and 0.4) were simulated with the three CMAs. *s/L* = 0 represented a solid electrode. *s/L* = 0.027 was simulated for the field-programmable lab-on-a-chip (FPLOC) design (*L* = 37.1 μm, *s* = 1 μm, and *s/L* = 0.027), and *s/L* = 0.1 was simulated for the *s/L* ratio of the ITO glass prototypes. Other *s/L* ratios (0.2 and 0.4) were for the purpose of comparisons. The aspect ratio of this simulation was kept at: *d/L* = 0.1.

From the results shown in Figure 3.15, the actuation performance impact by the *s/L* ratio is obvious. Defining the exact mathematical relationships between *s/L* ratios and actuation force distributions would be very difficult, but approximately the actuation force has a dependence on $(s/L)^{-1}$ for all three CMAs. The smaller the *s/L* ratio is, the stronger the actuation force of the MEDA architecture. Based on the simulations, with *s/L* = 0.027, the averaged actuation forces of the three CMAs exceeded 93% of the actuation force of the solid electrode (93%-of-solid). The upper bound of the actuation force distribution for CMAs can be approximated by $(1 - s/L)$%-of-solid. For example, when *s/L* = 0.027, the upper bound of the actuation force distribution is about 97.3%-of-solid. This upper bound limit might not be shown clearly in Figure 3.15, but it is definitely obvious in Figure 3.12. One possible way to analyze the distribution curves in Figure 3.15 is to separate the actuation force distribution curves into two components: one is the virtual base curve which resembles the parabolic arch of the solid electrode (*s/L* = 0) and has an approximate dependence on $(s/L)^{-1}$; another is the strayed distributions from the base curve. All three CMAs had similar base curves, but the strayed distributions were very different especially

when *s/L* was bigger. It is noticeable that when *s/L* = 0.4, the wall-brick CMA had relatively small strayed distributions but the hexagon CMA had significant deviations. Further droplet motion simulations of *s/L* = 0.4 did confirm the performance degradation of the hexagon CMA under the big *s/L* ratio situation (Figure B-6).

3.8.6 Droplet Motion Modeling

A precise prediction of EWOD-actuated droplet motion depends on accurate assessments of the actuation forces and opposing forces. EWOD-actuated droplet motion is a complicated physical phenomenon driven by actuation forces and opposing forces. Natures of several of these opposing forces (surface tensions, shear forces, viscosity, dynamic contact angles, hysteresis, internal flow, etc.) are not well understood [12, 76]. The purpose of this droplet motion modeling was not aimed at developing a better droplet motion prediction model for conventional electrodes. Instead, the goal was to develop a simplified model which was capable of presenting the simulated droplet actuation forces into a more assessable format, such as the droplet velocity. Therefore, this droplet motion modeling was mainly based upon the foundation of droplet actuation force simulations, and the effects from opposing forces were simplified.

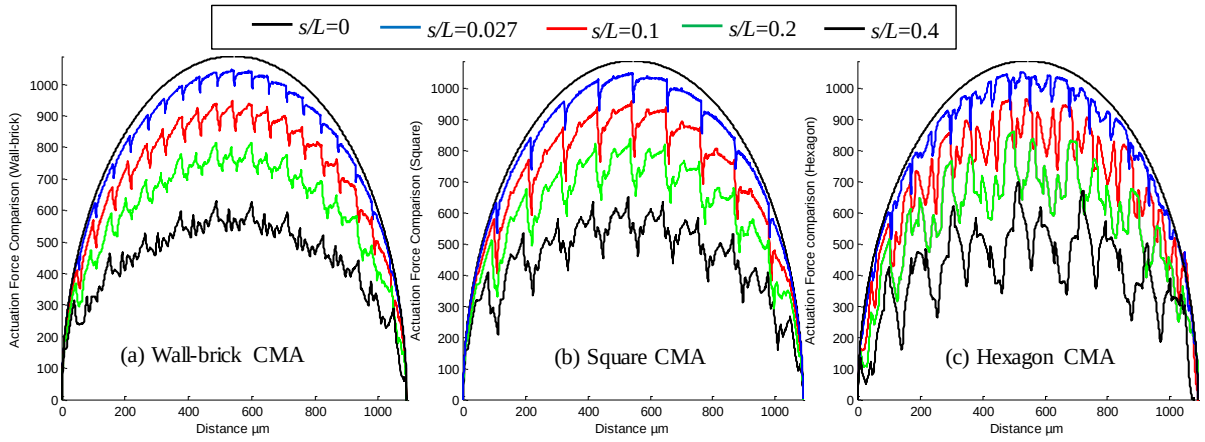

Figure 3.15. Actuation force distributions vs. *s/L* ratios: (a) wall-brick CMA, (b) square CMA, and (c) hexagon CMA.

3.8.6.1 Droplet Motion Model Description

All equations of the opposing forces for the simplified droplet motion model were based on Bahadur and Garimella's paper [76]. Nonetheless, parameters were adjusted, such as the contact-line friction coefficient, to make the model work for the study. Zero slip boundary conditions were applied to model the plate shear force. The total wall shear force from the two plates is expressed as [76]

$$F_w = \left(\frac{6\mu_l v}{d}\right)(2\pi r^2)\,, \tag{3-57}$$

where v is the droplet velocity, μ_l the liquid viscosity, d the gap height, and r the radius of the droplet. The viscous drag due to the filler medium was estimated by [76]

$$F_f = \left(\frac{1}{2}C_f \rho_f v^2\right)(2rd)\,, \tag{3-58}$$

where C_f is the drag coefficient, and ρ_f is the filler medium density. The total friction force of the contact-line was modeled by [76]

$$F_{cl} = (zv)(4\pi r)\,, \tag{3-59}$$

where z is a proportionality coefficient. The integrated equation of EWOD-actuated droplet motion is [76]

$$ma = m\frac{d^2x}{dt^2} = F_{act} - F_w - F_f - F_{cl}\,, \tag{3-60}$$

where m is the droplet mass, a the acceleration, and F_{act} the actuation force. Other equations incorporated in droplet motion simulations are also listed below,

$$r = r_0 + \left(\frac{v + v_0}{2}\right)t \quad , \tag{3-61}$$

$$v^2 = v_0^2 + 2a(r - r_0)\,, \tag{3-62}$$

where v_0 and r_0 are the initial velocity and position of the droplet; v and r are the velocity and position after time t with acceleration a.

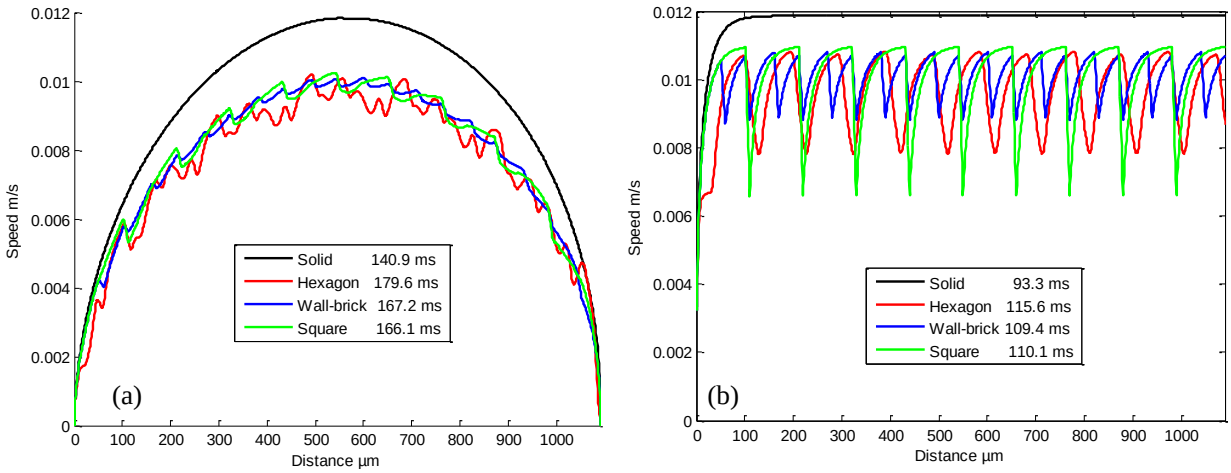

Figure 3.16. Simulated speed distributions (d = 100 µm): (a) circular droplet; (b) square droplet.

3.8.6.2 Droplet Motion Simulation Results

Simulations of droplet motion were performed to obtain droplet positions, speed distributions and total times for droplets to travel a distance of 1090 µm. Water droplets were assumed in simulations, and the filler medium was assumed to be air. Both square and circular droplets were simulated along with the three CMAs. During the EWOD actuation, the droplet moves toward the actuated CMA, and stops moving when its center reaches the center of the activated CMA. To model this droplet motion transition, the parameters for the contact-line friction force and the wall shear force from the top and bottom plates were optimized to make the initial speed = 0 and the end speed = 0 as shown by the black curve (the solid electrode) in Figure 3.16(a). Unfortunately, this approach was not possible for modeling the square droplet. The square droplet would oscillate around the vertical center line of the actuated CMA before coming to stop. This oscillatory behavior would be prevented by the threshold voltage V_{min}, which is covered in Section 2.1.4, under actual experimental conditions.

Figure 3.16 shows speed distributions of two droplet types moving across a 1.09-mm distance under EWOD actuations. Figure 3.16(a) shows the speed distributions of the circular droplet

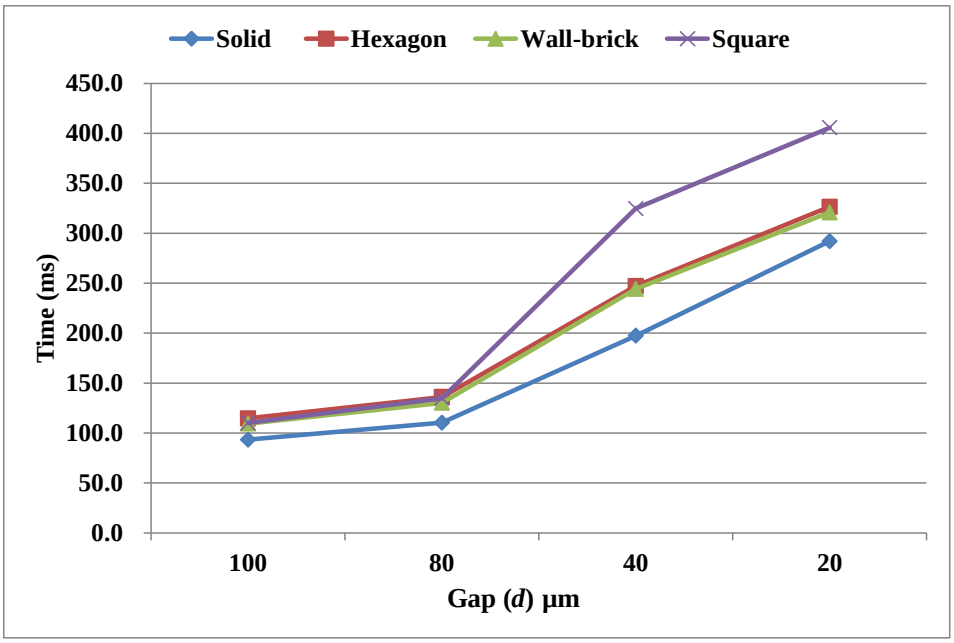

Figure 3.17. Summarized results from droplet motion simulations.

actuated by the solid electrode and the three CMAs. The total traveling times are: 140.9 ms for the solid electrode, 179.6 ms for the hexagon CMA, 167.2 ms for the wall-brick CMA, and 166.1 ms for the square CMA. Figure 3.16(b) shows the speed distributions of the square droplet actuated by the solid electrode and the three CMAs. The total traveling times are: 93.3 ms (solid), 115.6 ms (hexagon), 109.4 ms (wall-brick) and 110.1 ms (square).

One of the key considerations for the MEDA architecture is dynamic aspect ratios caused by different sizes of droplets on the same chip with a fixed gap height, possibly resulting in unwanted small aspect ratios. When the aspect ratio gets smaller, the total opposing force is expected to get bigger [144]. To understand the impact from the small aspect ratios, four aspect ratios (0.1, 0.08, 0.04 and 0.02) were simulated. Summarized results from droplet motion simulations under the four aspect ratios are shown in Figure 3.17. This summary represented the simulated EWOD actuation behaviors, which were intended for comparison with the actual experimental results. Empirical data showed that EWOD-actuated droplets were more square

than circular, so the *d/L* impact summary was prepared by square-droplet simulations. With a fixed spacing/length ratio (*s/L* = 0.1), simulations of different aspect ratios *d/L* revealed unexpected performance degradations of the square CMA. When $d/L \geq 0.08$, all three CMAs were performing similarly. However, at *d/L* = 0.04, the droplet motion performance of the square CMA dropped significantly (60.8%-of-solid) in comparison to others (around 80%-of-solid). When the aspect ratio further decreased to *d/L* = 0.02, all CMAs, including the solid electrode, dropped in performance but the square CMA still dropped more significantly than the rest of the CMAs. The hypothesis of this phenomenon was that when the opposing force was more significant, the bigger fluctuation of the force distribution the more degradation on the overall motion performance (Figure 3.12).

3.8.7 Modeling Results for the Microelectrode Dot Array Architecture

1. The main purpose of this modeling was to understand the significance of the shape and spacing of microelectrodes in droplet actuations of the MEDA architecture. The focus was on the study of the EWOD actuation force on the droplet in transition. The energy-based model and the contact-line-effective-length-based model were implemented both analytically and numerically with a square droplet. Both models worked out well with the MEDA architecture and revealed the same EWOD-actuated force distributions of the droplet. Due to the higher complexity, only numerical simulations were performed for circular droplets.
2. Based on the actuation force simulations, the actuation force distributions of the three CMAs showed the same general distribution trends as the distribution curve of the solid electrode, but complicated by the spacing between microelectrodes (Figure 3.12 and Figure 3.14).
3. The EWOD actuation force has a dependence on $(s/L)^{-1}$. The smaller the *s/L* the better the actuation performance of the MEDA architecture. With *s/L* = 0.027, the actuation forces of the three CMAs exceeded 93% of the actuation force of the solid electrode (Figure 3.15).

4. The upper bound of the actuation force distribution for CMAs can be approximated by (1 − *s/L*)%-of-solid (Figure 3.12 and Figure 3.14). For example, when *s/L* = 0.027, the upper bound of the actuation force distribution is about 97.3%-of-solid.
5. If a big spacing/length ratio situation (e.g. *s/L* = 0.4) cannot be avoided in the design of the microelectrode array, hexagon microelectrodes should be avoided based on the results shown in Figure 3.15.
6. The purpose of droplet motion modeling was not aimed at developing a better droplet motion prediction model for conventional electrodes. Instead, the goal was to develop a simplified model which was capable of presenting the simulated droplet actuation forces into a more assessable format, such as the droplet velocity. Therefore, this droplet motion modeling was mainly based upon the foundation of droplet actuation force simulations, and the effects from opposing forces were simplified.
7. Shapes of droplets did have impacts on the EWOD actuation performances specifically for the hexagon CMA. Based on the simplified droplet motion model, the hexagon CMA showed more dependence on the shapes of droplets. While both the wall-brick CMA and the square CMA showed 1% change between the circular droplet (84%-of-solid) and the square droplet (85%-of-solid), the hexagon CMA changed from 78%-of-solid for the circular droplet to 81%-of-solid for the square droplet.
8. Overall, for $d/L \geq 0.08$ and $s/L = 0.1$, the droplet motion performances, based on the square-droplet simulations, of all three CMAs were more than 80%-of-solid and had less than 5% deviations from each other (Figure 3.17).
9. However, at $d/L \leq 0.04$, the droplet motion performance of the square CMA dropped significantly in comparison to others (Figure 3.17).

CHAPTER 4. PROOF-OF-CONCEPT EXPERIMENTS OF THE MICROELECTRODE DOT ARRAY ARCHITECTURE

This chapter starts from the design and fabrication of proof-of-concept prototypes. The second section covers the test setup. Proof-of-concept experiments of the MEDA architecture are arranged into four sections: (a) Section 4.3 covers the configuration and group activating test; (b) Section 4.4 is for basic microfluidic operations; (c) Section 4.5 covers advanced microfluidic operations; (d) Section 4.6 discusses droplet motion performance experiments. The overall test results are then summarized in the last section.

4.1 Design and Fabrication of Proof-of-Concept Prototypes

To prove the concept of the MEDA architecture, ITO-glass prototypes were fabricated to conduct extensive experiments for the architecture. Different levels of EWOD microfluidic operations were performed to verify the microfluidic functionality of the MEDA architecture. Except motion-comparison prototypes, which had all three CMAs, the rest of prototypes were fabricated on ITO glasses based on the square CMA configuration (Figure 3.8(a)) to simulate the worst case scenario predicated by the numerical simulations. Both individually controllable microelectrode arrays and hardwired CMAs were fabricated for the experiments. Individually controllable microelectrode arrays were limited by the small number of microelectrodes so that they were designed only for CMA configuration and group activating experiments. A 4 × 12 individually controllable microelectrode array is shown in Figure 4.1(a). For more complicated microfluidic operations, hardwired CMAs, which were formed by grouping microelectrodes together with thin hardwires, were designed and fabricated for the experiments. The example illustrated in Figure 4.1(b) is the design of hardwired CMAs for diagonal droplet transport. Each microelectrode was 100 μm × 100 μm with a 10-μm spacing between the microelectrodes. The hardwire trace was 10 μm wide.

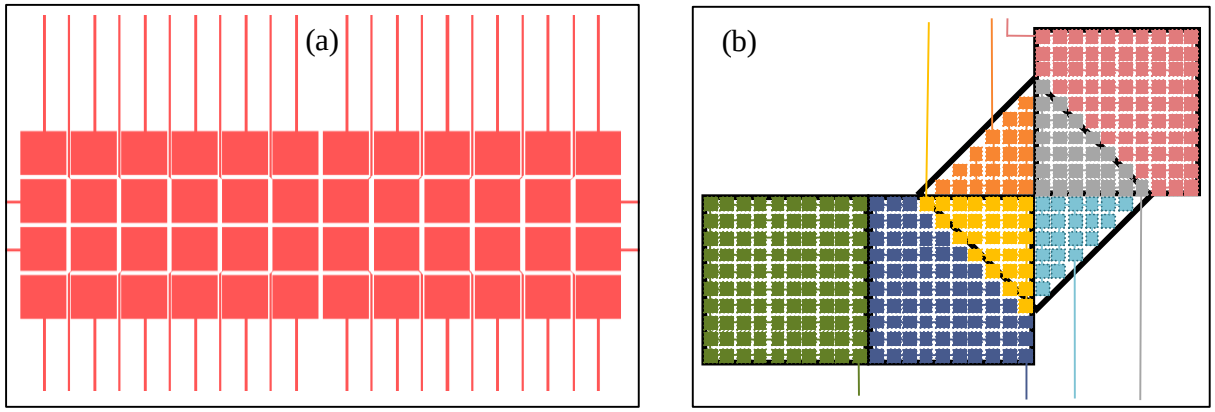

Figure 4.1**.** The design and fabrication of ITO-glass prototypes: (a) the design of the 4 × 12 individually controllable microelectrode array; (b) the design of the ITO-glass prototype for performing diagonal droplet transport and cutting.

On top of the ITO electrodes, a 1-µm-thick dielectric layer (SU8-2002) was spin-coated by: (1) 5 seconds at 1,000 RPM, (2) 60 seconds at 4,500 RPM, (3) 90ºC soft bake for 1 second, (4) near UV (wavelength = 350 - 400 nm) exposure (~36 mW/cm^2) for 2.5 seconds, and (5) 150ºC bake for 5 minutes. A 55-nm hydrophobic layer was then spin coated (1 wt% Teflon AF1600, 30 seconds at 3,000 RPM, and 150ºC bake for 30 minutes) on top of the dielectric layer. There was a total of 15 groups, T0 to T14 as listed in Appendix B, of ITO-glass prototypes designed and fabricated for the experiments.

4.2 Test Setup

Figure 4.2 shows the block diagram of the test setup for proof-of-concept experiments of the MEDA architecture. Droplet actuation high voltages were generated by an Agilent 332200A 20 MHz Function/Arbitrary Waveform Generator and an A.A. LAB System A-303 High Voltage Amplifier and Modulator. The actuation voltages were delivered to ITO-glass prototypes through a mechanical relay board, which was controlled by a National Instruments (NI) USB-6251 data acquisition (DAQ) device. LabVIEW 8.6 programs (Component Configuration Window and Microfluidic Operation Control Window) converted microfluidic operations into physical control

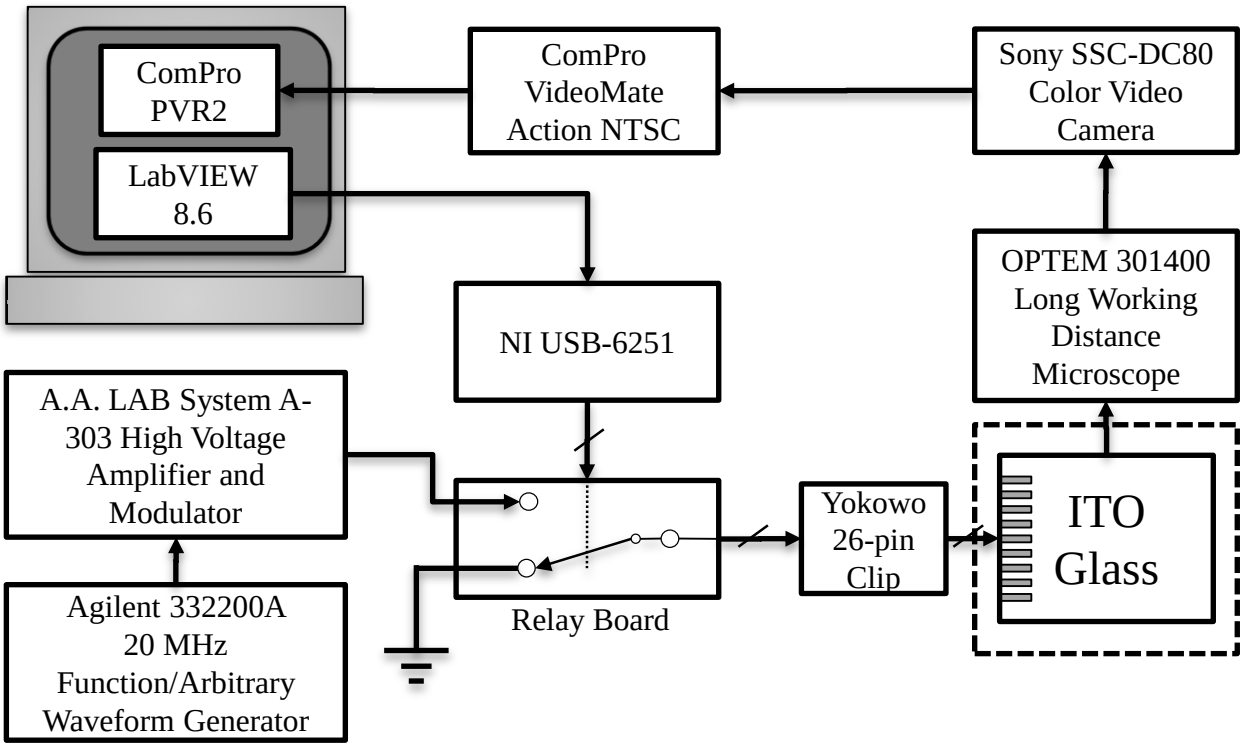

Figure 4.2. Block diagram of the experiment test system for ITO-glass prototypes.

sequences of the DAQ device. Actual microfluidic operations were observed visually by a long working distance microscope (Optem 301400) and a CCD color camera (Sony SSC-DC80 Color Video Camera). Videos were collected by a PC using ComPro VideoMate and ComPro PVR2 software.

4.3 Configuration and Group Activating Test

Both 2 × 12 and 4 × 12 individually controllable microelectrode arrays were fabricated for CMA configuration and group activating tests. For the convenience of discussion, a CMA composed of 4 × 4 microelectrodes is also called a 4×4-microelectrode CMA. Both 4×4-microelectrode CMAs and 2×2-microelectrode CMAs were configured for the CMA configuration test. Droplet transport and three-CMA droplet cutting were successfully performed by both sizes of CMAs. Figure 4.3 shows the picture of four 2×2-microelectrode CMAs

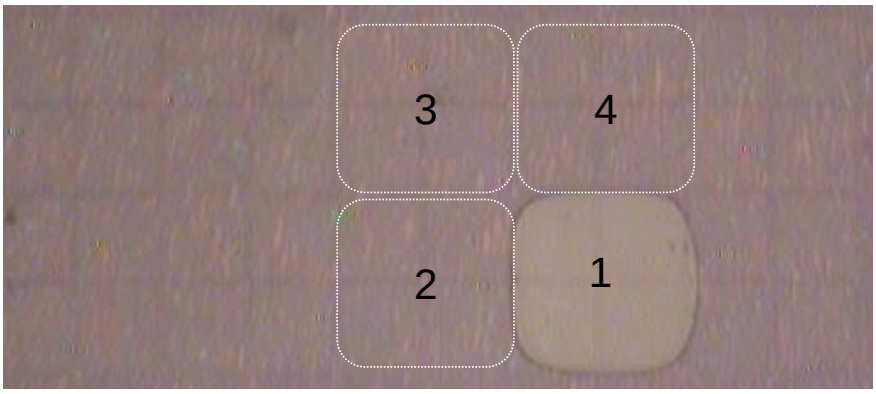

Figure 4.3. Four 2×2-microelectrode CMAs are performing a square loop (from position 1, 2, 3, 4 then back to 1) droplet actuation on the 4 × 12 microelectrode array.

performing a square loop (from position 1, 2, 3, 4 then back to 1) droplet actuation on the 4 × 12 microelectrode array. The main purpose of the test was to confirm the dynamic configurability and the group activation of the microelectrodes.

4.4 Basic Microfluidic Operations

The key hypothesis of the MEDA architecture was that microelectrodes can be dynamically configured into CMAs to have reliable microfluidic operations. Modeling and simulations were performed and discussed in the previous chapter to support this hypothesis. The experiment results from basic microfluidic operations directly confirmed the hypothesis.

4.4.1 Droplet Creating

Liquids from the input ports are stored in reservoirs. Droplet creating is the process of creating droplets from reservoirs. EWOD droplet creating was performed by activating droplet creating CMAs and the pull-back CMA in the reservoir. These activated CMAs extruded and pulled a droplet out from the reservoir. Figure 4.4(a) shows a liquid finger pulled by 10×10-microelectrode creating CMAs from the 24×26-microelectrode reservoir CMA, and Figure 4.4(b) shows the pinched droplet. Figure 4.4(c) shows smaller droplets created by 4×4-microelectrode creating CMAs.

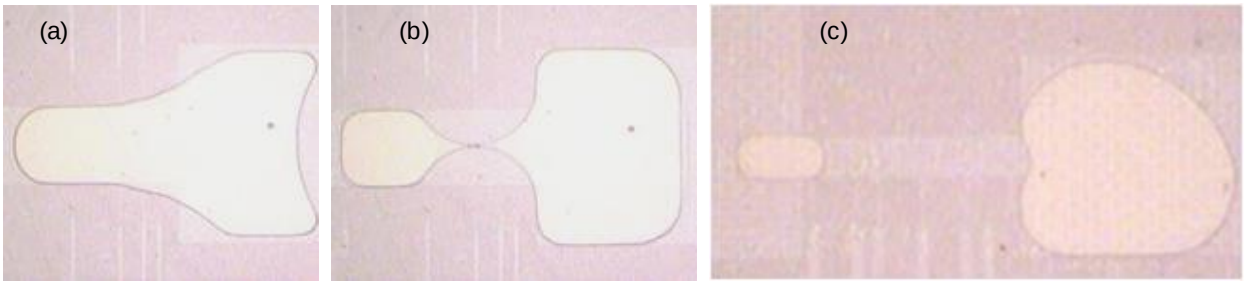

Figure 4.4. Droplet creating: (a) a liquid finger pulled from the reservoir (80 µm gap, 40 V); (b) the droplet pinched by deactivated CMAs; (c) Two smaller droplets were created by 4×4-microelectrode creating CMAs and added together (20 µm gap, 48 V). Both are bi-planar with DI water in air.

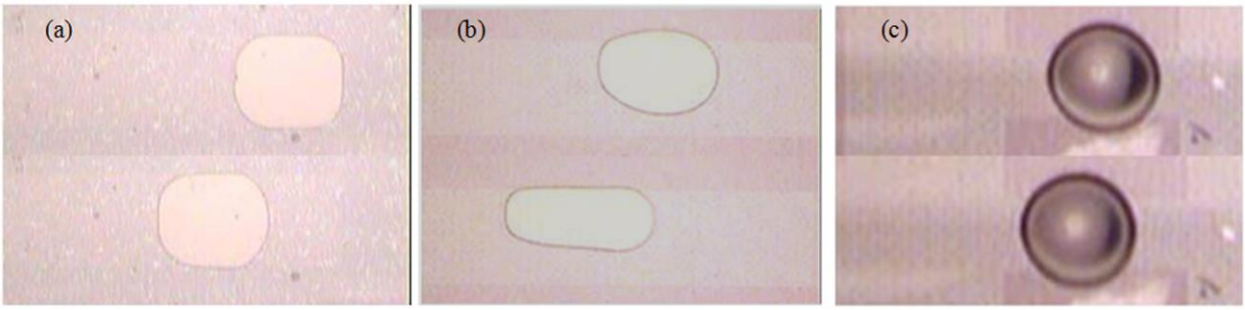

Figure 4.5. Droplet transport from the right (upper) to the left (lower): (a) bi-planar actuation with 80 µm gap; (b) covered coplanar actuation with the top plate and 80 µm gap; (c) open coplanar actuation without the top plate. All droplets are DI water in air.

4.4.2 Transport

Both bi-planar and coplanar (with and without the top plate) droplet transport actuations were successfully performed with the MEDA architecture. Figure 4.5(a) shows the picture of droplet transport by the bi-planar actuation. Different droplet sizes and plate gaps were successfully tested under the bi-planar actuation. More details of droplet transport performances are given later in Section 4.6. Figure 4.5(b) shows the covered coplanar droplet actuation, which has both droplet actuation CMAs and ground CMAs on the bottom plate. For the coplanar droplet actuation, a typical 10×10-microelectrode CMA was divided into a 5×10-microelectrode actuation CMA and a 5×10-microelectrode ground CMA. Actuation CMAs and ground CMAs were arranged in a way as indicated in Figure 2.11(d) for the coplanar droplet actuation. Figure

4.5(c) depicts the open coplanar droplet actuation. It can be seen that the sessile droplet is more circular from top view of the open configuration.

4.4.3 Cutting

Three CMAs were used to perform droplet cutting. During droplet cutting, the middle CMA was deactivated and the outer two electrodes were activated. Consequently, the droplet was stretched by EWOD actuation forces of the two activated CMAs, and it was pinched off into two daughter droplets by hydrophobic forces from the middle electrode. Figure 4.6(a) illustrates a typical three-CMA droplet cutting operation performed by three 10×10-microelectrode CMAs. Figure 4.6(b) shows a picture of three-CMA droplet cutting performed by ITO-glass prototypes.

4.4.4 Mixing

The mixing operation was performed by creating two droplets from two reservoir CMAs, transporting two droplets across the CMA array, and merging two droplets together at the mixing CMA. In DMFBs, droplets act as virtual chambers for mixing, incubation and reaction. Effective mixing of analytes and reagents is difficult to achieve in DMFBs due to the small Reynolds numbers of droplets. Reynolds number is defined as the ratio of inertial forces to viscous forces; $Re = \rho v R/\mu$ where ρ is the fluid density and μ is the dynamic viscosity of the fluid. Hence, a low Reynolds number implies laminar flow. With typical DMFB velocities of the order of $v \approx 10^{-3}$ m/s and droplet sizes of $R \approx 10^{-3}$ m or less, Re ≈ 10 for water. The ability to mix liquids quickly while utilizing a minimum area greatly improves the performance of the microsystem. Figure 4.6(c) shows the picture of diffusion-only droplet mixing by simply merging two droplets together. The mixing time by diffusion was long due to the small mixing interface between two liquids and the long diffusion length (~CMA length). Diffusion mixing was ineffective for DMFBs especially for those with small aspect ratios (gap/length).

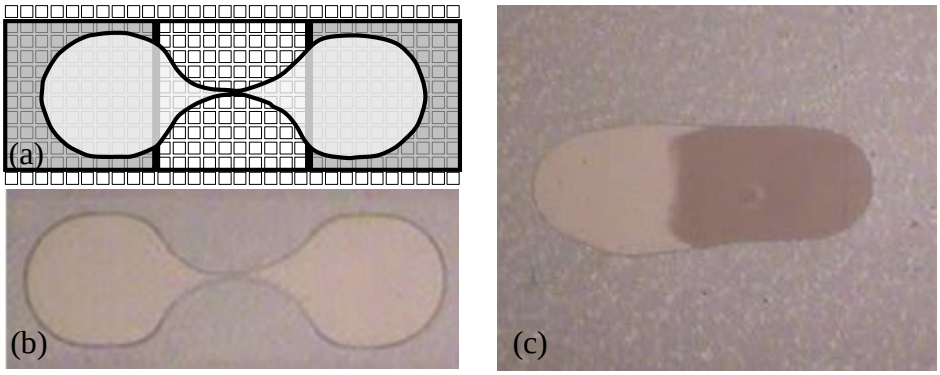

Figure 4.6. Cutting and mixing: (a) the illustration of typical three-CMA cutting; (b) a picture of three-CMA droplet cutting (bi-planar, 100 μm gap, 62 V, DI water in air); (c) a picture of droplet mixing.

4.5 Advanced Microfluidic Operations

CMAs can be dynamically configured, which increases the capability of manipulating droplets of the MEDA architecture. Some advanced microfluidic operations, which might not be easy for conventional EWOD microsystems to achieve, were performed and evaluated through the proof-of-concept experiments.

4.5.1 Droplet Aliquot

Traditionally, droplet volumes are decided by the droplet creating operation, which typically does not have the flexibility to control the size of the droplet. The dynamic configurability of the MEDA architecture could be used to create smaller droplets as unit droplets and then collecting the calculated number of unit droplets to form the desired droplet volume. Figure 4.7 illustrates this special droplet creating technique called “droplet aliquot”, where the creating CMAs were composed of 3 × 3 microelectrodes and the collecting CMA was composed of 10 × 10 microelectrodes. Droplet aliquot can be performed by the MEDA architecture easily and it provides a more precise control of the droplet volume. This technique can also be applied to perform more precise cutting or to measure the droplet volume. In both usages, it counts the number of smaller droplets created from the bigger droplet to cut or measure the droplet.

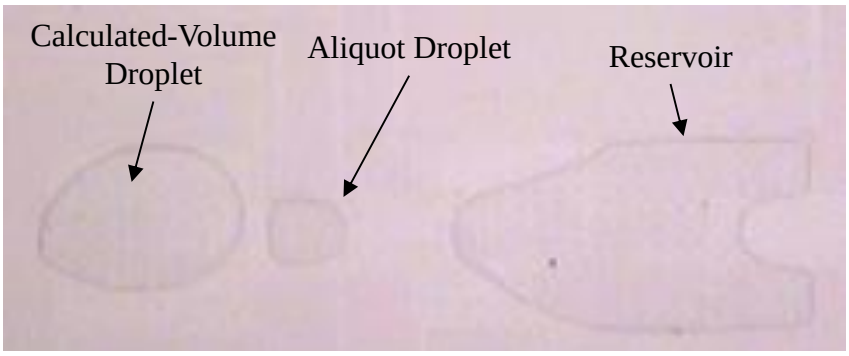

Figure 4.7. The droplet aliquot technique can be used to: control the droplet volume, do precise cutting, and measure the droplet volume (bi-planar, 20 μm gap, 50 V, DI water in 10 cSt silicone oil**)**.

4.5.2 Interim Bridging

Droplets reduce their sizes by evaporation or droplet cutting, and might become too small to be actuated reliably by electrodes. For example, the droplet (dotted circle) in Figure 4.8(a) cannot be actuated by the adjacent square CMA because the spacing prevents the physical overlap between the droplet and the CMA. The interim bridging technique was demonstrated to resolve the issue. An interim bridging CMA was dynamically created to overcome the physical gap. The interim CMA actuated the droplet toward the targeted CMA. Once the targeted CMA had a physical overlap with the droplet, then it was activated to pull the droplet in. The illustration and pictures for the interim bridging technique are shown in Figure 4.8.

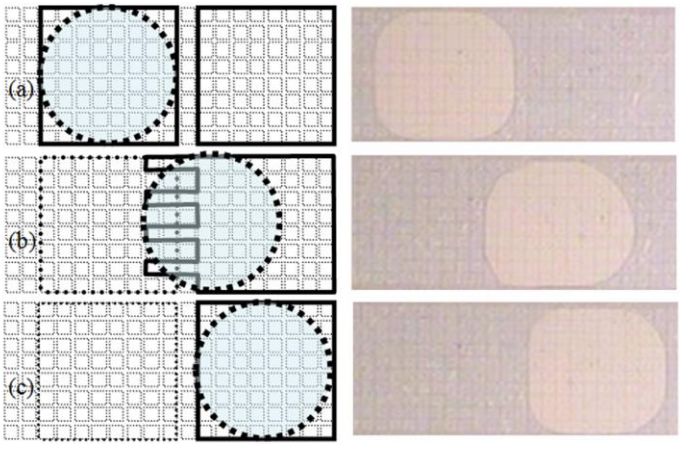

Figure 4.8. Interim bridging: (a) the droplet cannot be actuated by the adjacent square CMA because of the spacing; (b) the interim CMA is used to overcome the physical gap; (c) The targeted CMA pulls the droplet in.

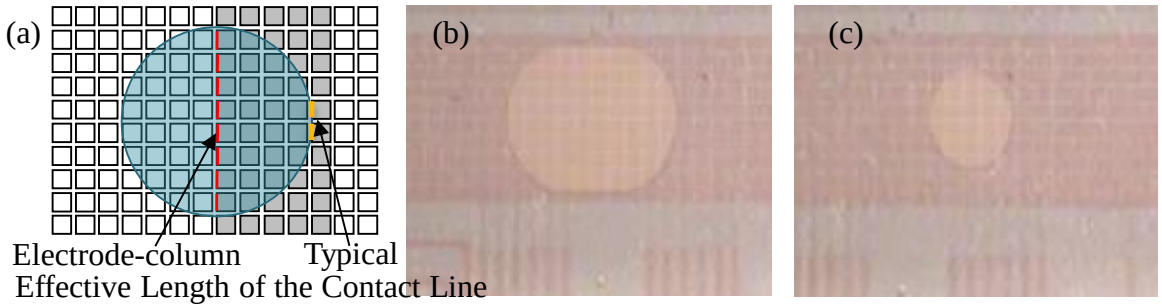

Figure 4.9. Electrode-column actuation: (a) the illustration of the 5-electrode-column actuation where its effective length of the contact line is longer than the typical actuation; (b) an 8×8-microelectrode droplet is actuated by the electrode-column actuation; (c) a stuck 4×4-microelectrdoe droplet is flushed out by the electrode-column actuation. Masks are added to the original pictures for better views of sizes of droplets for both (b) and (c).

4.5.3 Electrode-Column Actuation

The electrode-column actuation was demonstrated as an effective way to actuate the droplet. The traditional droplet actuation starts with a short effective length of the contact line because the overlap between the droplet and the electrode is limited. The better droplet actuation capability of the electrode-column actuation comes from the longer effective length of the contact line as shown in Figure 4.9 (a). In this special droplet actuation technique, electrode-column CMAs were configured as the base actuation component. Then, five 1×10-microelectrode electrode-column CMAs were dynamically grouped to form the actuation CMA. For actuating a droplet, only one electrode-column CMA was activated and deactivated at a time to keep the long effective length of the contact line. The experiments showed that the electrode-column actuation provided very effective and smooth actuation capability under marginal driving voltage situations. By calculation, this electrode-column actuation can roughly provide 1.9 times more actuation force to initiate the droplet movement than typical actuations. Details of the calculation are provided in Appendix B. The electrode-column actuation technique was also demonstrated as a useful tool to flush out stuck droplets. Figure 4.9(b) and (c) show electrode-

column actuations for an 8×8-microelectrode droplet and a smaller 4×4-microelectrode droplet that are too small to be actuated by a 10×10-microelectrode CMA.

4.5.4 Diagonal Transport

Diagonal transport is an advanced droplet transport operation that normally cannot be performed by the traditional EWOD microsystem. As indicated in Figure 4.10(a), there is no physical overlap between the diagonal electrode and the droplet such that the droplet cannot be actuated diagonally. To solve the issue, an interim CMA was configured and activated to move the droplet diagonally, and diagonal transport was smoothly performed. The dotted square area in Figure 4.10(a) shows the interim CMA. A smooth diagonal droplet transport operation is shown in Figure 4.10(b)-(d). Figure 4.10(c) shows the droplet actuation of the interim CMA. Practically, this diagonal transport technique can move the droplet in any direction. The flexibility of diagonal transport provides some advantages in droplet routing, which is discussed in Section 5.5.4.

4.5.5 Diagonal Cutting

Diagonal droplet cutting is an advanced droplet cutting operation as illustrated in Figure 4.11(a) and (b). Diagonal droplet cutting started from positioning the center of the droplet at the junction of two CMAs in the diagonal position by an interim CMA. Then activation of the two CMAs in the diagonal position would cut the droplet into two daughter droplets. Typically,

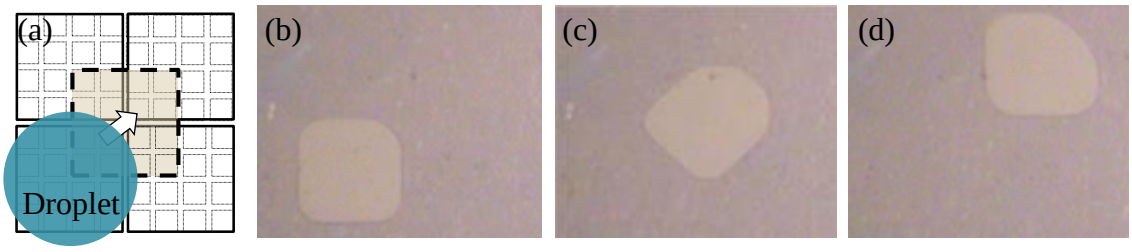

Figure 4.10. Diagonal droplet transport by the MEDA architecture.

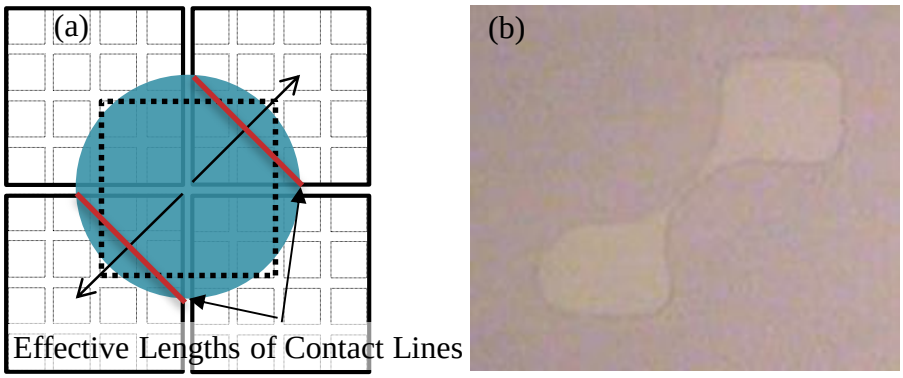

Figure 4.11. Diagonal cutting: (a) effective lengths of two contact lines during diagonal cutting; (b) the picture of diagonal cutting (bi-planar, 40 µm gap, 44 V, DI water in air).

diagonal droplet cutting is more effective than three-electrode droplet cutting due to longer effective lengths (about 50% longer, Appendix B) of contact lines as indicated in Figure 4.11(a). Also, diagonal cutting can be performed regardless of the size of the droplet to be cut. In contrast, traditional three-electrode droplet cutting has a minimum size requirement for the droplet, which needs to be big enough to have overlaps with both outer electrodes. Diagonal droplet cutting does not have this size constraint and can virtually cut droplets of any size.

4.5.6 Split-And-Recombine Lamination Mixing

There are two fundamental principles to improve mixing. The first one is to create a turbulent flow inside the micro-scale droplet. Alternatively, multilaminates can be created to achieve fast mixing via multilaminated diffusion. The dynamic configurability of the MEDA architecture provides a way to form multilaminates in the droplet by a sequence of diagonal cutting and mixing. The split-and-recombine (SAR) lamination mixer, which sped up mixing by creating multilaminates, was demonstrated by the MEDA architecture. The SAR lamination mixer is especially useful for the low aspect ratio ($d/L < 1$) situation. The low aspect ratio means that it is more difficult to create turbulent flow inside the droplet, and the ability to create multilaminates becomes more important.

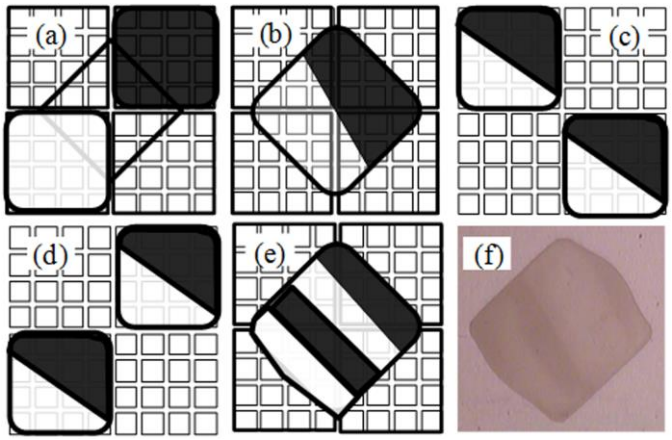

Figure 4.12. SAR lamination mixing based on the MEDA architecture: (a) initial positions of droplets; (b) step 1—diagonal mixing; (c) step 2—90 degree diagonal cutting; (d) step 3—droplets back to initial positions; (e) repeating step 1; (f) the picture from the experiment.

The demonstrated SAR lamination mixer has a small footprint (2 × 2 CMAs), as illustrated in Figure 4.12. Figure 4.12(a) shows starting positions of the black droplet and the white droplet. To start SAR lamination droplet mixing, the first step is to merge the two droplets diagonally as shown in Figure 4.12(b). The second step is to perform diagonal droplet cutting vertical to the mixing interface as indicated in Figure 4.12(c). Then, the third step of SAR lamination mixing is to move the two droplets back onto the starting CMAs in order to repeat diagonal mixing and cutting as illustrated in Figure 4.12(d). The procedure from step 1 to step 3 can be repeated to create the necessary numbers of multilaminates to speed up mixing. Figure 4.12(e) shows the four-laminated droplet as a result of repeating step 1 after the third step, and Figure 4.12(f) is the picture of a four-laminated droplet from the experiments. Typically, after three cycles of SAR lamination mixing, the droplets were well mixed.

4.5.7 Channel-Based Microfluidic Operations

By utilizing the flexibility of microelectrodes, there is a unique but very effective way of controlling microfluidic operations called “channel-based microfluidic operations”. As shown in

Figure 4.13, this technique is to build a channel between the targeted CMA and the reservoir CMA. In the experiments, the channel CMA was formed with a single line of microelectrodes between the 10×20-microelectrode reservoir CMA and the 10×10-microelectrode targeted CMA. While the reservoir CMA was deactivated, the activation of the channel CMA created a liquid flow on the channel CMA. The actuation of the targeted CMA continued the liquid flow onto the targeted CMA (Figure 4.13(a)). Once the targeted CMA was filled up, the liquid flow stopped (Figure 4.13(b)). Then the bridge CMA was deactivated, starting first from the microelectrode closest to the targeted CMA, to cut the linkage. After the deactivation of the channel CMA, the liquid in the channel CMA was pulled back to the reservoir CMA automatically.

Although this channel-based microfluidic operation looks simple, the demonstration actually covered all four fundamental microfluidic operations: creating, transport, mixing and cutting. As described above, the 10×10-microelectrode droplet was created from the 10×20-microelectrode reservoir CMA. So droplet creating was performed. This channel droplet creating could also be seen as droplet cutting of the 10×20-microelectrode droplet into two 10×10-microelectrode droplets. The channel CMA was formed to transport liquid from the reservoir CMA to the targeted CMA, so droplet transport was performed. In addition, another channel CMA could be

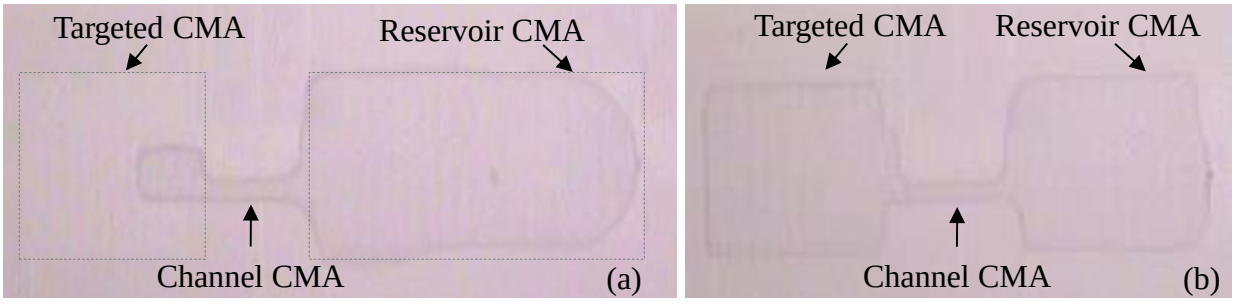

Figure 4.13. EWOD channel-based creating and cutting: (a) liquid is filling up the targeted CMA through the channel (Bi-planar, 20 μm gap, 50 V, DI water in 10 cSt silicone oil); (b) liquid flow stops when the targeted CMA is filled up.

formed to move the liquid from the second source onto the same targeted CMA to perform mixing.

A good application of this channel-based technique is to use channel-based transport for congested areas. For 10×10-microelectrode-sized droplets, a 10×10-microelectrode-sized area can only be used by one droplet to move through. This space can be easily configured into three 1×10-microelectrode channel CMAs to allow three independent liquid transport channels through the area. Allowing multiple independent liquid transport channels through a one-droplet area can increase the routability significantly for DMFBs.

4.6 Droplet Motion Performance Experiments

Droplet motion performance experiments, which measured the traveling times of droplets, were performed to address the key uncertainty—the spacing between the microelectrodes of the MEDA architecture. The results from the experiments were used to compare with the predictions from numerical simulations. Hexagon CMAs, Square CMAs, wall-brick CMAs and square solid electrodes were designed into ITO-glass prototypes for the droplet motion performance experiment. The design of the ITO-glass prototype for the droplet motion performance experiment is shown in Figure 4.14.

Test droplets were generated from the reservoir and moved to the desired CMAs to perform droplet motion experiments. Hexagon CMAs were designed in a way that both horizontal and vertical directions could be tested. Traveling times of a distance of 1090 μm (the CMA length) were measured under different gap heights (100 μm, 80 μm, 40 μm and 20 μm). The main actuation voltage was 50 V, but 48 V and 46 V were also checked to make sure droplets were not actuated marginally. All tests were performed by using DI water in air.

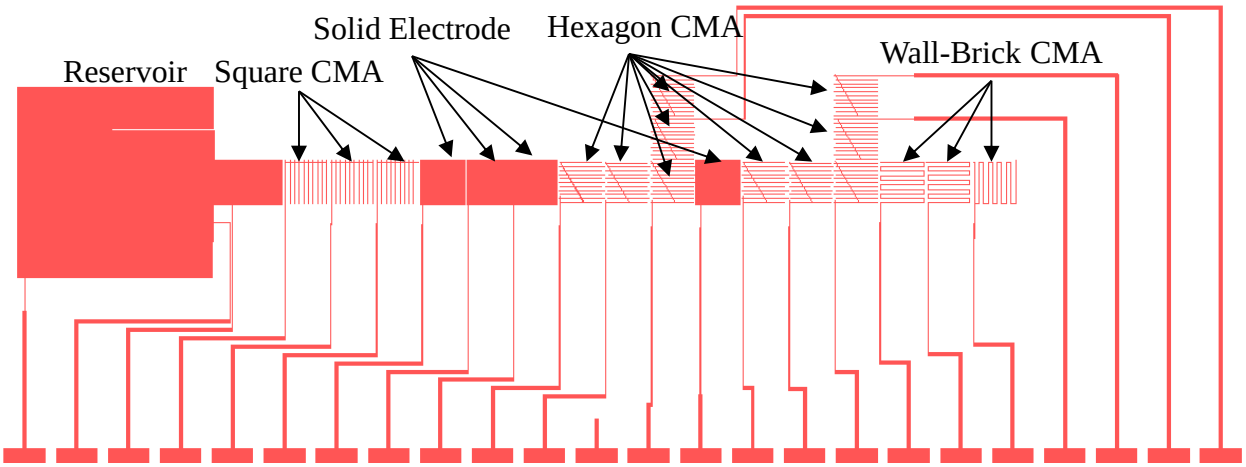

Figure 4.14. The design of the ITO-glass prototype for the droplet motion performance experiment includes: the reservoir CMA, solid electrodes, square CMAs, hexagon CMAs, and wall-brick CMAs.

The width of the spacing between microelectrodes represented the biggest variation, which was estimated to be about ±10%, because of the manual etching fabrication process of ITO-glass prototypes. Traveling time measurements of the experiments were averaged numbers from different batches of prototypes to minimize fabrication variations. Also, actuation force verifications between the vertical and horizontal directions of the hexagon CMA were checked first. The results showed less than 2% differences between two directions. Consequently, all subsequent experiments of the hexagon CMA were based on the horizontal direction for the convenience of performing the experiments.

The results from the droplet motion performance experiments agreed with the first scaling rule for DMFBs from the scaling model by Song et al. [142]. The scaling rule says that increasing d/L with all other system variables fixed increases the droplet velocity, while the dependence on d/L is weak. This scaling rule was specifically true for the solid electrode as shown in Figure 4.15(a). Measurement results of the three CMAs also agreed to the rule, but having other complications when $d/L \leq 0.037$.

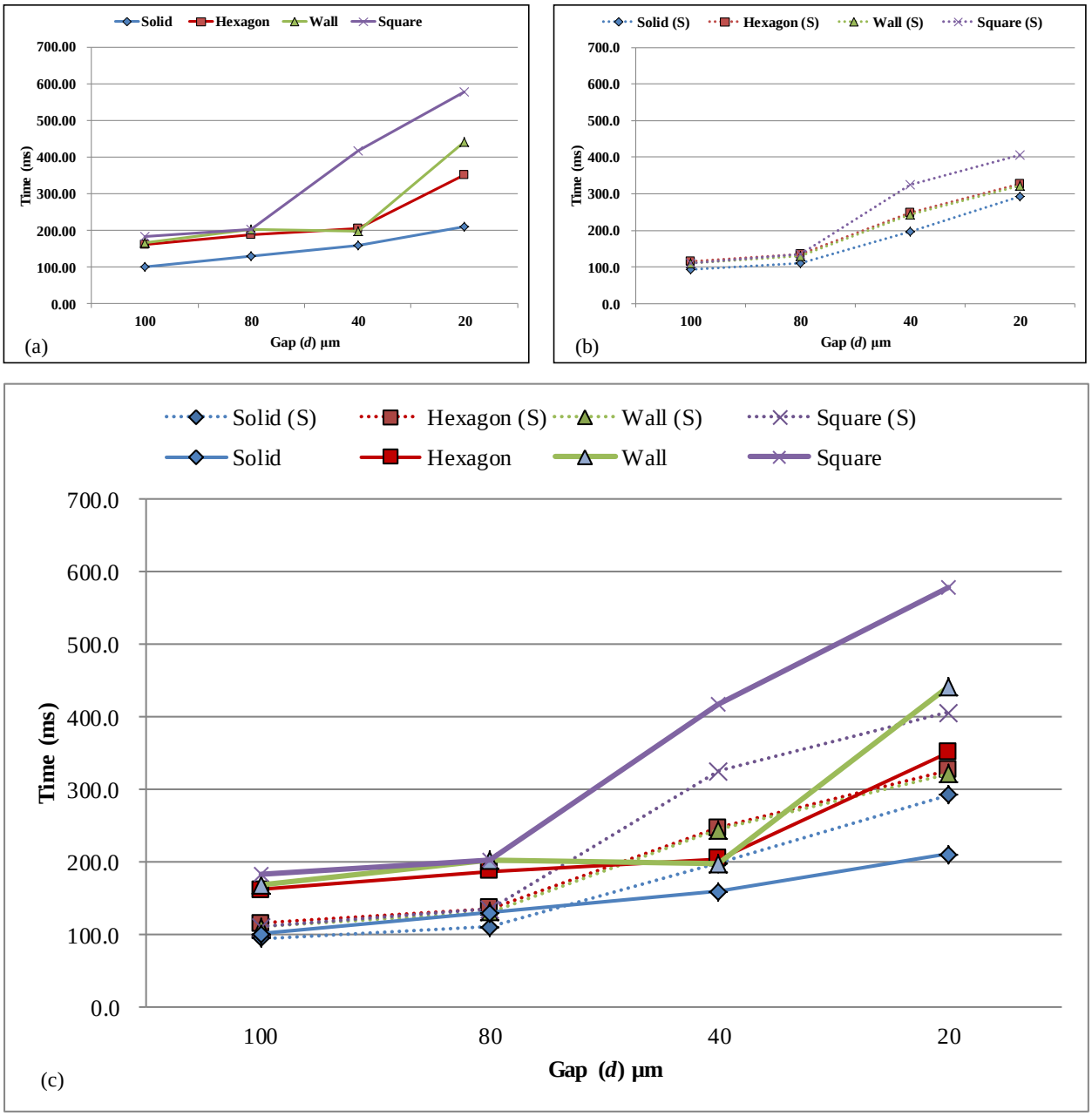

Figure 4.15. Comparisons of travelling times (ms) for a 1.09-mm distance of three CMAs and the solid electrode under different gap heights with a 50-V actuation voltage: (a) experiment results; (b) simulated predictions; (c) combined results.

Motion performance of droplets can be analyzed by their travelling times. Figure 4.15 shows the comparisons of travelling times between experimental results and simulation results. Referring to Figure 4.15(c), for d = 100 µm and d = 80 µm, the simulation results imply better

motion performances than the experimental results. Contact-angle hysteresis, which was not implemented in our simulations, might be accounted for the motion performance differences. For d = 40 μm, the simulations predicted the performance degradations for all CMAs and solid electrode, especially the noticeable performance drop of the square CMA. The experimental results did confirm the motion performance degradation of the square CMA. However, similar performance degradations were not observed in wall-brick and hexagon CMAs. Although the simulations did not reflect the exact amounts of the motion performance degradations, performance degradations were observed for all three CMAs at d = 20 μm. One key observation from the experiments was that the small aspect ratio (e.g. d/L = 20/1090 = 0.018) had more significant impact on the MEDA architecture (CMAs) than the conventional EWOD architecture (solid electrodes). The hypothesis from the simulations was that when the opposing force was more significant, the bigger fluctuation of the force distribution resulted in more degradation on the overall motion performance. As shown in Figure 3.12, solid electrodes did not experience fluctuation on the actuation force distribution and there was no implication of performance degradations at low aspect ratios from the experimental results. The three CMAs had different degrees of fluctuations on their actuation force distribution and their performance degradations at d = 20 μm coincided with the amplitudes of the fluctuations.

One thing unexpected from the experimental results was that the hexagon CMA had the best overall performance. This was especially true at d = 20 μm. Results from simulations predicted the wall-brick CMA should have a slight (less than 5%) performance advantage, but the experimental results showed that the hexagon CMA almost outperformed the wall-brick CMA in all places (Figure 4.15). The simulations indicated that the hexagon CMA was more sensitive to the shapes of droplets. Therefore, the dynamic contact angle and the shape of the droplet during

transition, which were not included in the simplified droplet motion model, might have played a role in the experiments. In addition, the spacing between hexagon microelectrodes was more often under-etched (estimated 10% variation) than the square microelectrodes through the manual fabrication. This meant that the spacing of the hexagon CMA could be a little bit smaller than the wall-brick CMA. This fabrication deviation might not have a significant impact, but it could contribute to the performance improvement of the hexagon CMA. Also, the performance advantage of the hexagon CMA was amplified at d = 20 μm. The hypothesis was still that when the opposing force was more significant, the bigger fluctuation of the force distribution resulted in more degradation on the overall motion performance (Figure 3.12).

4.7 Summary of Proof-of-Concept Experiments

1. The proof-of-concept experiments were fruitful. Different levels of EWOD microfluidic operations were performed successfully to prove the digital microfluidic functionality of the MEDA architecture. The architecture not only performed all basic microfluidic operations but also delivered some advanced microfluidic operations. Numerical simulations were performed and ITO-glass prototypes were fabricated to conduct droplet motion performance experiments to verify of the MEDA architecture. The results were also very successful.
2. The results from the droplet motion performance experiment agreed with the scaling rule that increasing d/L with all other system variables fixed increases the droplet velocity, while the dependence on d/L is weak.
3. One key observation from the experiments was that the small aspect ratio (e.g. d/L = 20/1090 = 0.018) had a bigger impact on the MEDA architecture (CMAs) than the conventional EWOD architecture (solid electrodes).
4. Among the three CMAs studied, the hexagon CMA had the best performance under low aspect ratio conditions. On the other hand, the square CMA was most susceptive to low d/L

conditions, and its performance started to degrade at d/L = 40/1090 = 0.037. Overall, the hexagon CMA had the best overall performance, and it would be the best choice for low aspect ratio ($d/L \leq 0.037$) conditions.

5. Through the experiments, design guidelines for the aspect ratio were carefully followed: (a) kept $d/L < 1$ for the oil filler medium; (b) kept $d/L < 0.4$ for the air filler medium; (c) all droplet sizes were factored into the calculations of aspect ratios so all met the design guidelines. By following these aspect ratio design guidelines, the experiments were performed smoothly in all microfluidic operations.
6. Two more design guidelines of aspect ratio came out from the experiments: (1) for a MEDA-architecture microsystem, it is highly recommended to have the aspect ratio bigger than 0.04 ($d/L \geq 0.04$); (2) if a small aspect ratio ($d/L \leq 0.04$) is required by the system, the microelectrode should be designed in the hexagon shape.

CHAPTER 5. DESIGN AND FABRICATION OF THE FIELD PROGRAMMABLE LAB-ON-A-CHIP

In this chapter, details of the design and fabrication of the FPLOC are discussed. The objectives of designing and fabricating the FPLOC prototype are (1) to demonstrate a DMFB based on the MEDA architecture, (2) to demonstrate the fabrication of a DMFB by the low-voltage CMOS technology, (3) to demonstrate droplet detection on-chip integration as well as large-scale microfluidics and microelectronics integration, and (4) to demonstrate the concept and the feasibility of the FPLOC. Before the FPLOC design and fabrication, the selection of the CMOS technology is discussed in the first section. The second section introduces the FPLOC. The hierarchical architecture and system partitions of the FPLOC are discussed in the third section. Designs of the functional blocks of the FPLOC are covered in Section 4, including the daisy-chained control structure, the bi-state-switch driver, the droplet detection circuit, the self-contained structure, the microelectrode shape and layout, the chip packaging and the built-in self-test. Section 5 is dedicated to the software design of the FPLOC. FPLOC hierarchical programming, top-down design automation, droplet routing and system software are covered in this software section.

5.1 CMOS Technology Selection

One of the research objectives is to fabricate the FPLOC with low-voltage CMOS technologies. A couple of high-voltage CMOS technologies (DALSA 0.8 μm high-voltage CMOS and TSMC T25HV 0.25 μm high-voltage CMOS) were evaluated to ensure that there were no dominant advantages of using high-voltage CMOS technologies. The evaluations not only did not reveal any dominant advantages of the high-voltage CMOS technologies, but also showed some drawbacks of utilizing high-voltage CMOS technologies. The main observations were: (1) high-voltage CMOS transistors were too big to construct microelectrodes smaller than

100 μm × 100 μm; (2) it was difficult to implement the droplet detection circuit with the high-voltage CMOS technology because high voltage components not only increase the size of the circuit but also complicate the design due to the need of high-low voltage interface circuits; (3) the fabrication time was longer and the cost was higher for the high-voltage CMOS; (4) some excellent CMOS-based capacitive detectors, mainly for video game controllers, have been implemented by low-voltage CMOS technologies such that a compatible microelectrode implementation would guarantee smoother integration in the future.

Eventually the decision was made to go with the TSMC 0.35 micron 3.3 V standard CMOS technology for the FPLOC fabrication, and the priority was set to explore the technology gap between the low-voltage CMOS technology and the FPLOC fabrication. In order to fully understand the technology gaps, the design and fabrication of the FPLOC were constrained to use strictly the standard 3.3 V CMOS technology and fabrication processes, including CAD tools, libraries, the die size and chip packaging.

5.2 Introduction of the Field-Programmable Lab-On-A-Chip

The idea of the FPLOC came from the field-programmable gate array (FPGA). The FPGA is an electrical programmable logic device that has the ability to configure the logic function by a designer after the fabrication process, therefore "field-programmable". From the function point of view, FPGAs work much like ASICs and can be programmed to implement all ASIC logical functions. The key difference is that ASICs are mask-programmed gate arrays and FPGAs are field-programmable gate arrays. ASICs require a very long (several months) development and fabrication time and they cannot be changed after the fabrication process. On the other hand, FPGAs require no masking steps and can be electrically programmed to implement logical functions after manufacturing. Normally, a hardware description language (HDL) is used to program product features and functions into the FPGA. FPGAs provide a design alternative for

designers to do fast prototyping of millions of gates of logic with low risks and low incremental cost. Therefore, FPGAs have become one of the key digital circuit implementation tools based on their flexible field-programmability, fast turnaround time and low non-recurring engineering costs [57, 58].

Similarly, the FPLOC is a pre-fabricated DMFB designed to be configured by customers or designers at their sites. Through software programming, the FPLOC can be configured to implement bio-medical applications that the conventional DMFB could perform. Based on the MEDA architecture, the FPLOC has a hierarchical programming structure that at the first level, descriptions of biomedical applications are translated into a set of microfluidic operations. The second level manages the microfluidic operations, including routing algorithms, types of microfluidic operations and timing sequences. The third level configures and manages microfluidic components to implement the microfluidic operations. At the bottom level, these microfluidic components are mapped into different groups of identical microelectrodes. The MEDA hierarchical architecture has advantages in implementing the top-down system-level design methodology because the identical microelectrode cells work as the foundation of building the entire DMFB hierarchically. This hierarchical programming structure of the FPLOC provides the convenience of constructing the DMFB system and controlling microfluidic operations through seamless software programming. Consequently, the FPLOC not only provides a solution to relieve designers from the burden of hardware design, slow turnaround time, high incremental cost and high development risk but also pioneers a path to provide biochip designers with CAD support at a level similar to that of the semiconductor industry. In the long run, the expectation is that the FPLOC would mimic the success of FPGAs. The FPLOC

may serve as an additional development tool for future DMFB developments, especially used in fast prototyping, education/training and quick-time-to-market product developing.

5.3 Architectural Design of the Field-Programmable Lab-On-A-Chip

5.3.1 Hierarchical Architecture

As indicated in Figure 5.1, the high-lighted blocks are the system layers implemented by the FPLOC based on the MEDA hierarchical architecture.

5.3.1.1 Biomedical Microfluidic Function Layer

At this layer, application-level functions and bioassays of the FPLOC are described and specified using a DMFB protocol. Next, a synthesis tool is used to generate detailed implementations of the FPLOC into a sequence of microfluidic operations. Limited by the maturity of the FPLOC and the resources (mainly the number of microelectrodes), the biomedical microfluidic function layer was not demonstrated in the first implementation of the FPLOC. The research focus was on the fundamental architecture and the enabling technologies such as the bi-state-switch driver. The demonstration of the biomedical microfluidic function layer would be included in future work.

5.3.1.2 Microfluidic Operation Layer

The microfluidic operation layer controls and manages sequences of microfluidic operations. It optimizes sequences of microfluidics operations based on FPLOC resource constraints and adds actuation timing aspects to these microfluidic operations. It then converts these microfluidic operations into corresponding microfluidic components and actuation timing sequences of these microfluidic components. The FPLOC microfluidic operation layer was demonstrated by NI LabVIEW software as the “Microfluidic Operation Control Window” which is detailed in Section 5.5.6. All microfluidic operations of this research were controlled by the “Microfluidic Operation Control Window”.

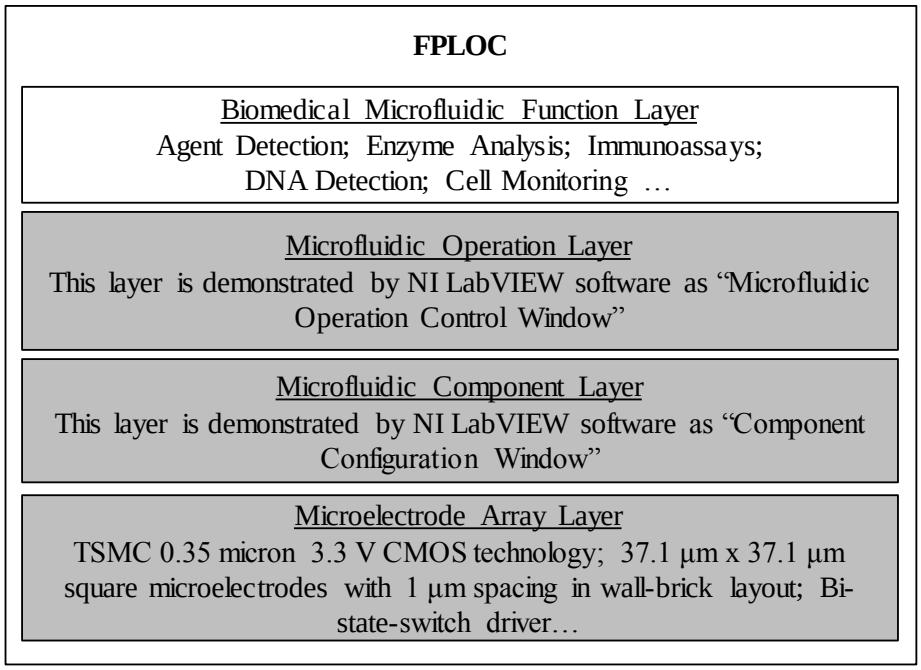

Figure 5.1. Top-level hierarchical architecture of the FPLOC. The high lighted blocks are the system layers implemented by the FPLOC based on the MEDA architecture.

5.3.1.3 Microfluidic Component Layer

At the microfluidic component layer, physical representations of microfluidic components required for microfluidic operations and the final layout of the biochip are generated at the geometrical level. One of the key tasks for this architectural layer is to map microfluidic components into groups of microelectrodes. Actuation timing sequences of microfluidic components are further converted into activating/deactivating timing sequences of each individual microelectrode. The FPLOC microfluidic component layer was implemented by NI LabVIEW software as the "Component Configuration Window" which is detailed in Section 5.5.5. The configurations of all microfluidic components and layouts of the FPLOC were achieved by the "Component Configuration Window".

5.3.1.4 Microelectrode Array Layer

The microelectrode array for the FPLOC was implemented by the TSMC 0.35 micron 3.3 V standard CMOS technology. The microelectrode cell was designed in the square shape (37.1 μm

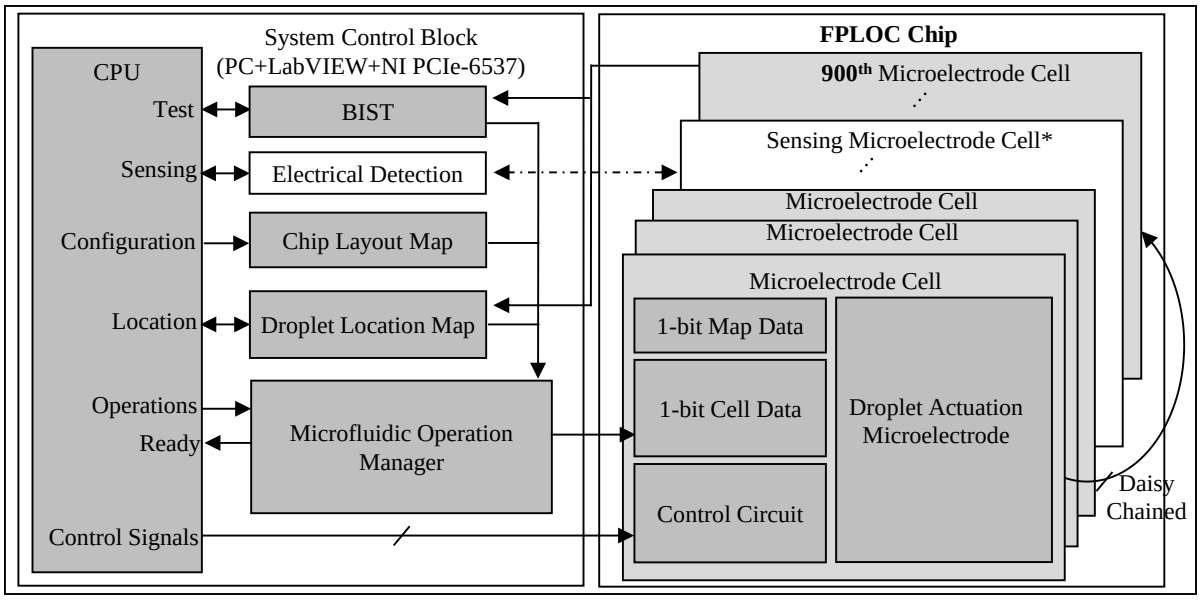

Figure 5.2. System partition of the FPLOC implementation. The high-lighted blocks are the functions implemented by the FPLOC.

× 37.1 μm), and the spacing between microelectrodes is 1 μm. A 30 × 30 wall-brick microelectrode array was implemented for the FPLOC. The bi-state-switch driver was designed to enable the fabrication of the FPLOC by the standard low-voltage CMOS technology.

5.3.2 System Partitions

As indicated in the system block diagram (Figure 5.2), the high-lighted blocks are the functions implemented by the FPLOC. The FPLOC chip includes 900 daisy-chained microelectrode cells and an interface circuit, which provides the connection to the system control block. All system control function blocks, except the BIST, were not integrated into the chip. The BIST leveraged the scan-chain structure of the microelectrode cell array so that it was built into the chip without extra circuits. The special Sensing Microelectrode Cell and the Electrical Detection, which work together to provide advanced electrical on-chip detection, were not implemented. Instead, the one-bit droplet detection was designed in each microelectrode cell to demonstrate the integrated detection capability. A PC and a NI PCIe-6537 interface card were

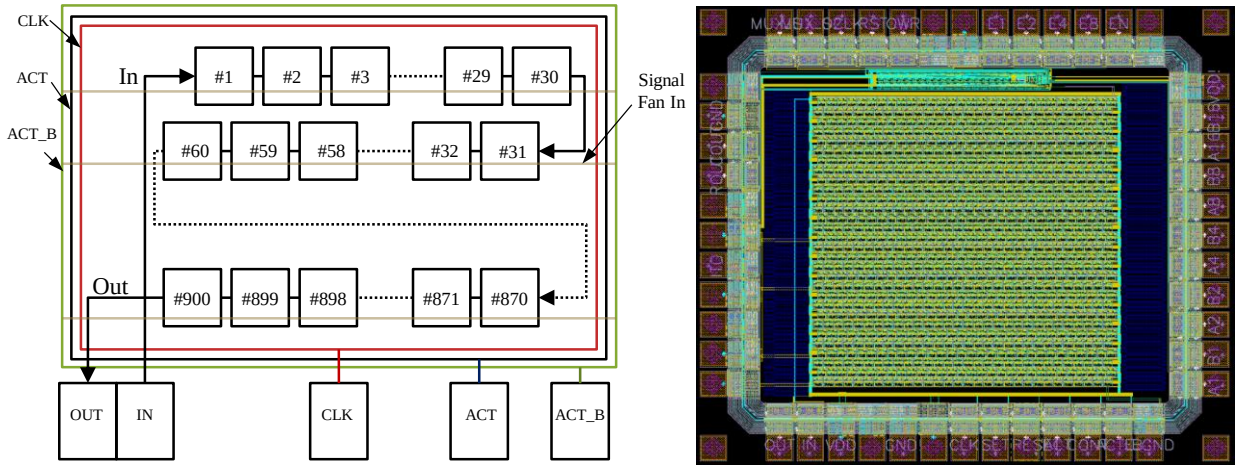

Figure 5.3. Daisy-chained microelectrode cells of the FPLOC: (a) the cell connection block diagram; (b) the layout design of the FPLOC, which reflects the connection block diagram.

used to form the hardware for the system control block. LabVIEW was used to implement other functions in the system control block. The BIST software was developed for the BIST function. The Chip Layout Map was implemented by the "Component Configuration Window". The Droplet Location Map was realized by Location Map software. Also, the "Microfluidic Operation Control Window" was generated to work as the Microfluidic Operation Manager.

5.4 Functional Blocks of the Field-Programmable Lab-On-A-Chip

5.4.1 Daisy-Chained Control Structure

The implementation of the daisy-chained control structure for the FPLOC is shown in Figure 5.3. The cell connection block diagram is shown in Figure 5.3(a). Each small block in the figure represents a microelectrode cell, and these 900 microelectrode cells are daisy-chained together. The upper-left corner is microelectrode cell #1, and the lower-left corner is microelectrode cell #900. Figure 5.3(b) shows the daisy-chained layout design of the microelectrode array, which reflects the connection block diagram.

5.4.2 Bi-State-Switch Driver

Conventionally, the EWOD microfluidic system requires high-voltage electrodes to perform the droplet actuation. Typically, the top plate is used as the electric potential reference (ground), and the high-voltage potentials are applied to electrodes on the bottom plate to perform EWOD actuations. The polarity of the droplet actuation voltage is not a concern in actuating droplets. By moving high-voltage potentials to the top plate and implementing the bi-state-switch drivers in the microelectrode on the bottom plate, the low-voltage CMOS fabrication technology can be used for EWOD actuations. Figure 5.4 illustrates the bi-state-switch driver. In this design, the high voltage is applied to the top plate, and the microelectrode is activated when it is grounded (0-state). The high-impedance mode (x-state) deactivates the microelectrode. In this arrangement, when the bottom microelectrode is activated (ground), the electric field still accumulates electric charges at the interface between the droplet and the insulating dielectric

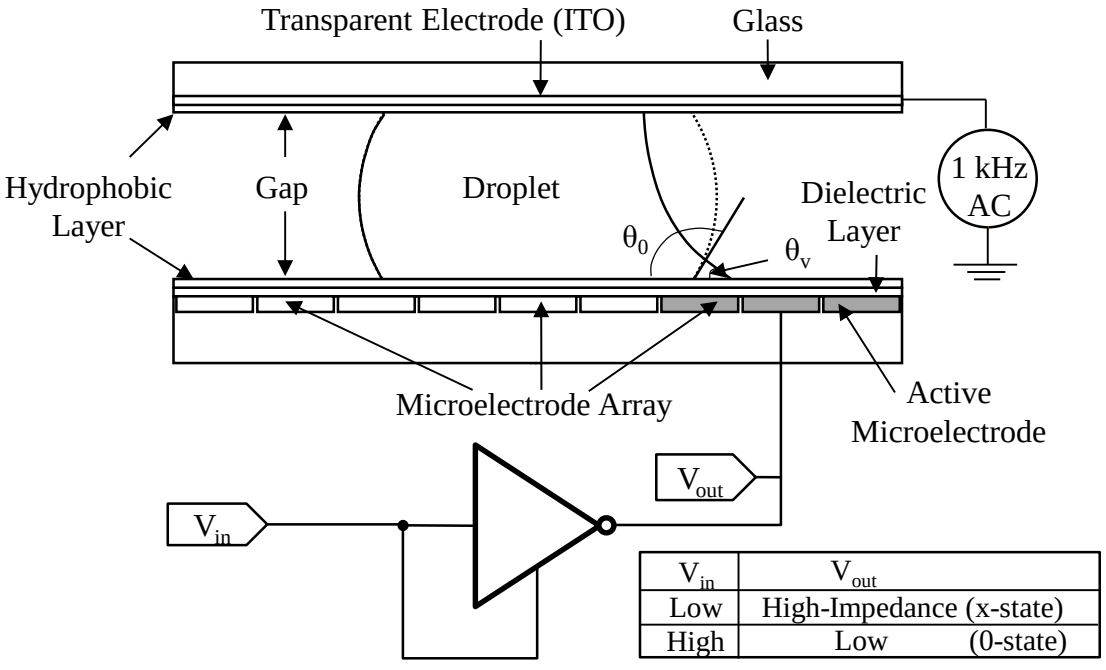

Figure 5.4. The bi-state-switch driver allows the EWOD droplet actuation by the low-voltage CMOS fabrication technology.

layer, causing the EWOD effect to transport the droplet. Although the polarity change of the actuation voltage might cause some degree of changes of the accumulation of electric charges at the droplet/insulator interface [145], the overall droplet actuations can be still reliably performed.

Prior to the fabrication of the FPLOC, mechanical relays and high speed CMOS logic tri-state buffers (74HC125) were used to test the concept. The mechanical relay represented the ideal situation, a perfect high-impedance mode, and the results proved the feasibility of the bi-state-switch driver. However, one area of concern came from the CMOS tri-state buffer—leakage currents of the high-impedance mode. Ideally, such as the mechanical relay, when the bi-state-switch driver is in the high-impedance state, the induced voltage on the microelectrode closely follows the applied voltage on the top plate such that the electric potential between the top plate and the deactivated microelectrode is zero. However, the high-impedance state of the CMOS tri-state buffer was not really an open circuit. Leakage currents occurred when the applied voltage on the top plate increased. Leakage currents then reduced the induced voltage. When the induced voltage was limited by leakage currents, the actuation force was also reduced. In addition, the CMOS tri-state buffer has the anti-static protection that prohibits the induced voltage to go beyond a certain level. Although leakage currents were anticipated for the bi-state-switch driver, the objective was trying to identify the technology gaps between the FPLOC and the low-voltage CMOS fabrication technology, so no fix was attempted in the fabrication of the FPLOC.

5.4.3 Droplet Detection

The strategy of on-chip detector integration, as well as the integration of microelectronics and microfluidics, was to have 900 simple one-bit detectors integrated into the FPLOC instead of a single but more complex capacitive detector. In this way, it not only could demonstrate integration of microelectronics and microfluidics in a larger scale but also could mitigate the risk from integrating the complex detector. A simple time constant capacitive comparator was

designed and integrated into the microelectrode cell. The design of the one-bit droplet detection is illustrated in Figure 5.5. The sensing control signal CONT switches the input of the D flip-flop (DFF) from the output of the last scan cell to V_{out}, which is its own physical microelectrode, to form the droplet detection loop (Figure 5.5(a)). As shown in Figure 5.5(b), the microelectrode is charged to 3.3 V first, and at t_0 it is discharged in order to measure the discharging speed. After a period of time from t_0, V_{out} is charged again to enable the measurement of the charging speed. The RC time constant of the microelectrode determines discharging/charging speeds. To detect the droplet, the CLK signal clocks the DFF as the logic latched comparator at the pre-calculated delay Δt from t_0. At the moment the CLK triggering edge comes in, if V_{out} is falling below $V_{ref,}$ then the logic value "zero" is latched onto the DFF, as indicated by the black discharging curve. In this case, the droplet detection senses a time constant less than Δt, so no droplet is present. When the droplet is present, as shown by the red-dashed discharge curve, the detector latches a "one" at the rising edge of the CLK. Both discharging and charging curves can be used to detect the droplet by adjusting Δt. After the droplet detection is performed, the CONT signal is disabled and the scan chain is restored to shift out the 900-bit droplet detection results.

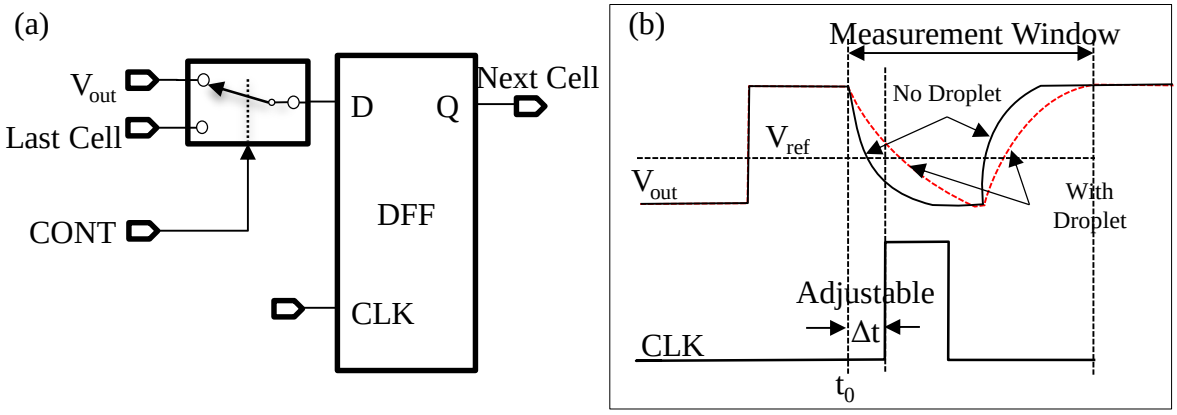

Figure 5.5. Diagrams of the one-bit droplet detection circuit: (a) the schematic of the time constant capacitive detector; (b) timing diagram.

In addition to the functional importance of the droplet detection, the implementation of the circuit was also a demonstration of integration of microfluidics and microelectronics. Because the droplet detection was included in the microelectrode cell, the microelectronic circuit became part of the microfluidic component. This represented true on-chip integration. In addition, a total of 900 CMOS-based capacitive detectors were built into the FPLOC, which resulted in larger scale integration than integration of a single but more complex detector. The success of integrating the droplet detection circuit means a high feasibility of more complex on-chip integration such as advanced detectors, CPU, memory, USB interface, wireless and others.

5.4.4 Self-Contained Structure

Another important design of the FPLOC was the self-contained microelectrode cell structure, where the control circuit, flip-flops, the droplet detection circuit and the bi-state-switch driver were contained in the area directly beneath the physical microelectrode. The first step for the standard-cell design approach for the microelectrode cell was to modularize the design, and this self-contained structure was an essential element in the modular design of the microelectrode cell. Input/output signals, structures of transistor devices, interconnect wiring layers, via layers, and physical dimensions of the microelectrode cell were carefully arranged in the layout of the microelectrode cell. Also, the metal 4 layer was used for the physical microelectrode, and the metal 3 layer was used as the shielding layer. Then, functional and analog SPICE validations were performed to finalize the microelectrode cell layout.

The layout view of the microelectrode cell is illustrated in Figure 5.6. The white dotted square is added to the layout figure to outline the shape of the microelectrode. It can be seen that all circuits are contained inside the white dotted square. All I/O signals of the microelectrode cell were arranged in the way that they could be conveniently connected with other cells to form the daisy-chained control structure. For example, the IN signal, which is the input of the shift

register, was arranged in the lower middle on the left-hand side, and the OUT signal, which is the output of the shift register, was arranged in the lower middle on the right-hand side. They were arranged in this way so that the left-to-right daisy-chained connection of microelectrodes could be easily achieved with minimum complexity.

After the design of the microelectrode cell, the layout of the microelectrode cell was duplicated to form the 30 × 30 microelectrode array of the FPLOC. It needs to be mentioned that the layout and simulations of the microelectrode cell were performed by the Si-Bio Chips Lab of National Chiao-Tung University (NCTU) in Taiwan based on the specs, schematics and design guidelines defined for the FPLOC.

5.4.5 Microelectrode Shape and Microelectrode Array Layout

Figure 5.7 shows the pictures of the FPLOC microelectrode array layout and the shape of the microelectrode cell. The 30 × 30 microelectrode array forms a working area of 1,142 μm × 1,142 μm for the FPLOC, as shown in Figure 5.7(a). Each microelectrode is 37.1 μm × 37.1 μm with 1

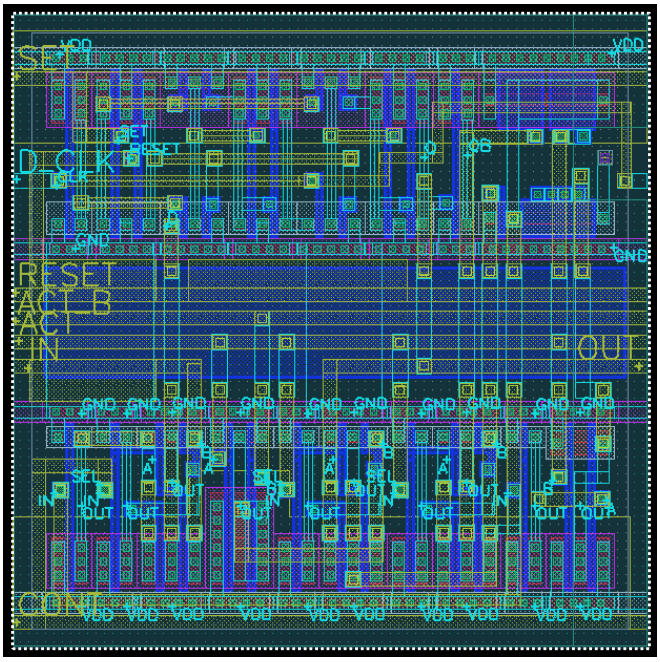

Figure 5.6. Top view of the FPLOC microelectrode cell layout. The white dotted square is added to outline the shape of the physical microelectrode.

μm spacing between the microelectrodes. The spacing/length ratio (s/L = 0.027) of the FPLOC is much better than the MEDA architecture design guideline ($s/L \leq 0.1$). Based on the simulations, this s/L ratio should have the actuation force greater than 93%-of-solid. The wall-brick microelectrode array was chosen for a balance between the design complexity and the actuation capability. Based on experimental data, the hexagon CMA had the best overall actuation capability, but the precise shape and the self-contained structure of the hexagon microelectrode were more difficult to implement. The wall-brick microelectrode array was chosen for its good actuation capability and its simple geometric form.

All thirteen pads were arranged on one side of the die in order to leave the other three sides open for accommodating the top plate without touching bonding wires. Four pads were used for droplet detection control, three pads were used for scan-chain control, and other pads were used for powers, grounds, SET and RESET.

5.4.6 Chip Packaging and the Cover Structure

The 48-pin ceramic dual in-line package (CerDIP) was chosen as the package of the FPLOC. The CerDIP is a rectangular ceramic package that has dual in-line leads on its longer sides. The

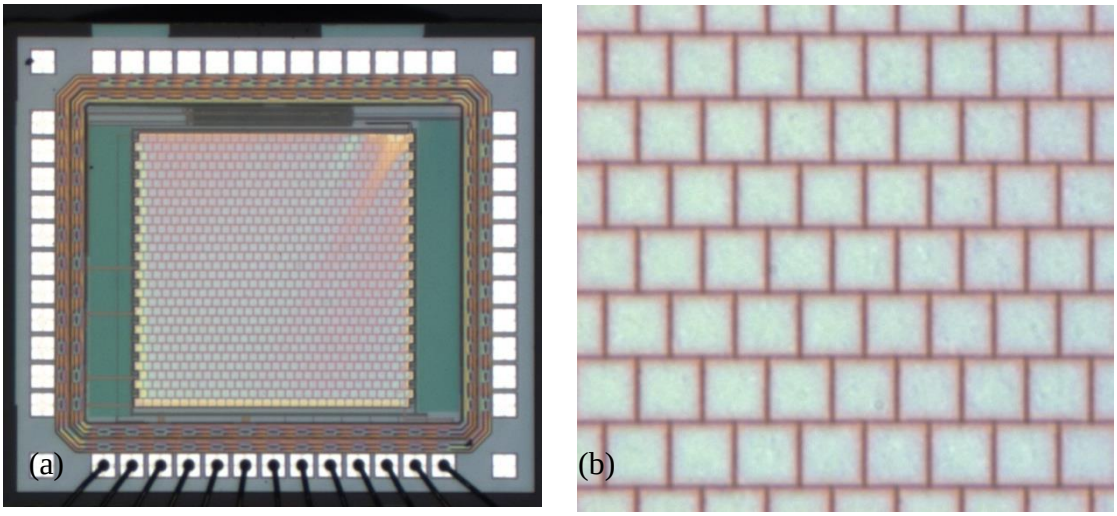

Figure 5.7. The layout of the FPLOC microelectrode array: (a) the die photo shows the microelectrode array and bonding wires, and (b) the wall-brick microelectrode array.

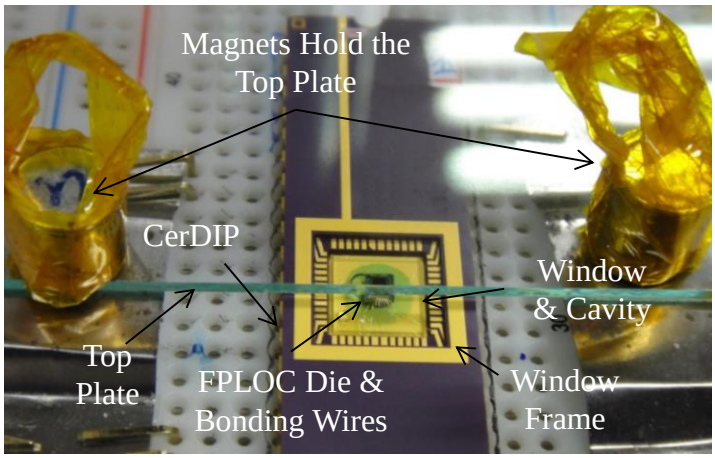

Figure 5.8. A photo of the FPLOC in 48-pin CerDIP and the top plate supporting structure.

package has a wide selection of available cavity sizes to accommodate the needs of different die sizes. The FPLOC was implemented as a covered DMFB that had a special top plate. The sealing glass of the 48-pin CerDIP was replaced by the special top plate, which also provided the bridging function for delivering the droplet onto the FPLOC. The die attachment was manually adjusted to have a 20-μm gap between the die surface (the bottom plate) and the cavity window frame. Therefore, the gap was 20 μm when the top plate was pressed against the cavity window frame. Other gap sizes were achieved by adding spacers and adjusting the top plate supporting structure.

Peak heights of bonding wires were about 200 μm above the die, and bonding wires would touch the top plate if the gap height is less than 200 μm. Therefore, all bonding wires were limited to one side of the die in order to free up the other three sides for the top plate. This cover arrangement not only prevented the space interference between the top plate and bonding wires but also avoided electrical shorts of the bonding wires by the droplet because the droplet was securely confined inside the bi-planar structure. Figure 5.8 shows a picture of the FPLOC in the 48-pin CerDIP package as well as the glass top plate and its supporting structure.

5.4.7 The Dielectric Layer and the Hydrophobic Layer

Since the design strategy of the FPLOC was to use the standard CMOS fabrication technology and process, the passivation layer of the chip was used as the dielectric layer. The passivation layer consists of a 1-μm Si_3N_4 layer and a 450-nm SiO_2 layer. A 55-nm hydrophobic layer was then deposited onto the dielectric layer by spin coating a 1-wt% solution of the Teflon AF1600 (Du Pont), which was dissolved in a fluorinated solvent (FC-77, 3M). An identical hydrophobic layer was also applied to the top plate. The combined capacitance of the dielectric and hydrophobic layers was calculated to be 31.93 pF/mm^2. The dielectric layer design had direct impact on the actuation capability of the FPLOC. Based on empirical data and more calculations, the minimum droplet actuation voltage for the FPLOC was expected to be around 18 V, assuming no impact from the leakage currents. Because the leakage currents were anticipated and the actuation capability appeared to be marginal, the electrode-column actuation technique (Section 4.5.3) was planned to help droplet actuations.

5.4.8 Built-In Self-Test

Two BISTs were designed for the FPLOC: the 900-BIST was designed to perform the test of the daisy-chained shift registers and the Metal-4 BIST was developed to test the metal-4 microelectrode and the droplet detection circuit. The 900-BIST is achieved by sending patterns through the 900-bit shift registers, and if the patterns come out correctly, then the daisy-chained shift registers are good. The Metal-4 BIST leverages the existing capacitance C_{34} between the metal-4 microelectrode and the metal-3 shielding layer. Without the cover or the droplet, this capacitance can be used to check the integrity of the physical metal-4 microelectrode and the droplet detection circuit. By adjusting Δt in Figure 5.5 against the RC_{34} time constant, the droplet detection results would show "1" for RC_{34} time constant greater than Δt, and "0" for

RC_{34} time constant less than Δt. Any broken connection or circuit between the bi-state-switch driver and the metal-4 microelectrode would result a "0" and fail the Metal-4 BIST.

5.5 Programming and System Software

In this section, the software design of the FPLOC is discussed. The FPLOC can be configured through seamless software programming into an application specific DMFB. The programming of the FPLOC is introduced in Section 5.5.1. Ultimately, the top-down design automation is the goal of the FPLOC and the MEDA architecture. The discussion of the top-down design automation is covered in Section 5.5.2. One key component of the top-down design automation for the FPLOC is droplet routing and it is introduced in Section 5.5.3. The advantages of the MEDA-architecture-based droplet router are discussed in Section 5.5.4. To demonstrate the field-programmability and the hierarchical software programming of the FPLOC, the Component Configuration Window and the Microfluidic Operation Control Window were implemented as system software tools. The last two subsections cover the designs of the Component Configuration Window and the Microfluidic Operation Control Window.

5.5.1 Programming of the Field-Programmable Lab-On-A-Chip

Before any programming or configuration, a blank FPLOC looks like what shown in Figure 5.9(a). It has an array of unrelated microelectrodes. There are several ways of programming the blank FPLOC. A conventional bottom-up programming is to work at the microelectrode level so that the control of the FPLOC ties directly to individual microelectrodes, and microfluidic operations are performed by direct activating and de-activating of individual microelectrodes. Designers of the FPLOC can choose this bottom-up approach to build the entire biochip and to perform microfluidic operations by using individual microelectrodes directly. However, to

simplify the programming process and to scale up the design of the FPLOC, a hierarchical programming of the FPLOC is highly desirable.

Hierarchical programming of the FPLOC can be done manually (bottom-up) and eventually automatically (top-down). For manual programming, the first design step (or the lowest-level work) for the FPLOC is to program the physical locations, sizes, and shapes of all microfluidic components, such as reservoirs, mixing areas, detection areas, transportation paths, and the overall layout of the FPLOC. Figure 5.9(b) illustrates an FPLOC being programmed into a DMFB application. This programmed-FPLOC has microfluidic components, including reservoir CMAs, droplet creating CMAs, the waste tank CMA, the mixing chamber CMA, the detection window CMA and transport path CMAs. The second step of designing the FPLOC is to define microfluidic operations for the chip. Microfluidic operations are controlled by selecting and activating CMAs at the right timing. To speed up the design of a complex system, libraries of predefined microfluidic functions can be used for the design process. Typically, the predefined microfluidic functions came from earlier experiments, and they have been tested and saved.

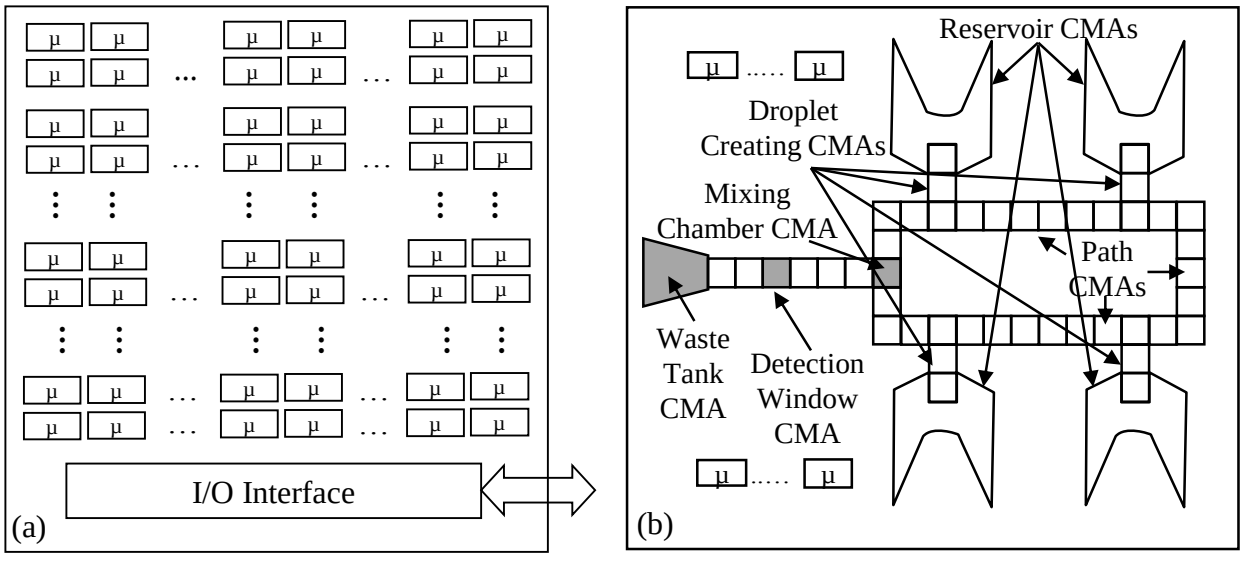

Figure 5.9. Programming of the FPLOC: (a) a blank FPLOC before any programming or configuration; (b) an example of a programmed FPLOC.

For example, the predefined microfluidic operations can be advanced microfluidic operations such as “Diagonal Cutting” or “SAR Lamination Mixing”. A batch file containing a sequence of predefined microfluidic operations can achieve rather complex FPLOC programming and microfluidic operations.

5.5.2 Top-down Design Automation

Hierarchical programming of the FPLOC can be done automatically in a top-down design approach. Based on the MEDA architecture, the top-down design automation starts from the biomedical microfluidic function layer. At this layer, application-level functions and bioassays of the FPLOC are scaled into a set of sequences of microfluidic operations. After the biomedical microfluidic functions being translated into specific sequences of microfluidic operations, the microfluidic operation layer optimizes sequences of microfluidics operations based on biochip resource constraints and adds actuation timing aspects to these microfluidic operations. It then converts these microfluidic operations into corresponding microfluidic components and actuation timing sequences of these microfluidic components. At the microfluidic component layer, physical representations of microfluidic components required for microfluidic operations and the final layout of the biochip are generated at the geometrical level. One of the key tasks for this architectural layer is to map microfluidic components into groups of microelectrodes at the bottom level. Actuation timing sequences of microfluidic components are further converted into activating/deactivating timing sequences of each individual microelectrode. The MEDA architecture has advantages in implementing this top-down design automation because the identical microelectrode cells work as the fundamental elements and hierarchically build the entire FPLOC.

Based on the top-down design methodology proposed by Su et al., the placement of wide varieties of microfluidic components has been identified as a key issue in the geometry-level

synthesis of DMFBs [18, 141, 146]. This issue can be managed better with identical microelectrodes as the basic building elements. Instead of managing a huge set of libraries for different microfluidic components and the complexity of physical constraints among different components, CMAs composed of identical microelectrodes provide a more manageable solution. In addition, on the resource sharing side, the dynamic configurability of microelectrodes can remove many resource constraints. For example, in the placement of microfluidic components, overlapped electrodes and interim electrodes are generally not allowed in the conventional DMFB architecture, but they are common practices for the FPLOC.

Also the physical verification of DMFBs is a difficult issue. Design rules for the accurate and efficient DMFB physical verification have been identified as one of the challenges in the development of the DMFB top-down design automation [141]. Physical verification is a process whereby a DMFB layout design is checked via EDA software tools to see if it meets design criteria. The challenge is mainly caused by the lack of standard microfluidic components. The standard cell methodology for the microelectrode is one of the best ways to resolve this issue. A well-characterized and fully-verified microelectrode cell makes accurate and efficient physical verifications for DMFBs more achievable.

As high design complexity and large-scale FPLOCs are anticipated to happen, top-down design automation of the FPLOC certainly requires the same level of CAD support as in the conventional ASIC design [147]. Droplet routing in the top-down design automation of the FPLOC is one of the most crucial design challenges because it is very complex and has direct impacts on the FPLOC performance. Notably, the routing process for the FPLOC is very different from conventional transport path electrode design approaches, and it is discussed in the next section.

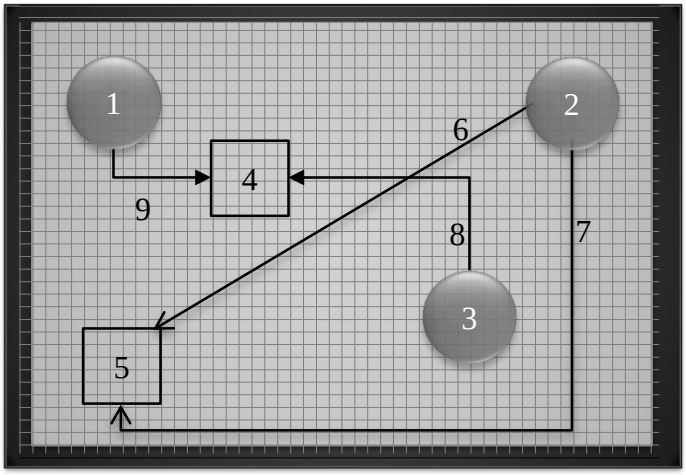

Figure 5.10. FPLOC droplet routing

5.5.3 Droplet Routing

Conventionally, the DMFB has transport path electrodes to transport droplets as shown in Figure 5.9(b). The FPLOC does not require fixed paths for transporting droplets. Instead, droplet routing is used to move multiple droplets simultaneously from multiple initial locations to designated destinations. FPLOC routing path selection needs to schedule droplet actuations under physical constraints such as contaminations, unreliable actuations, and timing restrictions. For example, droplets 1, 2 and 3 are at their beginning positions as shown in Figure 5.10. Droplet 1 and droplet 3 will be mixed at CMA 4, and droplet 2 will be transported to CMA 5. If contamination is not a concern, then droplet 2 can be moved by taking route 6, and droplet 3 can be moved by taking route 8. Precautions need to be taken so that droplet 2 and droplet 3 do not collide while moving to their destinations. If contamination is a concern, then droplet 2 might take route 7 to avoid any route overlaps. Also, droplet 1 and droplet 3 may have the time restriction to arrive at CMA 4 at the same time, so the distance difference between route 9 and route 8 needs to be taken into routing considerations.

5.5.4 Droplet Router Based on the Microelectrode Dot Array Architecture

Many droplet DMFB routing algorithms have been proposed [147, 148, 149, 150]. Compared to the conventional DMFB architecture, the MEDA architecture represents an ultra-high resolution situation that cannot be handled by existing droplet routing algorithms. This high resolution is caused and defined by the microelectrode. A new droplet routing algorithm was required for droplet routing of the MEDA architecture. Chen et al. presented a routing algorithm specifically designed for the MEDA architecture [151]. The new DMFB droplet router is capable of routing multiple variable-sized droplets concurrently and has advanced routing features specific to the MEDA architecture, such as diagonal and channel-based transport. The performance of the new router was evaluated against existing routing algorithms and it is discussed in the next two subsections.

5.5.4.1 Routing Algorithm Performance Evaluation Criteria

The evaluation of the overall performance of the new router was performed by several criteria: (1) the total number of used cells, (2) the average latest arrival time, and (3) the maximum latest arrival time. The total number of used cells indicates the degree of efficient usages of biochip resources. Both the average and maximum latest arrival times reflect the performance of the routing algorithm. The smaller number of these three measurements means the better performance. Because of the differences between solid electrodes (used by the traditional architecture) and CMAs (used by the MEDA architecture), appropriate conversions of the routing results were performed before the comparisons.

5.5.4.2 Routing Performance Analysis Results

A common set of predefined test cases were used to evaluate the performance of the MEDA-architecture-based router. The goal for the routing algorithm was to create path selections for droplets from their starting points to destinations by minimizing total used microelectrode cells

and the latest arrival times. Also, time and fluidic constraints defined by the test cases must be satisfied. Among reviewed routing algorithms, Huang's algorithm [148] had the best routing results, and Cho's algorithm [147] was the second best. Two configurations of the MEDA-architecture-based router were used for the comparisons: (1) diagonal transport without channel-based routing, and (2) diagonal transport with channel-based routing. The routing performance comparison was based on the same benchmark [151]. The numbers in Table 5-1 are normalized by the best numbers for easier comparisons. The routing simulation results showed that channel-based routing dramatically reduced (more than 60%) the total number of used cells. Diagonal transport was also proved to be a very effective approach in improving routing performances. The droplet routing algorithm can decide the system performance of the FPLOC. This MEDA-architecture-based routing algorithm works for both the conventional and the MEDA architecture with outstanding routing performances.

Table 5-1. Comparisons of MEDA-architecture-based routing results and existing works based on the conventional DMFB architecture [151]. The numbers in the table are normalized by the best numbers for easier comparisons.

	Max. Arrival Time	Avg. Arrival Time	Total #Cell Used
Cho's Algorithm [147]	1.29	1.32	4.15
Huang's Algorithm [148]	1.10	1.02	3.08
MEDA No Channel, 3 × 3 [151]	1.01	1.01	3.71
MEDA Channel, 3 × 3 [151]	1.00	1.00	1.00

5.5.5 Component Configuration Window

Based on the hierarchical structure of the FPLOC, National Instruments' Graphical programming language, LabVIEW, was leveraged to demonstrate the microfluidic component layer and the microfluidic operation layer. The graphical programming language approach simplifies the FPLOC programming process. The "Component Configuration Window" was designed as a graphical configuration tool for the microfluidic component layer.

At the microfluidic component layer, all necessary microfluidic components and the final chip layout of the FPLOC are defined. The final chip layout includes shapes, sizes and locations of all microfluidic components. The "Component Configuration Window" provided the geometry-level graphical interface to create physical representations of the microfluidic components and the final chip layout.

Figure 5.11(a) illustrates an example of using the Component Configuration Window to configure microfluidic components. The picture illustrates the physical configuration of #9 CMA. Each CMA configuration has a page (30 × 30) of blank microelectrodes (shown as dark green) to work on. The red circle in Figure 5.11(a) indicates that CMA #9 is under construction. Through the graphical interface, CMA configuration is a matter of pointing and selecting. CMA #9 is configured into a hexagon shape as an example. Additional software functions have been designed for the convenience of selecting larger areas or sequencing the same CMA configurations to later pages. While doing the configuration of the individual CMA, a real-time summary page shows all CMA configurations and the overall layout of the chip as depicted in Figure 5.11(b). In this summary figure, 10 CMAs, numbered from 0 to 9, form an electrode path from CMA #0 to CMA #9. CMA #4 shows a larger size for mixing of two droplets. CMA #0 and CMA #1 also demonstrate that overlapped CMAs are allowed in the FPLOC configuration.

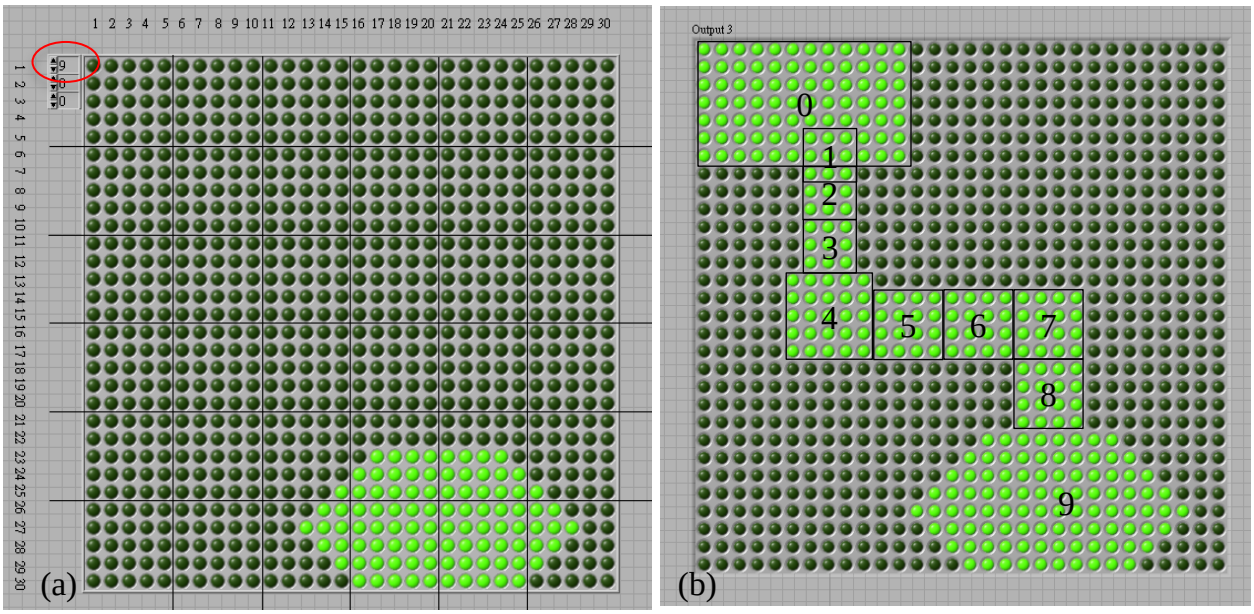

Figure 5.11. Demonstrations of the Microfluidic Component layer: (a) configuration of CMA #9 under the Component Configuration Window; (b) the real-time summary page shows all CMAs. Numbers and border lines in (b) are manually added for explanations.

5.5.6 Microfluidic Operation Control Window

The Microfluidic Operation Control Window was designed to demonstrate the microfluidic operation layer. The Microfluidic Operation Control Window can be used to handle the sequences and actuation timing steps for microfluidic operations. The graphical user interface of the Microfluidic Operation Control Window is shown in Figure 5.12(a). Actuation step numbers are on the y-axis, and CMA numbers are on the x-axis. There are other control buttons, windows and switches such as the step control button and the time interval window. Programming microfluidic operations through the control window is in two simple steps: (1) defining CMAs that would be activated in each actuation step, and (2) assigning the appropriate actuation time interval between the actuation steps. None, single or multiple CMAs can be selected at each actuation step. Defining the activated CMAs for each actuation step is a simple selecting and clicking process. The timing steps for actuations are driven by the time period needed to actuate

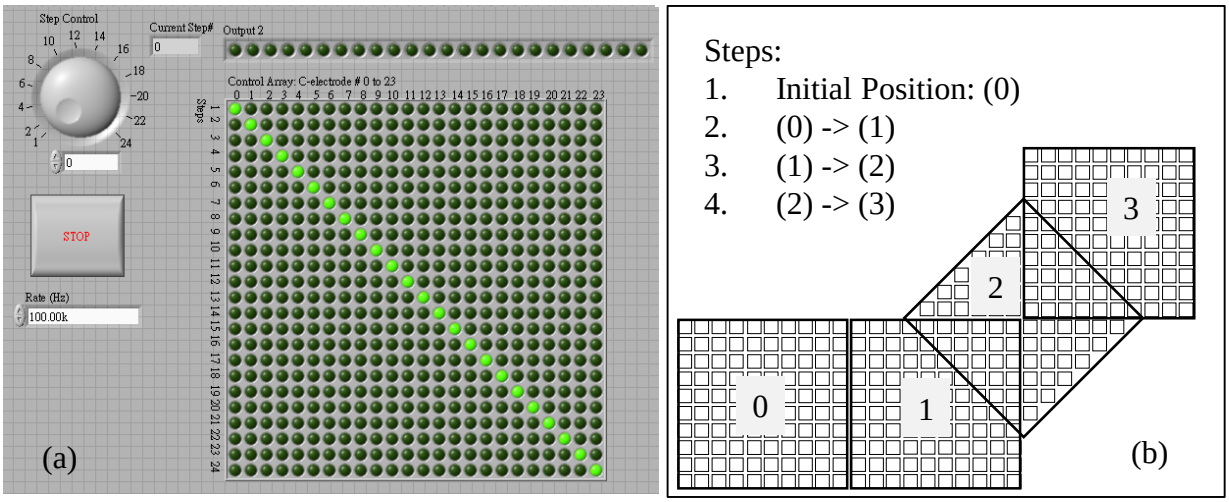

Figure 5.12. Demonstrations of the Microfluidic Operation layer: (a) the Microfluidic Operation Control Window; (b) a programming example of the diagonal droplet actuation.

the droplets to their next locations. Microfluidic operations are accomplished by sequencing through predefined actuation steps. Sequencing actuation steps can be operated in manual mode or auto mode. When in auto mode, the time delay between actuation steps needs to be specified. Because there is only one value of the time delay, the actuation step can be repeated if more actuation time needed. Some versions of the Microfluidic Operation Control Window also have limited looping capabilities.

Any actuation step change triggers a new droplet actuation cycle as defined in Figure 3.7. Besides, any change of the CMA selection inside the active actuation step also triggers a new actuation cycle of the FPLOC. So, in the active actuation step, manual selection/de-selection of different CMAs can be used to control microfluidic operations.

Figure 5.12(b) illustrates an example of performing a diagonal droplet actuation from CMA #0 to CMA #3 by using the actuation steps defined in Figure 5.12(a). Once CMAs shown in Figure 5.12(b) are successfully configured by using the Component Configuration Window, the diagonal droplet actuation could be performed by sequencing through 4 actuation steps. Step 1

activates CMA #0 to initiate the starting point of the droplet. Step 2 deactivates CMA #0 and activates CMA #1 to move the droplet from CMA #0 to CMA #1. Step 3 deactivates CMA #1 and activates CMA #2, which is an interim CMA. Step 4 deactivates CMA #2 and activates CMA #3. Sequencing through actuation step 1 to step 4 with appropriate timing would move the droplet from CMA #0 to CMA #3. After programming of microfluidic operations is done, it can be tested and saved for later use. A batch file containing a sequence of predefined microfluidic operations can achieve rather complex FPLOC programming and microfluidic operations.

CHAPTER 6. VALIDATIONS OF THE FIELD PROGRAMMABLE LAB-ON-A-CHIP

This chapter covers the validations and analysis of the FPLOC. There were three main areas of validations for the FPLOC: (1) BIST validation, (2) droplet actuation capability validation, and (3) droplet detection validation. The test setup is discussed in the first section including discussions of the test system, test control software and details of the droplet delivery system. The second section covers the three validations for the FPLOC. The BIST validation is discussed in Section 6.2.1. The droplet actuation capability validation is covered in Section 6.2.2, and the droplet detection validation is shown in Section 6.2.3.

6.1 Test Setup

6.1.1 Test System

Figure 6.1 illustrates the block diagram of the test setup for chip verifications of the FPLOC. Droplet actuation high voltages are generated by an Agilent 332200A 20 MHz Function/Arbitrary Waveform Generator and an A.A. LAB System A-303 High Voltage Amplifier and Modulator. Actuation data of microelectrodes are sequenced and delivered to the FPLOC by control signals from a NI PCIe-6537, 50 MHz Digital I/O, which is programmed by NI LabVIEW 2011 software. The NI PCIe-6537 interface card also performs the readout of droplet detection data from the FPLOC. Actual microfluidic operations are observed visually by a long working distance microscope (Optem 301400) and a CCD color camera (The Imaging Source DFK31AU03 USB CCD Color Camera). Videos are collected by a PC using IC Capture 2.2 software. The test fixture integrates the interface circuit, wiring, chip housing, positioning mechanics and the supporting structure of the top cover.

6.1.2 Test Control Software

There were four main software tools for validations of the FPLOC. Component Configuration Window was used to configure CMAs for droplet actuations. Microfluidic Operation Control

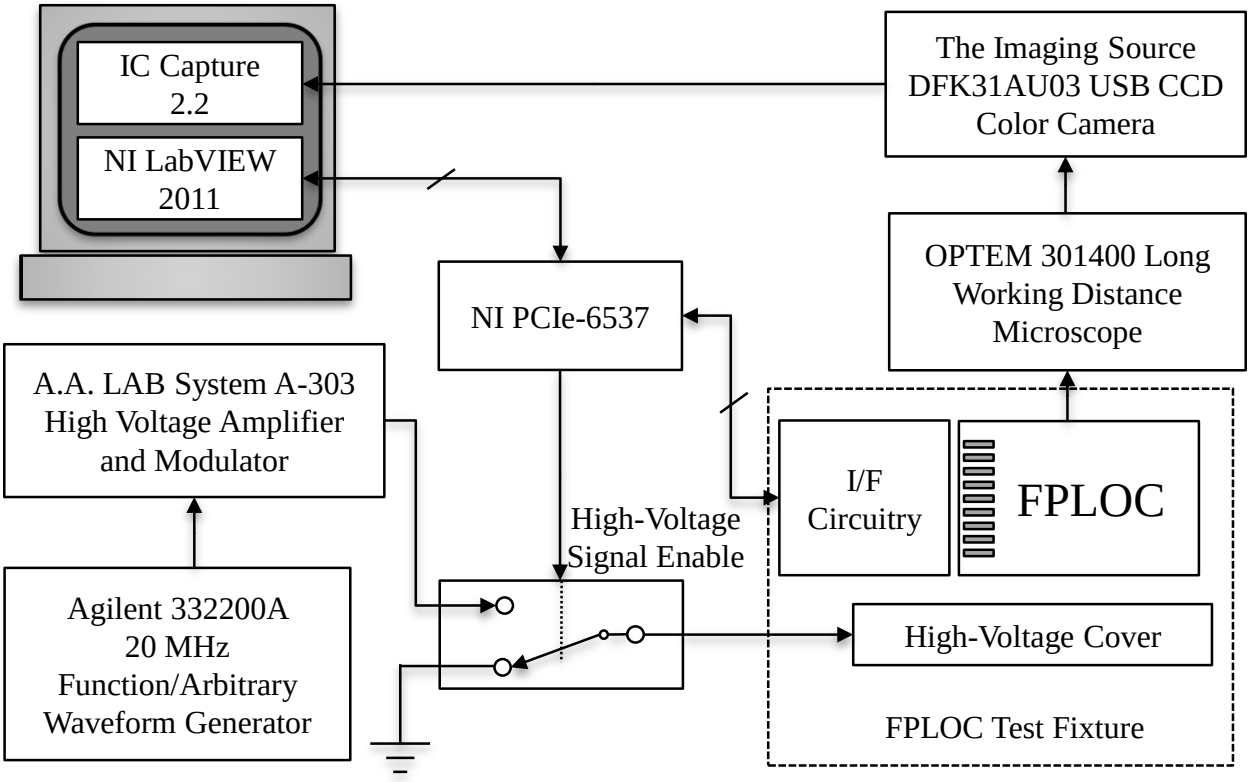

Figure 6.1. Block diagram of the FPLOC test system.

Window was used to actuate droplets for the FPLOC. Location Map software was used to check the readout from the output of daisy-chain shift registers and it also performed the real-time conversion of 900-bit droplet detection data into the droplet location map. Location Map software was the main software tool for validations of droplet detection. In addition, IC Capture 2.2 was used to capture all videos of microfluidic operations under the microscope.

6.1.3 Droplet Delivery System

A system integration analysis was performed after the completion of the FPLOC design. The goal was to make sure fundamental functional blocks needed for a DMFB were covered by the system design of the FPLOC. Ideally, the FPLOC should include all functional blocks, but after the system integration analysis, it was concluded that there were gaps in sample-reagent loading and sample preparation. Fundamental functional blocks needed for the FPLOC including sample

and reagents I/O ports, sample preparation, droplet manipulation, detection, and system control as shown in Figure 6.2. The design of the FPLOC covered most of the functional blocks except the highlighted areas shown in Figure 6.2. The FPLOC can perform some simple sample preparations, such as diluting. However, more advanced sample preparations, such as particle separation, would need to be done off chip. Also, the delivery of samples and reagents is not an easy task for the FPLOC, because of the small working area (1,142 μm × 1,142 μm) and other constraints such as bonding wires.

The guiding principle was that the FPLOC would include all functional blocks as a complete system, or at least gaps would be filled with compatible technologies to complete the system. To resolve the technical challenge of loading samples and reagents, it would involve a special interface between the outside world and the FPLOC [152]. A fluidic interface platform, which allows a seamless and simple integration of different fluidic modules for DMFBs, is highly desirable. The research effort of the three-dimensional microfluidic structure was aimed at solving this issue. In the following subsections, the relevance of the three-dimensional structure for the FPLOC is discussed. Details of the three-dimensional digital microfluidics are provided in Appendix A.

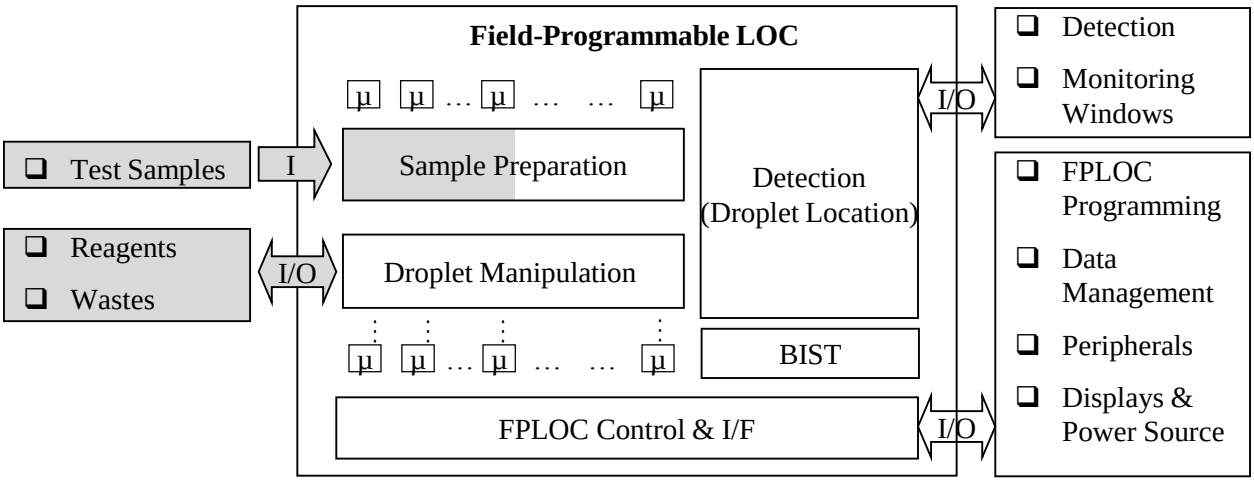

Figure 6.2. Block Diagram of microfluidic functions needed for the FPLOC.

6.1.3.1 Inter-Chip Bridge

The three-dimensional microfluidic system started from the "inter-chip bridge" concept. The goal was to have a fluidic interface technology that could enable a seamless and simple integration of fluidic modules by its inter-chip droplet transport capabilities [73]. The inter-chip bridge provides a viable modular FPLOC design solution before a monolithically integrated FPLOC could be achieved. In this modular system design, the FPLOC was partitioned into different function modules (sample-reagent loading, sample preparation, and the main chip), which were then linked together by the inter-chip bridge. This modular FPLOC design concept was used to solve the sample-reagent loading and sample preparation issues. Moreover, incompatible modules, such as glass-based and CMOS-based, could be combined into an FPLOC microsystem for heterogeneous integration. For example, a particle separation module, which might not be built by the CMOS fabrication technology, could be used in FPLOC system integration. Consequently, the FPLOC microsystem can be optimized (technical or cost wise) to a much better solution than if it were built only on CMOS technology.

The inter-chip bridge is fundamentally a dual open/covered DMFB configuration. In a dual open/covered DMFB, droplets can be actuated bi-directionally between the open and covered region [72]. Figure 6.3 illustrates the operation of the inter-chip bridge. In the figure, DMFB #1 (an open DMFB) and DMFB #2 (a covered DMFB) are connected by the inter-chip bridge. The open-to-covered actuation moves droplet A from the open DMFB #1 into the covered region between the bridge and DMFB #1 to become droplet B. Then the covered-to-open actuation moves droplet B from the covered region into the open region on the bridge to become droplet C. Again, another open-to-covered actuation moves droplet C into the covered region between the bridge and the DMFB #2 to become droplet D. This droplet bridging operation moves the droplet on DMFB #1 to DMFB #2. The reverse direction can also be performed.

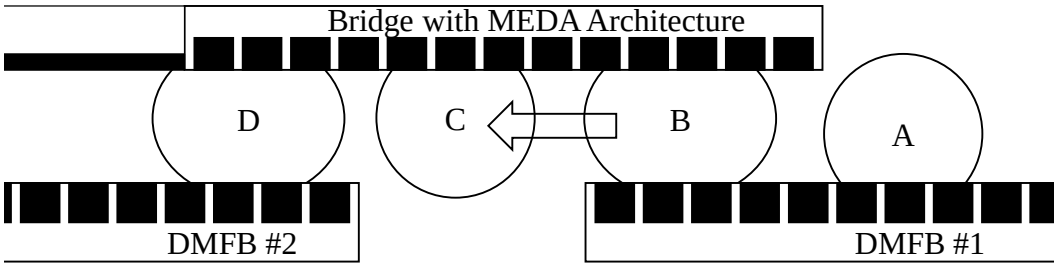

Figure 6.3. Sketch of the inter-chip bridge. DMFB #1 (an open DMFB) and DMFB #2 (a covered DMFB) are connected by the inter-chip bridge. Droplet A is delivered from DMFB #1 to DMFB #2 as droplet D.

The inter-chip bridge has some constraints in the relation between the gap and the droplet size. The covered-to-open droplet actuation is not possible if the gap is too large relative to the droplet volume. Similarly, the open-to-covered droplet actuation is not possible if the gap is too small [12, 72, 73]. These constraints prevented the inter-chip bridge (Figure 6.3) to be directly used as the interface between the outside world and the FPLOC due to the huge size discrepancy between real world samples (microliters) and FPLOC droplets (nanoliters). Therefore, a new technique called “dual-layer system” was introduced to solve the constraints by tilting the top plate. The tilted top plate provides an auto-adjusted gap height, and resolved the gap height and droplet size constraints of the inter-chip bridge [73]. Details of the inter-chip bridge and the dual-layer system are summarized as “Three-dimensional Digital Microfluidics” in Appendix A.

6.1.3.2 Combined Droplet Delivery System

A combination of the inter-chip bridge and the dual layer was used to construct the droplet delivery system for the FPLOC as shown in Figure 6.4. The right hand side is a dual-layer structure, which provides the solution for the needs of different droplet sizes with a tilted bottom plate. Droplet A, which is much bigger than the droplet size that the FPLOC could accommodate, is delivered by a pipette to the bottom plate. Because of the tilted plate structure, the droplet delivery system can work with a wider range of two droplet sizes: the one delivered

by the pipette and the droplet for the FPLOC. The bigger the Gap1 is, the bigger droplet A can be accepted by the droplet deliver system. Also, the smaller the Gap2 is, the smaller the droplet can be created and delivered to the FPLOC. Droplet A is moved from the open region into the covered region and becomes droplet B. Droplet creating is handled in the covered region. A smaller droplet C is created from droplet B, and droplet C is covered-to-open actuated to become droplet D. Droplet D is moved into the covered region of the FPLOC to become droplet E, and the cover plate with droplet E is pressed onto the FPLOC. Because the FPLOC chip is inside the CerDIP cavity and is 20 μm below the cavity frame, the vertical movement of the top cover shown in Figure 6.4 is taken to overcome the cavity constraint.

6.2 Results and Discussions

6.2.1 Built-In Self-Test

There were two BISTs performed for the FPLOC: the 900-BIST was performed to test the daisy-chained shift registers and the Metal-4 BIST was performed to test the metal-4 microelectrode and the droplet detection circuit. The Microfluidic Operation Control Window was used to generate test control signals and actuation patterns and the oscilloscope was used to visually inspect the input and output signals of the scan-chain. Typically, the 900-BIST was

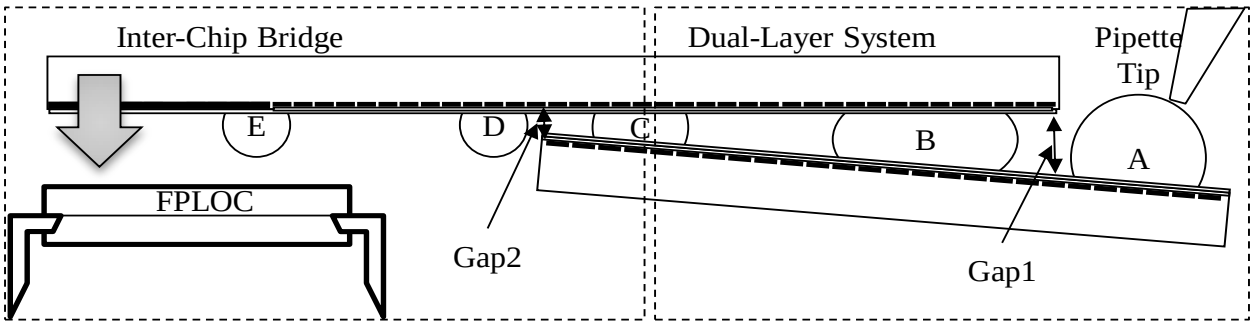

Figure 6.4. The droplet delivery system for the FPLOC.

performed by a set of testing configurations: SET, REST, regular patterns and irregular patterns. Through the entire research, the standard operating procedure was to perform the 900-BIST right after every power-up of the FPLOC to ensure the operability of the FPLOC. As shown in Figure 6.5(a), the oscilloscope displays IN, OUT and CLK waveforms for the 900-BIST. The green waveform is the IN signal, the blue waveform is the OUT signal, and the pink signal is the CLK signal. A pair of identical but reverse IN and OUT signals, which can be easily verified by the naked eye, ensure the integrity of the 900-bit shift registers.

The Metal-4 BIST was not a convenient test because it was very time consuming. The Metal-4 BIST was difficult to perform due to the difficulty and reliability of the manual adjustment of the appropriate time delay (Δt) of the CLK signal. Every FPLOC inserted into the test fixture required a new adjustment of Δt to be able to perform the Metal-4 BIST because FPLOC removing and inserting on the 48-pin IC socket always created too much variation of Δt. The adjustment of Δt was not an easy task because the capacitance between the metal-4 microelectrode and the metal-3 shielding layer is very small (18 fF). Typically, the Metal-4 BIST was performed in a sweeping mode, in which Δt was swept through a wide range to trigger some changes of the OUT signal (the pink waveform in Figure 6.5(b)) for the area of concerns. The reliability and usability of the Metal-4 BIST have room for improvement, especially the adjustments of Δt.

All 15 FPLOCs received from TSMC passed both the 900-BIST and the Metal-4 BIST. Both BISTs became very useful tools in catching FPLOC chip failures. Through the research, the most common defects detected by the 900-BIST were: (1) broken bonding wires, (2) shorts of bonding

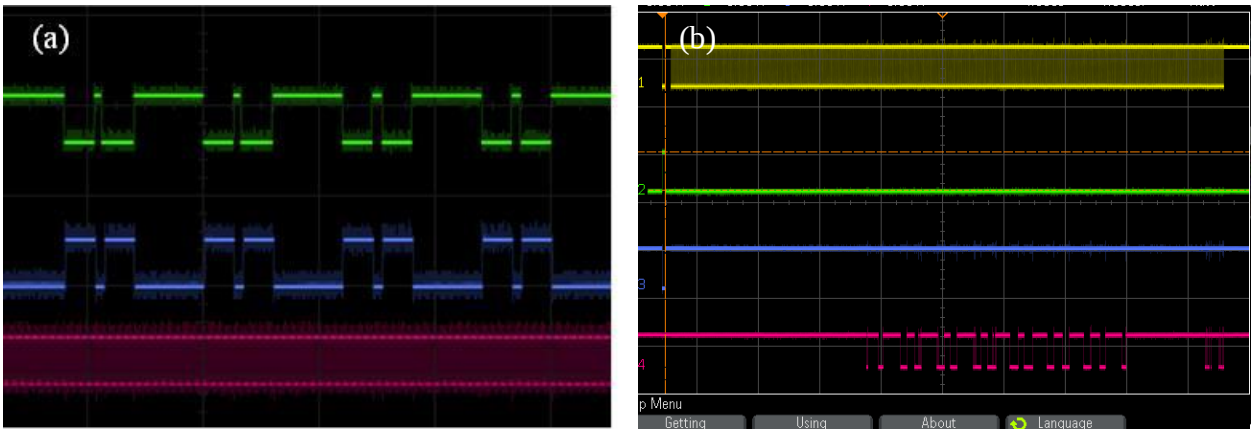

Figure 6.5. BISTs: (a) the 900-BIST for the test of daisy-chained shift registers; (b) the Metal-4 BIST is used to check the droplet detection circuit and the metal-4 microelectrode.

wires, and (3) damages of microelectrodes. The Metal-4 BIST also detected FPLOC failures, which were mainly broken connections between metal-4 microelectrodes and bi-state-switch drivers. This kind of failure typically was caused by the physical damage of the microelectrodes from direct probing.

Main purposes for BISTs are in two areas: (1) tools to bring up FPLOCs and (2) the demonstration of the advantages of the MEDA architecture in effective testing of DMFBs. It has been identified that effective testing of DMFBs remains an open problem. DMFB defects associated with thermal effects are difficult to detect. More efficient testing in covering and identifying failures is required for DMFBs [146]. The scan-chained structure of the MEDA architecture is more convenient to implement the BIST and the design-for-testability (DFT) for DMFBs as demonstrated by the FPLOC BISTs.

6.2.2 Droplet Actuation Capability Validation

DI-water droplets in silicone oil with 300-μm to 20-μm gaps were tested for droplet actuations of the FPLOC. The EWOD actuation force from the bi-state-switch driver was not strong, the original contact angle was 107 degrees and the actuated contact angle was 87 degrees, so the

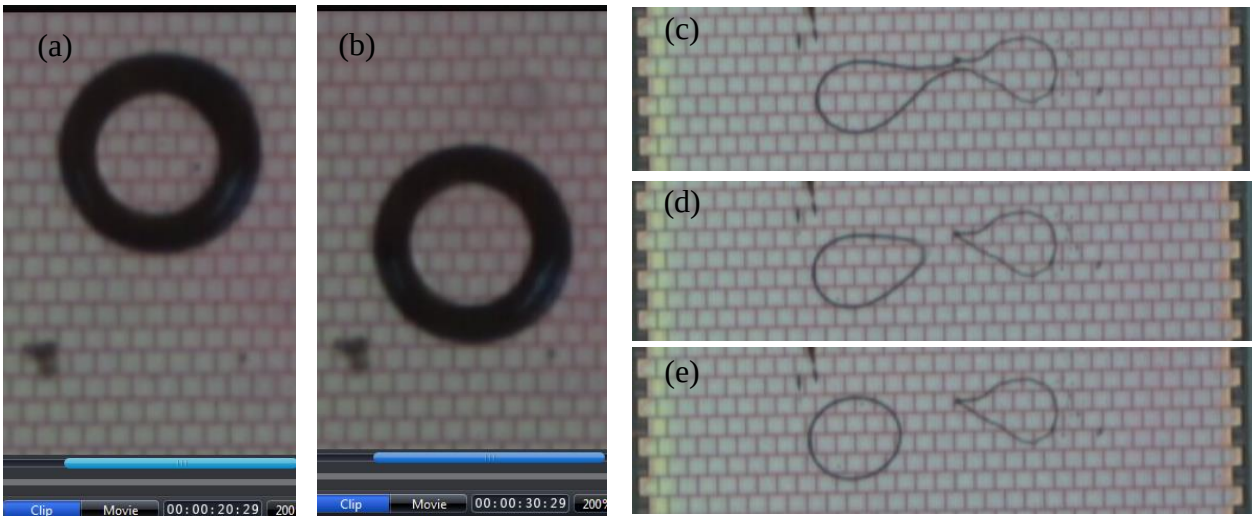

Figure 6.6. FPLOC droplet actuations through the control of the Microfluidic Operation Control Window: (a) and (b) show the droplet movement by EWOD actuations with 220 μm gap height; (c) electrode-column droplet cutting is pulling a small droplet from a pinned droplet; the gap height is 20 μm; (d) the droplet pinched off; (e) the droplet is actuated away.

electrode-column actuation (Figure 4.9) was applied to help actuations of droplets. As a result, droplets could be successfully actuated through the control of the Microfluidic Operation Control Window to move around the FPLOC. Figure 6.6(a) and (b) show the pictures of the droplet movement by activating CMAs. The attempt of three-CMA cutting was not successful due to the limited actuation forces of the CMAs. The only cutting (as well as droplet creating) operation performed successfully was electrode-column cutting of a droplet, which was pinned at two sticky spots on the microelectrode array surface, as shown in Figure 6.6(c)-(e). Overall, experimental results of the FPLOC droplet actuation were in line with the expectations that leakage currents of the bi-state-switch driver reduced the capability of droplet actuations, but EWOD droplet actuations could still be achieved by the low-voltage CMOS technology.

The fabrication of the FPLOC with TSMC 0.35 micron 3.3 V standard CMOS technology was enabled by the bi-state-switch driver. In the actuation validation, the high-voltage was applied to the top plate, and the bi-state-switch driver was set to low (0-state) to activate the

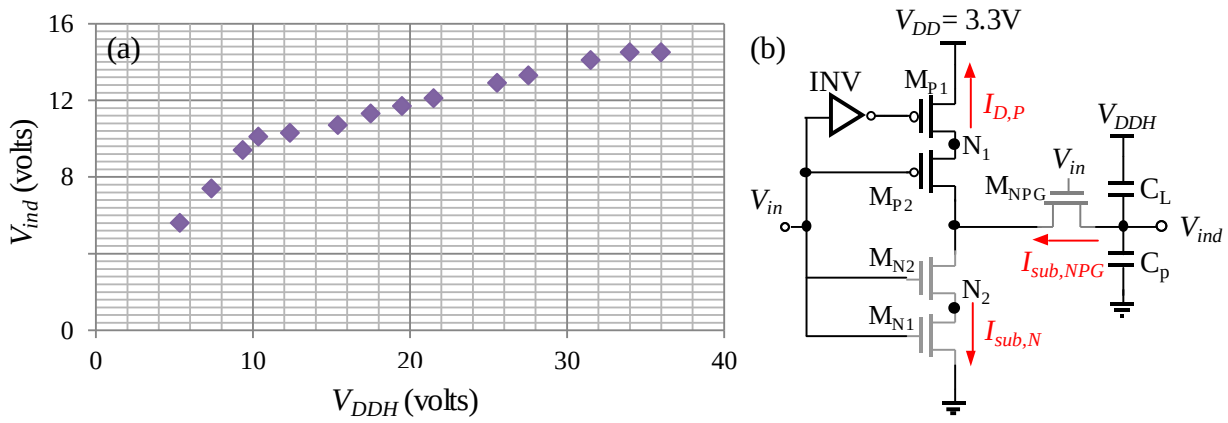

Figure 6.7. Induced voltages and leakage currents: (a) measured induced voltages vs. applied voltages of the FPLOC microelectrode; (b) leakage currents of the bi-state-switch driver in the high impedance mode.

microelectrode. The high-impedance mode (x-state) of the bi-state-switch driver deactivated the microelectrode. In the ideal situation, the high impedance mode should result a zero electric potential between the high voltage top plate and the deactivated microelectrode. In reality, leakage currents did exist and the induced voltage on the deactivated microelectrode was not able to follow the applied voltage on the top plate. Measurements of induced voltages were performed in the FPLOC droplet actuation validation. The results are shown in Figure 6.7(a) where the applied voltage is V_{DDH} and the induced voltage on the microelectrode is V_{ind}. For low applied voltages (less than 10.3 V), the relation between the induced voltage V_{ind} and the applied potential V_{DDH} shows a linear dependence. When the applied voltage is greater than 10.3 V, the induced voltage is not increasing as fast as the applied voltage. The induced voltage V_{ind} has a saturation asymptote at 14.5 V.

Figure 6.7(b) shows the schematic of the bi-state-switch driver, which consists of an inverter and five transistors. V_{DDH} is the applied voltage on the top plate. When V_{in} transits from high to low, it turns off M_{N1}, M_{N2} and the path NMOS gate M_{NPG}. This puts the bi-state-switch driver into x-state (high-impedance mode). In the high-impedance mode, V_{ind} is expected to be induced

to high voltage V_{DDH}. However, the subthreshold leakage current $I_{sub,NPG}$ discharges the electric potential of V_{ind}, which consequently degrades the performance of the driver. $I_{sub,NPG}$ is then divided into two current paths: one is the reverse current $I_{D,P}$, and the other is the sub-threshold leakage current $I_{sub,N}$. For those leakage currents affecting V_{ind}, the primary source is the sub-threshold leakage current $I_{sub,NPG}$, which is caused by a large voltage drop on M_{NPG}. The sub-threshold leakage current I_{sub} is expressed as [153, 154]

$$I_{sub} = \mu C_{dep} \frac{W}{L} V_T^2 exp\left(\frac{V_{GS} - V_{th}}{nV_T}\right)\left(1 - exp\left(\frac{-V_{DS}}{V_T}\right)\right), \tag{6-1}$$

where μ is the effective mobility; C_{dep} is the depletion capacitance; W is the device width; L is the effective channel length; V_T is the thermal voltage; V_{GS} is the gate-to-source voltage; V_{th} is the threshold voltage; n is the sub-threshold slope factor; V_{DS} is the drain-to-source voltage. V_{ind} can be derived as

$$V_{ind} \approx \frac{C_L}{C_p + C_L} \cdot V_{DDH} - \frac{1}{C_L}\left(\int_{T_1} \left[I_{D,P}(V_{DS}) + I_{sub,N}(V_{DS})\right] dt\right), \tag{6-2}$$

where C_p is the parasitic capacitance on the node of V_{ind}. For V_{DDH} over 10.3 V, the reverse leakage current starts to affect the output potential level, and V_{ind} is not increasing as much as V_{DDH}. When V_{DDH} continues to increase to around 35 V, the avalanche breakdown happens. As a result, V_{ind} maintains constant at around 14.5 V.

Leakage currents and limited V_{ind} did have a complicated impact on the droplet actuation of the FPLOC. From Figure 6.8, it can be seen that there are two capillary forces acting on the droplet in the unit vector $\vec{\imath}$ direction. One is the actuated force induced by V of the activated electrode, and another is the hindering force induced by the electric potential difference between V and V_{ind} of the deactivated electrode. The hindering force generated by leakage currents

reduces the overall droplet actuation force of the FPLOC. According to the discussion of the capillary force of the droplet in Chapter 2, the actuated force F_V induced by V (equation (2-22)) in the unit vector $\vec{\imath}$ direction is expressed as

$$F_V = \gamma \cos\theta(V) \int_L dl\vec{n} \cdot \vec{\imath} = \gamma \cos\theta(V) e \,, \tag{6-3}$$

where γ is the surface tension and $\theta(V)$ is the contact angle with the potential V. The hindering force F_H induced by $V - V_{ind}$ of the deactivated electrode in the unit vector $\vec{\imath}$ direction is

$$F_H = -\gamma \cos\theta(V - V_{ind})\, e \,, \tag{6-4}$$

where $\theta(V - V_{ind})$ is the contact angle resulted from the difference between the applied V and the induced voltage V_{ind} for the deactivated microelectrode. The net actuation force F_x acting on the droplet in the unit vector $\vec{\imath}$ direction is

$$F_x = F_V + F_H = \gamma \cos\theta(V)\, e - \gamma \cos\theta(V - V_{ind})\, e \,, \tag{6-5}$$

$$F_x = \gamma(\cos\theta(V) - \cos\theta(V - V_{ind}))e \,. \tag{6-6}$$

Based on the measured 107° non-actuated contact angle and the calculated 31.93 pF/mm^2 capacitance of the dielectric and hydrophobic layers of the FPLOC, the Lippmann-Young equation (equation (2-17)) was used to predict the contact angles of different applied voltages.

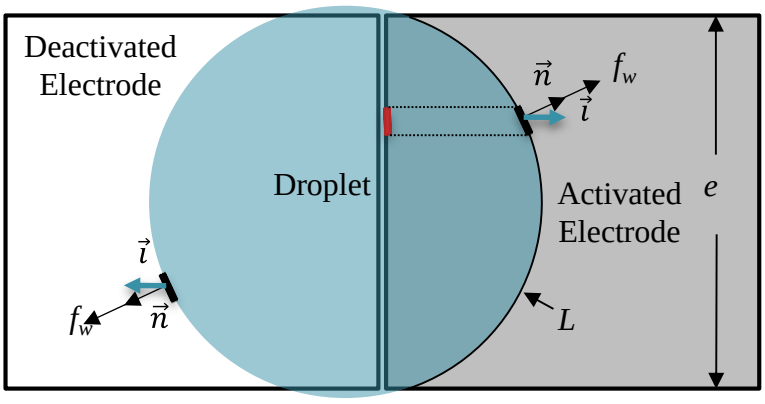

Figure 6.8. EWOD actuation forces acting on the droplet in the unit vector $\vec{\imath}$ direction (FPLOC).

Pairs of $V\ and\ V - V_{ind}$ were generated from the empirical data shown in Figure 6.7(a) and then applied into equation (6-6) to predict the capillary force F_x. This exercise predicted the droplet would start to have positive F_x around applied V = 25 V, and then F_x would peak at around V = 30 V. After that, V > 30 V, F_x had no gain but reduced again. The results from the exercise provide an explanation for the experiment results described below. When the actuation voltage was around 25 V, most droplets started to be actuated. Also, the best working window for EWOD actuations stayed between 25 V to 30 V. Voltages over 30 V did not gain any actuation performance improvement.

The minimum droplet actuation voltage for the FPLOC was expected to be around 18 V, assuming no impact from leakage currents. Leakage currents, as expected, complicated the droplet actuations of the FPLOC. Although three-CMA cutting, which requires stronger actuation forces, was not achieved, the transport actuations of droplets have been achieved by the 3.3 V CMOS technology. There are possible solutions to improve the performance of the bi-state-switch driver. High-voltage operations using standard low-voltage CMOS processes can be achieved by modified device structures. Several such works have been reported, e.g. techniques of the extended drain MOS [155] and gate-shifted LDD-MOS [156]. These techniques can be potentially utilized to improve the performance of the bi-state-switch driver. In addition, hierarchical programming of the FPLOC has been very successful. Configurations of CMAs and microfluidic operations were seamlessly executed. At the microfluidic component layer, all microfluidic components for microfluidic operations were defined, and the Microfluidic Operation Control Window handled the sequences and actuation timing for the droplet manipulations.

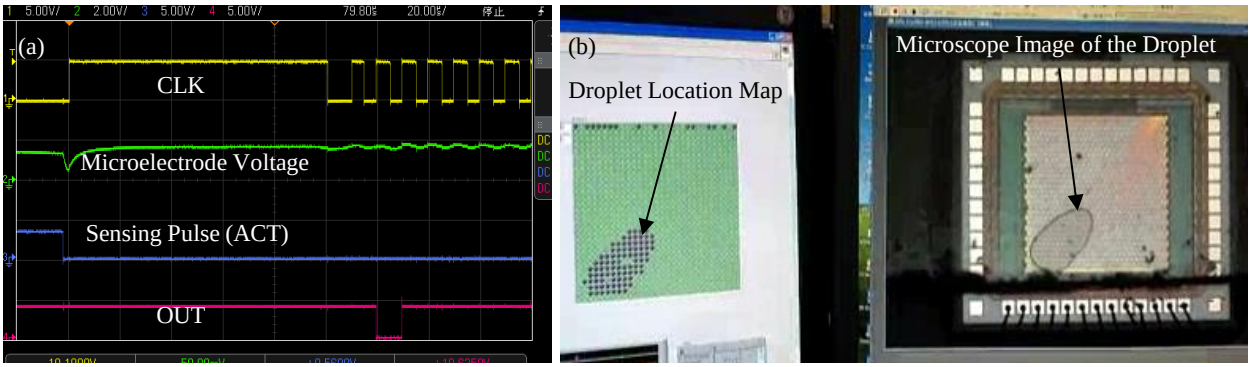

Figure 6.9. FPLOC droplet detection validation: (a) the test of a single microelectrode; (b) the real-time droplet location map in comparison to the actual droplet image.

6.2.3 Droplet Detection Validation

The droplet detection function was successfully demonstrated by the FPLOC. The test of the droplet detection function was conducted in two steps: (1) functional verifications of the droplet detection circuit were performed on individual microelectrodes; (2) integrated droplet detection in the form of the droplet location map was checked. A screen shot of the functional verification on individual microelectrodes is shown in Figure 6.9(a). In this functional verification, the microelectrode was loaded with 12 pF capacitance, which came from an oscilloscope probe, and the droplet detection circuit was checked against the loaded capacitance. The falling edge of Sensing Pulse (ACT) initiates the discharging cycle, and the rising edge of the CLK signal clocks in the detection result. Then the detection mode is switched back to the read-out mode, and the OUT signal shows a low bit which indicates a droplet (capacitance loading) is detected.

Figure 6.9(b) shows the real-time comparison between the droplet location map and the actual droplet image. The Location Map software interpreted the 900-bit OUT pattern into a graphical droplet location map, which resembled the actual droplet. There were two factors that could influence the accuracy of the droplet location map. The first issue, which is minor, was that the droplet location map was constructed and displayed based on a square microelectrode array

instead of the actual wall-brick format. Unfortunately, it was not an easy task to implement the wall-brick microelectrode array on the graphical interface of LabVIEW, so it was decided not to spend the effort. The second factor was the threshold level of droplet detection. The change of the threshold level of droplet detection could cause different detection results for those bordering microelectrodes that were not fully covered by the droplet. Consequently, the boundary line of the droplet location map would be changed. Regardless impacts from the two factors, overall, the droplet location map did accurately reflect the position of the droplet.

Based on the MEDA architecture, the size of the microelectrode is typically expected to be reasonably small relative to the size of the CMA so that the desired CMA shape can be accurately configured by microelectrodes. Based on this assumption, a qualitative yes-no droplet detection could serve the purpose for measuring the size of the droplet. For example, a droplet created by 1 mm × 1 mm solid electrodes might require a precise capacitive detector to determine the volume of the droplet. On the other hand, the droplet location map of the FPLOC could serve as a handy tool for the measurement. For the FPLOC, a 1 mm × 1 mm CMA would be composed of 27 × 27 microelectrodes because each microelectrode is 37.1 μm × 37.1 μm with 1-μm spacing in between. These 729 microelectrodes would have an area measurement resolution of 18.55 μm × 18.55 μm, assuming the droplet detection threshold is defined at 50%. The droplet location map can be used to calculate the number of microelectrodes covered by the droplet. The volume of the droplet is determined by multiplying the size of the microelectrode, the number of covered microelectrodes and the gap height. Of course, a more precise measurement could also be performed by a more accurate boundary line, which can be achieved by setting up multiple detection thresholds along with multiple scans.

CHAPTER 7. CONCLUSIONS AND FUTURE WORK

Early work in DMFBs has demonstrated promising results of the tremendous potential in transforming the POC diagnostics industry, but further developments to integrate DMFBs into field-deployable systems for POC diagnostics are surely required [3, 14]. The development of the DMFB has been hindered by the absence of: integrated detector technology, standard commercial components, on-chip sample preparation, standard manufacturing technology, low cost, and end-to-end system integration [55, 87, 157]. At the moment, the development of the DMFB is awaiting break-through in converting laboratory demonstrations into high volume commercial devices. To move forward, the future of the DMFB development will require the collaboration of multiple disciplines, such as biology, physics, chemistry, and engineering, to bridge the technology gaps and achieve commercialization. This research was aimed at providing enabling technologies that pave a potential path which may lead us to the vision that DMFBs will copy the success of digital integrated circuits. In this chapter, the research contributions are listed in the first section, including the list of published papers. The research scope and limitations are discussed in the second section. Conclusions and future work are presented in the last two sections.

7.1 Contributions

- A possible bridge between the high-tech industry and the bio-tech industry lies in the DMFB technology. The DMFB technology has been long advertised as one of the most promising biochip technologies, and it is the biochip technology most compatible to microelectronics. The MEDA architecture is the enabling technology, which can be used to advance integration of the DMFB technology and microelectronics, such that electrical engineering technologies and digital microfluidics can be fully integrated to provide advanced biochemical solutions.

- The MEDA architecture has been motivated by the analogy and compatibility between DMFBs and ASICs. Similar to the development of the ASIC that all logic gates and digital circuits are made of CMOS field-effect transistors, microfluidic components and microfluidic operations can be configured from standard DMFB building elements (microelectrode cells) in the development of the MEDA-architecture DMFB. DMFBs based on the architecture can be fabricated by well-established and commonly available manufacturing technologies. The MEDA architecture paves a possible path for future DMFB developments by copying the success of the development of the ASIC.
- The design of the microelectrode cell was implemented by taking the CMOS standard cell approach. The demonstration of the FPLOC microelectrode cell was the first step toward the ultimate design goal that the microelectrode cell will be included in the standard-cell library in the next generation SoC design. Along with DMFB development advances, the standard cell methodology will help designers to scale DMFBs from comparatively simple single-function DMFBs to complex multi-functional DMFBs.
- A prototype of the FPLOC was successfully fabricated and demonstrated in this research. The field-programmability and the seamless hierarchical programming capability of the FPLOC might establish a new design approach of DMFBs. The FPGA-like design approach could be a significant breakthrough for DMFB designers. The FPLOC has the potential to become a strong development tool for future DMFB developments, especially used in fast prototyping, education/training and quick-time-to-market product developing.
- Many advanced microfluidic operations, which cannot be achieved by conventional EWOD systems, were successfully demonstrated by the MEDA architecture. The study of droplet routing based on the MEDA architecture indicated that advanced microfluidic manipulations

such as diagonal transport and channel-based transport can significantly improve the droplet routing performance.

- Research of the MEDA architecture inevitably would need to examine basic EWOD principles in much deeper levels both from the simulation and experiment point of view. Modeling, experiments and result analyses of the MEDA architecture have contributed some first-hand research data regarding the impact from the spacing between microelectrodes.
- The bi-state-switch driver was designed to enable the fabrication of the FPLOC with the low-voltage CMOS technology. Although the first implementation of the bi-state-switch driver was not perfect, it successfully demonstrated the EWOD droplet actuation capability. The FPLOC prototype is the first DMFB built by 3.3 V standard CMOS technology. The technology gaps between the low-voltage CMOS technology and the DMFB have been analyzed through the FPLOC prototype. The causes and possible solutions have been identified for future performance improving of the driver. The development of the bi-state-switch driver not only deepened the knowledge of CMOS fabrications of DMFBs but also potentially moved more DMFB developments into the electrical engineering domain.
- Advanced CAD tools will be essential to future DMFB developments. The MEDA architecture serves as the bridging technology that many existing CAD tools and applications for ASIC designs can be leveraged for future developments of DMFBs. National Instruments' graphical programming language LabVIEW was leveraged to demonstrate the hierarchical programming and controlling of the FPLOC. In addition, the CMOS standard cell design approach of the microelectrode cell was aimed at the full leverage of the ASIC CAD tools for future DMFB developments. The hierarchical architecture, standard DMFB building elements, the CMOS standard cell approach and the field-programmability

demonstrated the feasibility of the top-down design automation that can drastically simplify the DMFB design and programming processes.

- An integrated droplet detection circuit, which can detect the locations of all existing droplets on the FPLOC, was successfully demonstrated. A total of 900 one-bit CMOS-based capacitive detectors were integrated into the microelectrode array to demonstrate the capability of large-scale on-chip integration of microelectronics and microfluidics. This demonstration substantiated the possibility of future DMFB integration with ultrasensitive CMOS-based capacitive sensors, CPU, memory and other microelectronic components.
- In this research, the daisy-chained control structure for DMFBs was proposed. With the proposed daisy-chained control structure, the number of control pads can be reduced for accommodating pad-limited DMFB designs. The FPLOC demonstrated the individual controllability of 900 microelectrodes by three control pads. In addition, the daisy-chained structure is more convenient to implement the built-in self-test and the design-for-testability for DMFBs.
- Published Research Papers:

    1. G. Wang, D. Teng and S.-K. Fan, "Digital microfluidic operations on microelectrode array architecture," in *Proceedings of the 2011 IEEE International Conference on Nano/Micro Engineered and Molecular Systems (NEMS)*, Kaohsiung, Taiwan, pp. 1180-1183, 20-23 February 2011.
    2. G. Wang, D. Teng and S.-K. Fan, "Digital microfluidic operations on microelectrode dot array architecture," *IET Nanobiotechnology*, vol. 5, no. 4, pp. 152-160, December 2011.
    3. Z. Chen, D. Teng, G. Wang and S.-K. Fan, "Droplet routing in high-level synthesis of configurable digital microfluidic biochips based on microelectrode dot array architecture," *BioChip Journal*, vol. 5, no. 4, pp. 343-352, 20 December 2011.
    4. G. Wang, D. Teng and S.-K. Fan, "Three-dimensional digital microfluidics and applications," in *Proceedings of the 2012 7th IEEE International Conference on*

Nano/Micro Engineered and Molecular Systems (NEMS), Kyoto, Japan, pp. 415-418, 5-8 March 2012.

5. G. Wang, D. Teng, Y.-T. Lai, Y.-W. Lu, Y. Ho and C.-Y. Lee, "Field-programmable lab-on-a-chip based on MEDA architecture," *IET Nanobiotechnology*, accepted, July 2013.

7.2 Scope and Limitations

Significant contributions have been made by researchers in chemistry and physics for DMFB developments. The DMFB design has expanded to involve all major scientific and engineering disciplines including: engineering (electrical, biomedical, mechanical and chemical), chemistry, physics, biology, computer science and manufacturing technology. It often requires the collaboration of multiple teams and organizations from different disciplines for the DMFB development [4]. This broad multidisciplinary scope makes it challenging to understand all aspects of the DMFB development. Therefore, it is important to explain the scope and limitations of this research.

- This research is based on a belief that the CMOS technology is a good candidate for manufacturing DMFBs. The integration of microelectronics and microfluidics through the CMOS technology provides one of the best ways to integrate advanced detection technologies into DMFBs. There are existing technologies such as polydimethylsiloxane (PDMS), Mylar, polycarbonate [55], and thin-film transistor (TFT) [59] that have been used for manufacturing microfluidic devices. This research pointed out one of the possibilities, but it did not cover comparisons and analyses of all available manufacturing technologies.
- Overall, this research worked on narrowing the technology gaps and paving a path for future developments of DMFBs. It mainly focused on proof-of-concept experiments and analyses of the MEDA architecture. ITO-glass-based prototypes and the CMOS-based FPLOC were used to demonstrate the key features of the MEDA architecture. Perfection of the MEDA

architecture and related technologies was not the goal of this research.

- Top-down design automation, DMFB CAD tools, and the FPLOC would be very helpful along advances of future DMFB developments. This research demonstrated the feasibility of the FPLOC, but the FPLOC prototype is still at a conceptual stage and would require major research and engineering efforts in order to commercialize the FPLOC.
- This research mainly focused on the integration of microfluidics and microelectronics. Mechanical, chemical, biomedical and other engineering involvements were very limited.
- Along with the research progress, some new techniques, such as the daisy-chained control structure and the bi-state-switch driver, were designed to overcome technical challenges. Each of these new technologies could be independent research topics, and this research only focused on the feasibility of the new technologies.
- Microfluidic operations in this research were performed only on DI water with air or silicone oil as the filler medium. Other droplet types were not used.
- The size optimization of microelectrode cells was not covered by this research. Ultimately, the size of the microelectrode cell would be strongly influenced by DMFB applications. In biomedical applications, concentrations of analytes would most likely be the key factor of deciding the size of the microelectrode cell. This research studied two microelectrode sizes: one was 100 μm × 100 μm for ITO-glass prototypes and another was 37.1 μm × 37.1 μm for the FPLOC with 0.35 μm CMOS technology. Both sizes demonstrated the limitations of the fabrication technologies, and they were not driven by real DMFB applications.
- The feasibility of the standard cell design approach of the microelectrode cell was demonstrated, but the full standard cell design of the microelectrode cell is in future work.
- No full top-down design automation demonstration.

7.3 Conclusions

The DMFB technology has been long advertised as one of the most promising biochip technologies, and it is also the biochip technology most compatible to microelectronics. There are some technical challenges remaining to be resolved to advance the DMFB development. Motivated by the analogy and compatibility between DMFBs and ASICs, these technical challenges were taken as opportunities to drive the development of the MEDA architecture as the solution.

The main challenges of the DMFB development are (1) on-chip detection integration, (2) end-to-end system integration, (3) top-down design automation, and (4) mass production technology and processes. This research proposed the MEDA architecture as the enabling technology for bridging these technology gaps. To prove the concept of the MEDA architecture, numerical simulations were performed and ITO-glass prototypes were fabricated to conduct extensive experiments to verify the digital microfluidic functionality of the MEDA architecture. The results were very successful. The architecture not only can perform all basic microfluidic operations (creating, transport, cutting, and mixing) but also delivers some advanced microfluidic operations such as electrode-column actuation and diagonal transport.

Integration of microelectronics and microfluidics through the CMOS technology provides one of the best ways to integrate advanced detection technologies into DMFB systems. As a result, the implementation of the architecture based on the CMOS technology was demonstrated by the FPLOC prototype. The FPLOC prototype exhibited the feasibility of on-chip CMOS-based capacitive detection integration. By integrating 900 droplet detection circuits into microelectrode cells, the FPLOC also achieved large scale integration of microfluidics and microelectronics. In addition, the inter-chip bridge was also demonstrated to provide a viable modular FPLOC design solution before a monolithically integrated FPLOC could be achieved.

To move beyond the limit of current high-voltage-only DMFB fabrication technologies, this research demonstrated the feasibility of the first DMFB fabricated by the standard low-voltage CMOS technology. This achievement has positioned the well-established and commonly available low-voltage CMOS technology as a good candidate for the mass production of future fully integrated DMFBs or POC diagnostic devices.

To speed up the development of DMFBs, system wide top-down design automation will be essential. The lack of standard DMFB components makes the implementation of the hierarchical top-down design approach for DMFBs difficult. The MEDA architecture offers standard DMFB building elements, microelectrode cells, to enable the top-down design automation. Microfluidic components, operations and applications can be implemented by dynamic configurations of a sea-of-microelectrode array. Also, the microelectrode cell has been designed by following the CMOS standard cell approach that established the possibility of integrating digital microfluidics into next generation SoC designs. Configurability, scalability, and portability, which are critical aspects of standard DMFB building elements, have been successfully demonstrated by MEDA microelectrode cells.

The FPLOC based on the MEDA architecture has demonstrated the seamless and easy configuration of microfluidic components and operations by hierarchical software programming. It proved the feasibility of a real field-programmable and reusable DMFB. Flexible field-programmability, fast turnaround time and low non-recurring engineering costs could make the FPLOC a good alternative in the future development of DMFBs.

In summary, all research objectives have been successfully achieved. The research results suggested that the MEDA architecture is a viable enabling technology to advance the development of DMFBs by using CMOS technologies. The architecture fosters the development

path that electrical engineering technologies and digital microfluidics can be fully integrated to provide advanced biochip solutions.

7.4 Future Work

The results of this research bring up many exciting DMFB research possibilities in the emerging areas of on-chip detection, system integration, manufacturing technologies and processes, and top-down design automation. Future works that are most relevant in making this research more valuable are summarized below.

1. A highly efficient bi-state-switch driver: The actuation capability of the bi-state-switch driver has been identified as the biggest gap of implementing the FPLOC by the standard low voltage CMOS technology. Limited by the actuation capability of the bi-state-switch driver, the FPLOC prototype couldn't perform all microfluidic operations. The causes and possible solutions have been identified for improving the performance of the driver. The design goal of the new bi-state-switch driver is to achieve 30+ V induced voltage, which would give enough actuation forces for all microfluidic operations.
2. An integrated high-sensitivity CMOS-based capacitive sensor: CMOS-based capacitive sensing technologies have recently created substantial interest for a wide variety of biochemical detection applications. Early work has demonstrated that it is very promising to achieve low detection limits for biochemical detection applications by using CMOS-based capacitive sensors. A micromachined silicon gyroscope [158] is capable of providing ultrasensitive capacitance detection (~12 zF sensitivity) with a fully integrated CMOS-based capacitive sensor. CMOS-based ultrasensitive capacitive sensors for biosensing applications have achieved the sensitivity of a minimum detectable capacitance change of 0.3 aF [122]. In addition, low cost and high sensitive CMOS-based capacitive sensors have been designed and built for gaming controllers, and they are fabricated by standard low-voltage CMOS

technologies. The MEDA architecture enables the fabrication of DMFBs by standard low-voltage CMOS technologies; therefore, these capacitive sensors can be easily integrated into the biochip. Possible specifications for the integrated CMOS-based capacitive sensor would be: 0.2 fF measurement resolution, 2 μs refresh cycle and self-calibration capabilities.

3. Top-down design automation for the FPLOC: Hierarchical top-down programming of the FPLOC can be done automatically. At the first level, descriptions of biomedical applications are translated into a set of microfluidic operations. The second level manages the microfluidic operations, including routing algorithms, types of microfluidic operations and timing sequences in software expressions. These software expressions of microfluidic operations are synthesized into physical microfluidic components and actuation step timings. The third level configures and manages microfluidic components to implement the microfluidic operations. At the bottom level, these microfluidic components are mapped into different groups of identical microelectrodes. Top-down design automation translates high-level biomedical function descriptions into physical groupings and activating timing steps of microelectrodes. In addition to the software design effort, an FPLOC with more microelectrodes will be necessary for implementing top-down design automation. So far all droplet routing algorithms performed for DMFBs were based on mathematical models. A full functioning and larger scale FPLOC would also provide a real DMFB platform for physical verifications of the algorithms.
4. System packaging improvements of the FPLOC: The through-silicon via (TSV) technology from the three-dimensional IC fabrication and an improved inter-chip bridge structure are two key elements for achieving system packaging improvements. The TSV technology can remove the chip packaging constraint of bonding wires by moving chip connections (the ball

grid array) to the bottom of the substrate. Better mechanical designs of the inter-chip bridge structure improve the robustness of the system and the world-to-chip interface, which brings the convenience of delivering samples and reagents to the FPLOC. In a modular system design, the FPLOC is partitioned into different function modules (e.g. sample-reagent loading, sample preparation, and the main FPLOC chip), which are then linked together by the inter-chip bridge. Moreover, incompatible modules, such as non-CMOS-based sample preparation modules, could be combined into an FPLOC microsystem for heterogeneous integration.

5. A demonstration of a biomedical application on the next generation FPLOC with integrated high-sensitivity capacitive detectors: The possible application is the immunoassays of the prostate-specific antigen (PSA), which has the analyte concentration level of fM to nM. This project requires collaborative efforts of several teams and organizations.

LIST OF REFERENCES

[1] A. Manz, N. Graber and H. M. Widmer, "Miniaturized total chemical analysis systems: a novel concept for chemical sensing," *Sensors and Actuators B: Chemical,* vol. 1, no. 1, pp. 244-248, January 1990.

[2] E. Verpoorte and N. F. de Rooij, "Microfluidics meets MEMS," *Proceedings of the IEEE,* vol. 91, no. 6, pp. 930-953, June 2003.

[3] C. D. Chin, V. Linder and S. K. Sia, "Commercialization of microfluidic point-of-care diagnostic devices," *Lab on a Chip,* vol. 12, no. 12, pp. 2118-2134, 21 June 2012.

[4] A. Rios, M. Zougagh and M. Avila, "Miniaturization through lab-on-a-chip: utopia or reality for routine laboratories? a review," *Analytica Chimica Acta,* vol. 740, pp. 1-11, 31 August 2012.

[5] M. L. Kovarik, D. M. Ornoff, A. T. Melvin, N. C. Dobes, Y. Wang, A. J. Dickinson, P. C. Gach, P. K. Shah and N. L. Allbritton, "Micro total analysis systems: fundamental advances and applications in the laboratory, clinic, and field," *Analytical Chemistry,* vol. 85, no. 2, pp. 451-472, 9 November 2012.

[6] P.-A. Auroux, D. Iossifidis, D. R. Reyes and A. Manz, "Micro total analysis systems. 2. Analytical standard operations and applications," *Analytical Chemistry,* vol. 74, no. 12, pp. 2637-2652, 15 June 2002.

[7] S. Haeberle and R. Zengerle, "Microfluidic platforms for lab-on-a-chip applications," *Lab on a Chip,* vol. 7, no. 9, pp. 1094-1110, September 2007.

[8] X. Xu, S. Zhang, H. Chen and J. Kong, "Integration of electrochemistry in micro-total analysis systems for biochemical assays: Recent developments," *Talanta,* vol. 80, no. 1, pp. 8-18, 15 November 2009.

[9] A. Arora, G. Simone, G. B. Salieb-Beugelaar, J. T. Kim and A. Manz, "Latest developments in micro total analysis systems," *Analytical Chemistry,* vol. 82, no. 12, pp. 4830-4847, June 2010.

[10] W. C. Nelson and C.-J. Kim, "Droplet actuation by electrowetting-on-dielectric (EWOD): a review," *Journal of Adhesion Science and Technology,* vol. 26, no. 12-17, pp. 1747-1771, 18 May 2012.

[11] D. Mark, S. Haeberle, G. Roth, F. v. Stetten and R. Zengerle, "Microfluidic lab-on-a-chip platforms: requirements, characteristics and applications," *Chemical Society Reviews,* vol.

39, no. 3, pp. 1153-1182, March 2010.

[12] J. Berthier, *Microdrops and digital microfluidics*, New York: William Andrew Publishing, 2008.

[13] P. Yager, T. Edwards, E. Fu, K. Helton, K. Nelson, M. R. Tam and B. H. Weigl, "Microfluidic diagnostic technologies for global public health," *Nature,* vol. 442, no. 2, pp. 412-418, 27 July 2006.

[14] V. Linder, "Microfluidics at the crossroad with point-of-care diagnostics," *Analyst,* vol. 132, no. 12, pp. 1186-1192, December 2007.

[15] R. Sista, Z. Hua, . P. Thwar, A. Sudarsan, V. Srinivasan and A. Eckhardt, "Development of a digital microfluidic platform for point of care testing," *Lab on a Chip,* vol. 8, no. 12, pp. 2091-2104, December 2008.

[16] J. Bergin, "Global biochip markets: microarrays and Lab-on-a-Chip," BCC Research, Wellesley, MA, USA, August 2011.

[17] MarketsandMarket, "Biochips market (DNA microarrays, Lab-on-Chip, protein microarrays, tissue & cell arrays) trends and global forecast (2010–2015)," MarketsandMarket, Dallas, TX, USA, August 2011.

[18] F. Su, K. Chakrabarty and R. B. Fair, "Microfluidics-based biochips: technology issues, implementation platforms, and design-automation challenges," *IEEE Transactions on Computer-Aided Design of Integrated Circuits and Systems,* vol. 25, no. 2, pp. 211-223, February 2006.

[19] T. Thorsen, S. Maerkl and S. Quake, "Microfluidic large-scale integration," *Science,* vol. 298, no. 5593, pp. 580-584, October 2002.

[20] S. Mutlu, F. Svec, C. H. Mastrangelo, J. M. Fréchet and Y. B. Gianchandani, "Enhanced electro-osmosis pumping with liquid bridge and field effect flow rectification," in *Proceedings of IEEE MEMS 2004 Conference*, Maastricht, Netherlands, pp. 850-853, 25-29 January 2004.

[21] V. Srinivasan, V. K. Pamula and R. B. Fair, "An integrated digital microfluidic lab-on-a-chip for clinical diagnostics on human physiological fluids," *Lab on a Chip,* vol. 4, no. 4, pp. 310-315, April 2004.

[22] i. Solvas, X. Casadevall and A. deMello, "Droplet microfluidics: recent developments and future applications," *Chemical Communications,* vol. 47, no. 7, pp. 1936-1942, 21

February 2011.

[23] A. Huebner, S. Sharma, M. Srisa-Art, F. Hollfelder and J. B. Edel, "Microdroplets: a sea of applications?," *Lab on a Chip,* vol. 8, no. 8, pp. 1244-1254, August 2008.

[24] A. B. Theberge, F. Courtois, Y. Schaerli, M. Fischlechner, C. Abell, F. Hollfelder and W. T. Huck, "Microdroplets in microfluidics: an evolving platform for discoveries in chemistry and biology," *Angewandte Chemie International Edition,* vol. 49, no. 34, pp. 5846-5868, 9 August 2010.

[25] Y. Schaerli, R. C. Wootton, T. Robinson, V. Stein, C. Dunsby, M. A. Neil, P. M. French, A. J. demello, C. Abell and F. Hollfelder, "Continuous-flow polymerase chain reaction of single-copy DNA in microfluidic microdroplets," *Analytical Chemistry,* vol. 81, no. 1, pp. 302-306, 1 January 2009.

[26] P. S. Dittrich, M. Jahnz and P. Schwi, "A new embedded process for compartmentalized cell-free protein expression and on-line detection in microfluidic devices," *ChemBioChem,* vol. 6, no. 5, pp. 811-814, 13 April 2005.

[27] S. Gulati, V. Rouilly, X. Niu, J. Chappell, R. I. Kitney, J. B. Edel and P. S. Freemont, "Opportunities for microfluidic technologies in synthetic biology," *Journal of The Royal Society Interface,* vol. 6, no. 4, pp. S493-S506, 27 May 2009.

[28] A. Ben-Yakar, N. Chronis and H. Lu, "Microfluidics for the analysis of behavior, nerve regeneration, and neural cell biology in C. elegans," *Current Opinion in Neurobiology,* vol. 19, no. 5, pp. 561-567, October 2009.

[29] M. G. Pollack, R. B. Fair and A. D. Shenderov, "Electrowetting-based actuation of liquid droplets for microfluidic applications," *Applied Physics Letters,* vol. 77, no. 11, pp. 1725-1726, September 2000.

[30] S. K. Cho, S. K. Fan, H. Moon and C. J. Kim, "Toward digital microfluidic circuits: creating, transporting, cutting and merging liquid droplets by electrowetting-based actuation," in *Proceedings of The Fifteenth IEEE International Conference On Micro Electro Mechanical Systems (MEMS),* Las Vegas, NV, USA, pp. 32-52, 24 January 2002.

[31] T. B. Jones, M. Gunji, M. Washizu and M. J. Feldman, "Dielectrophoretic liquid actuation and nanodroplet formation," *Journal of Applied Physics,* vol. 89, no. 2, pp. 1441-1448, 1 February 2001.

[32] O. D. Velev, B. G. Prevo and K. H. Bhatt, "On-chip manipulation of free droplets,"

Nature, vol. 426, no. 6966, pp. 515-516, 4 December 2003.

[33] T. B. Jones, "More about the electromechanics of electrowetting," *Mechanics Research Communications,* vol. 36, no. 1, pp. 2-9, January 2009.

[34] T. B. Jones, "On the relationship of dielectrophoresis and electrowetting," *Langmuir,* vol. 18, no. 11, pp. 4437-4443, 3 May 2002.

[35] H. Lee, S. Yun, S. H. Ko and K. H. Kang, "An electrohydrodynamic flow in ac electrowetting," *Biomicrofluidics,* vol. 3, no. 4, p. 044113, December 2009.

[36] H. Moon, S. K. Cho, R. L. Garrell and C.-J. Kim, "Low voltage electrowetting-on-dielectric," *Journal of Applied Physics,* vol. 92, no. 7, pp. 4080-4087, October 2002.

[37] Y. Li, P. William, L. I. Haworth, A. Ross, J. Stevenson and A. J. Walton, "Room-temperature fabrication of anodic tantalum pentoxide for low-voltage electrowetting on dielectric (EWOD)," *Journal of Microelectromechanical Systems,* vol. 17, no. 6, pp. 1481-1488, December 2008.

[38] Y.-Y. Lin, R. D. Evans, E. Welch, B.-N. Hsu, A. C. Madison and R. B. Fair, "Low voltage electrowetting-on-dielectric platform using multi-layer insulators," *Sensors and Actuators B: Chemical,* vol. 150, no. 1, pp. 465-470, 21 September 2010.

[39] T. B. Jones, K.-L. Wang and D.-J. Yao, "Frequency-dependent electromechanics of aqueous liquids: electrowetting and dielectrophoresis," *Langmuir,* vol. 20, no. 7, pp. 2813-2818, 3 March 2004.

[40] S.-K. Fan, T.-H. Hsieh and D.-Y. Lin, "General digital microfluidic platform manipulating dielectric and conductive droplets by dielectrophoresis and electrowetting," *Lab on a Chip,* vol. 9, no. 9, pp. 1236-1242, 7 May 2009.

[41] W. Wang and T. B. Jones, "Microfluidic actuation of insulating liquid droplets in a parallel-plate device," *Journal of Physics: Conference Series,* vol. 301, no. 1, p. 012057, 23 June 2011.

[42] J.-H. Lee, "Microactuation by continuous electrowetting and electrowetting: Theory, fabrication, and demonstration," Doctoral dissertation, University of California, Los Angeles, USA, 2000.

[43] J. Lee, H. Moon, J. Fowler, T. Schoellhammer and C.-J. Kim, "Electrowetting and electrowetting-on-dielectric for microscale liquid handling," *Sensors and Actuators A: Physical,* vol. 95, no. 2, pp. 259-268, 1 January 2002.

[44] M. J. Jebrail and A. R. Wheeler, "Let's get digital: digitizing chemical biology with microfluidics," *Current Opinion in Chemical Biology,* vol. 14, no. 5, pp. 574-581, October 2010.

[45] Z. Hua, J. L. Rouse, A. E. Eckhardt, V. Srinivasan, V. K. Pamula, W. A. Schell, J. L. Benton, T. G. Mitchell and M. G. Pollack, "Multiplexed real-time polymerase chain reaction on a digital microfluidic platform," *Analytical Chemistry,* vol. 82, no. 6, pp. 2310-2316, 12 February 2010.

[46] M. Hedström, I. Y. Galaev and B. Mattiasso, "Continuous measurements of a binding reaction using a capacitive biosensor," *Biosensors and Bioelectronics,* vol. 21, no. 1, pp. 41-48, 15 July 2005.

[47] T. Taniguchi, T. Torii and T. Higuchi, "Chemical reactions in microdroplets by electrostatic manipulation of droplets in liquid media," *Lab on a Chip,* vol. 2, no. 1, pp. 19-23, January 2002.

[48] V. N. Luk and A. R. Wheeler, "A digital microfluidic approach to proteomic sample processing," *Analytical Chemistry,* vol. 81, no. 11, pp. 4524-4530, 6 May 2009.

[49] M. J. Jebrail and A. R. Wheeler, "Digital microfluidic method for protein extraction by precipitation," *Analytical Chemistry,* vol. 81, no. 1, pp. 330-335, 4 December 2008.

[50] R. S. Sista, A. E. Eckhardt, V. Srinivasan, M. G. Pollack, S. Palanki and V. K. Pamula, "Heterogeneous immunoassays using magnetic beads on a digital microfluidic platform," *Lab on a Chip,* vol. 8, no. 12, pp. 2188-2196, December 2008.

[51] I. Barbulovic-Nad, H. Yang, P. S. Park and A. R. Wheeler, "Digital microfluidics for cell-based assays," *Lab on a Chip,* vol. 8, no. 4, pp. 519-526, April 2008.

[52] J. Zhou, L. Lu, K. Byrapogu, D. M. Wootton, P. I. Lelkes and R. Fair, "Electrowetting-based multi-microfluidics array printing of high resolution tissue construct with embedded cells and growth factors," *Virtual and Physical Prototyping,* vol. 2, no. 4, pp. 217-223, December 2007.

[53] M. G. Pollack, A. Shenderov and R. Fair, "Electrowetting-based actuation of droplets for integrated microfluidics," *Lab on a Chip,* vol. 2, pp. 96-101, 2002.

[54] M. G. Pollack, "Electrowetting-based microactuation of droplets for digital microfluidics," Doctoral dissertation, Duke University, 2001.

[55] G. M. Whitesides, "The origins and the future of microfluidics," *Nature,* vol. 442, no.

7101, pp. 368-373, 27 July 2006.

[56] L. Malic, D. Brassard, T. Veres and . M. Tabrizian, "Integration and detection of biochemical assays in digital microfluidic LOC devices," *Lab-on-a-Chip,* vol. 10, no. 4, pp. 418-431, 21 February 2010.

[57] I. Kuon, R. Tessier and J. Rose, "FPGA architecture: survey and challenges," *Foundations and Trends in Electronic Design Automation,* vol. 2, no. 2, pp. 135-253, April 2008.

[58] S. Trimberger, "Field-programmable gate array technology," Xilinx, San Jose, CA, USA, 1994.

[59] H. Morgan, B. Hadwen, G. Broder, D. Morganti, A. Jacobs, C. Brown, Y. Kubota and J. Hector, "Programmable large area digital microfluidic array with integrated droplet sensing for bioassays," *Lab on a Chip,* vol. 12, no. 18, pp. 3305-3313, 21 September 2012.

[60] J. N. Israelachvili, *Intermolecular and surface forces*: revised third edition, Waltham, MA: Academic Press, 2011.

[61] S. Cho, H. Moon and C. Kim, "Creating, transporting, cutting, and merging liquid droplets by electrowetting-based actuation for digital microfluidic circuits," *Journal of Microelectromechnical Systems,* vol. 12, no. 1, pp. 70-80, February 2003.

[62] B. Berge, "Electrocapillarité et mouillage de films isolants par l'eau," *Comptes rendus de l'Académie des sciences. Série 2, Mécanique, Physique, Chimie, Sciences de l'univers, Sciences de la Terre,* vol. 317, no. 2, pp. 157-163, 1993.

[63] H. Dahms, "Electrocapillary measurements at the interface insulator-electrolytic solution," *Journal of The Electrochemical Society,* vol. 116, no. 11, pp. 1532-1534, November 1969.

[64] M. Lippmann, "Relations entre les phénomènes électriques et capillaires," *Annales de Chimie et de Physique,* vol. 5, no. 11, pp. 494-549, 1875.

[65] A. G. Papathanasiou and A. G. Boudouvis, "Manifestation of the connection between dielectric breakdown strength and contact angle saturation in electrowetting," *Applied Physics Letters,* vol. 86, no. 16, pp. 164102-164102, April 2005.

[66] K. H. Kang and I. S. Kang, "Validity of the Derjaguin approximation on electrostatic effect in the Frumkin-Derjaguin approach," *Langmuir,* vol. 19, no. 23, pp. 9962-9967, 31 October 2003.

[67] E. Baird, P. Young and K. Mohseni, "Electrostatic force calculation for an EWOD-

actuated droplet," *Microfluid Nanofluid,* vol. 3, no. 6, pp. 635-644, January 2007.

[68] J. Berthier, P. Dubois, P. Clementz, P. Claustre, C. Peponnet and Y. Fouillet, "Actuation potentials and capillary forces in electrowetting based microsystems," *Sensors and Actuators A: Physical,* vol. 134, no. 2, pp. 471-479, 15 March 2007.

[69] R. Bavière, J. Boutet and Y. Fouillet, "Dynamics of droplet transport induced by electrowetting actuation," *Microfluid Nanofluid,* vol. 4, no. 4, pp. 287-294, April 2008.

[70] F. Mügele and J.-C. Baret, "Electrowetting: from basics to applications," *Journal of Physics: Condensed Matter,* vol. 17, no. 28, pp. R705-R774, 20 July 2005.

[71] T. Jones, J. Fowler, Y. S. Chang and C.-J. Kim, "Frequency-based relationship of electrowetting and dielectrophoretic liquid microactuation," *Langmuir,* vol. 19, pp. 7646-7651, 26 July 2003.

[72] J. Berthier, P. Clementz, J. M. Roux, Y. Fouillet and C. Peponnet, "Modeling microdrop motion between covered and open regions of EWOD microsystems," in *Proceedings of the 2006 Nanotech Conference*, Boston, USA, pp. 685-688, 20-24 June 2006.

[73] G. Wang, D. Teng and S.-K. Fan, "Three-dimensional digital microfluidics and applications," in *Proceedings of the 2012 7th IEEE International Conference on Nano/Micro Engineered and Molecular Systems (NEMS)*, Kyoto, Japan, pp. 415-418, 5-8 March 2012.

[74] P. M. Young and K. Mohseni, "Calculation of DEP and EWOD forces for application in digital microfluidics," *ASME Journal of Fluids Engineering,* vol. 130, no. 8, p. 081603, August 2008.

[75] N. Kumari, V. Bahadur and S. Garimella, "Electrical actuation of electrically conducting and insulating droplets using ac and dc voltages," *Journal of Micromechanics and Microengineering,* vol. 18, no. 10, p. 105015, October 2008.

[76] V. Bahadur and S. V. Garimella, "An energy-based model for electrowetting-induced droplet actuation," *Journal of Micromechanics and Microengineering,* vol. 16, no. 8, pp. 1494-1503, June 2006.

[77] D. Chatterjee, H. Shepherd and R. L. Garrell, "Electromechanical model for actuating liquids in a two-plate droplet microfluidic device," *Lab on a Chip,* vol. 9, no. 9, pp. 1219-1229, 7 May 2009.

[78] J. Zeng and T. Korsmeyer, "Principles of droplet electrohydrodynamics for lab-on-a-chip,"

Lab on a Chip, vol. 4, no. 4, pp. 265-277, April 2004.

[79] T. Jones, "An electromechanical interpretation of electrowetting," *Journal of Micromechanics and Microengineering,* vol. 15, no. 6, pp. 1184-1187, 22 April 2005.

[80] H. J. J. Verheijen and M. W. J. Prins, "Reversible electrowetting and trapping of charge: model and experiments," *Langmuir,* vol. 15, no. 20, pp. 6616-6620, 9 September 1999.

[81] S. K. Cho, Y. Zhao and C.-J. Kim, "Concentration and binary separation of micro particles for droplet-based digital microfluidics," *Lab on a Chip,* vol. 7, no. 4, pp. 490-498, April 2007.

[82] S.-K. Fan, P.-W. Huang, , T.-T. Wang and Y.-H. Peng, "Cross-scale electric manipulations of cells and droplets by frequency-modulated dielectrophoresis and electrowetting," *Lab on a Chip,* vol. 8, no. 8, pp. 1325-1331, August 2008.

[83] D. Janasek, J. Franzke and A. Manz, "Scaling and the design of miniaturized chemical-analysis systems," *Nature,* vol. 442, no. 7101, pp. 374-380, 27 July 2006.

[84] Y. Liu, H. Lee, R. M. Westervelt and D. Ham, "CMOS-based magnetic cell manipulation system," in *CMOS Biotechnology*, New York, Springer US, 2007, pp. 103-144.

[85] J. Takagi, M. Yamada, M. Yasuda and M. Seki, "Continuous particle separation in a microchannel having asymmetrically arranged multiple branches," *Lab on a Chip,* vol. 5, no. 7, pp. 778-784, July 2005.

[86] L. R. Huang, E. C. Cox, R. H. Austin and J. C. Sturm, "Continuous particle separation through deterministic lateral displacement," *Science,* vol. 304, no. 5673, pp. 987-990, 14 May 2004.

[87] R. B. Fair, "Digital microfluidics: is a true lab-on-a-chip possible?," *Microfluid Nanofluid,* vol. 3, no. 3, pp. 245-281, 8 March 2007.

[88] U.-C. Yi and C.-J. Kim, "Characterization of electrowetting actuation on addressable single-side coplanar electrodes," *Journal of Micromechanics and Microengineering,* vol. 16, no. 10, pp. 2053-2059, 25 August 2006.

[89] J. Fowler, H. Moon and C.-J. Kim, "Enhancement of mixing by droplet-based microfluidics in micro electro mechanical systems," in *Proceedings of The Fifteenth IEEE International Conference on Micro Electro Mechanical Systems (MEMS)*, Las Vegas, NV, USA, pp. 97-100, 24 January 2002.

[90] G. Wang, D. Teng and S.-K. Fan, "Digital microfluidic operations on microelectrode dot array architecture," *IET Nanobiotechnology,* vol. 5, no. 4, pp. 152-160, December 2011.

[91] C. Yi, Q. Zhang, C.-W. Li, J. Yang, J. Zhao and M. Yang, "Optical and electrochemical detection techniques for cell-based microfluidic systems," *Analytical and Bioanalytical Chemistry,* vol. 384, no. 6, pp. 1259-1268, 21 February 2006.

[92] F. B. Myers and L. P. Lee, "Innovations in optical microfluidic technologies for point-of-care diagnostics," *Lab on a Chip,* vol. 8, no. 12, pp. 2015-2031, December 2008.

[93] B. Kuswandi, J. Huskens and W. Verboom, "Optical sensing systems for microfluidic devices: a review," *Analytica Chimica Acta,* vol. 601, no. 2, pp. 141-155, 10 October 2007.

[94] J. Homola, "Surface plasmon resonance sensors for detection of chemical and biological species," *Chemical Reviews,* vol. 108, no. 2, pp. 462-493, 30 January 2008.

[95] X. D. Hoa, A. G. Kirk and M. Tabrizian, "Towards integrated and sensitive surface plasmon resonance biosensors: a review of recent progress," *Biosensors and Bioelectronics,* vol. 23, no. 2, pp. 151-160, 30 September 2007.

[96] D. Figeys, G. A. Schultz and D. Knapp, *Miniaturization and mass spectrometry,* S. L. Gac and A. v. d. Berg, Eds., Royal Society of Chemistry, 2009.

[97] S.-W. Wang and M. S.-C. Lu, "CMOS capacitive sensors with sub-μm microelectrodes for biosensing applications," *IEEE Sensors Journal,* vol. 10, no. 5, pp. 991-996, May 2010.

[98] A. Numnuam, P. Kanatharana, B. Mattiasson, P. Asawatreratanakul, B. Wongkittisuksa, C. Limsakul and P. Thavarungkul, "Capacitive biosensor for quantification of trace amounts of DNA," *Biosensors and Bioelectronics,* vol. 24, no. 8, pp. 2559-2565, 15 April 2009.

[99] C. Stagni, C. Guiducci, L. Benini, B. Riccò, S. Carrara, B. Samorí, C. Paulus, M. Schienle, M. Augustyniak and R. Thewes, "CMOS DNA sensor array with integrated A/D conversion based on label-free capacitance measurement," *IEEE Journal of Solid-State Circuits,* vol. 41, no. 12, pp. 2956-2964, December 2006.

[100] C. A. Betty, R. Lal, J. V. Yakhmi and S. K. Kuls, "Time response and stability of porous silicon capacitive immunosensors," *Biosensors and Bioelectronics,* vol. 22, no. 6, pp. 1027-1033, 15 January 2007.

[101] S. Loyprasert, P. Thavarungkul, P. Asawatreratanakul, B. Wongkittisuksa, C. Limsakul and P. Kanatharana, "Label-free capacitive immunosensor for microcystin-LR using self-assembled thiourea monolayer incorporated with Ag nanoparticles on gold electrode,"

Biosensors and Bioelectronics, vol. 24, no. 1, pp. 78-86, 15 September 2008.

[102] S. B. Prakash and P. Abshire, "On-chip capacitance sensing for cell monitoring applications," *On-Chip Capacita IEEE Sensors Journal,* vol. 7, no. 3, pp. 440-447, March 2007.

[103] A. Romani, N. Manaresi, L. Marzocchi, G. Medo, A. Leonardi, L. Altomare, M. Tartagni and R. Guerrieri, "Capacitive sensor array for localization of bioparticles in CMOS lab-on-a-chip," in *Proceedings of the 2004 IEEE International Solid-State Circuits Conference - ISSCC 2004,* San Francisco, CA, USA, pp. 224-225, 15-19 February 2004.

[104] Y. Li, Y. Mita, L. I. Haworth, W. Parkes, M. Kubota and A. J. Walton, "Test structure for characterizing low voltage coplanar EWOD system," *IEEE Transactions on Semiconductor Manufacturing,* vol. 22, no. 1, pp. 88-95, February 2009.

[105] K. Choi, A. H. Ng, R. Fobel and A. R. Wheeler, "Digital microfluidics," *Annual Review of Analytical Chemistry,* vol. 5, pp. 413-440, July 2012.

[106] P. Y. Paik, V. K. Pamula and K. Chakrabarty, "A digital-microfluidic approach to chip cooling," *Design & Test of Computers, IEEE,* vol. 25, no. 4, pp. 372-381, July 2008.

[107] F. Krogmann, W. Mönch and H. Zappe, "A MEMS-based variable micro-lens system," *Journal of Optics A: Pure and Applied Optics,* vol. 8, no. 7, pp. S330-S336, July 2006.

[108] Y.-Y. Lin, C.-W. Lin, L.-J. Yang and A.-B. Wang, "Micro-viscometer based on electrowetting on dielectric," *Electrochimica Acta,* vol. 52, no. 8, pp. 2876-2883, 10 February 2007.

[109] I. Moon and J. Kim, "Using EWOD (electrowetting-on-dielectric) actuation in a micro conveyor system," *Sensors and Actuators A: Physical,* vol. 130, pp. 537-544, 14 August 2006.

[110] Y. Zhao and S. K. Cho, "Micro air bubble manipulation by electrowetting on dielectric (EWOD): transporting, splitting, merging and eliminating of bubbles," *Lab on a Chip,* vol. 7, no. 2, pp. 273-280, February 2007.

[111] V. Srinivasan, V. K. Pamula and R. B. Fair, "Droplet-based microfluidic lab-on-a-chip for glucose detection," *Analytica Chimica Acta,* vol. 507, no. 1, pp. 145-150, April 2004.

[112] V. K. Pamula, V. Srinivasan, H. Chakrapani, R. Fair and . E. J. Toone, "A droplet-based lab-on-a-chip for colorimetric detection of nitroaromatic explosives," in *Proceedings of the 18th IEEE International Conference on Micro Electro Mechanical Systems, MEMS 2005,*

Miami Beach, Florida, USA, pp. 722-725, 30 January-3 February 2005.

[113] E. M. Miller and A. R. Wheeler, "A digital microfluidic approach to homogeneous enzyme assays," *Analytical Chemistry,* vol. 80, no. 5, pp. 1614-1619, 26 January 2008.

[114] K. P. Nichols and H. J. Gardeniers, "A digital microfluidic system for the investigation of pre-steady-state enzyme kinetics using rapid quenching with MALDI-TOF mass spectrometry," *Analytical Chemistry,* vol. 79, no. 22, pp. 8699-8704, 23 October 2007.

[115] J. R. Millman, K. H. Bhatt, B. G. Prevo and O. D. Velev, "Anisotropic particle synthesis in dielectrophoretically controlled microdroplet reactors," *Nature Materials,* vol. 4, no. 1, pp. 98-102, January 2005.

[116] P. Dubois, G. Marchand, Y. Fouillet, J. Berthier, T. Douki, F. Hassine, S. Gmouh and M. Vaultier, "Ionic liquid droplet as e-microreactor," *Analytical Chemistry,* vol. 78, no. 14, pp. 4909-4917, 26 May 2006.

[117] E. Ghafar-Zadeh and M. Sawan, "Charge-based capacitive sensor array for CMOS-based laboratory-on-chip applications," *Sensors Journal, IEEE,* vol. 8, no. 4, pp. 325-332, April 2008.

[118] A. Bange, H. B. Halsall and W. R. Heineman, "Microfluidic immunosensor systems," *Biosensors and Bioelectronics,* vol. 20, no. 12, pp. 2488-2503, 15 June 2005.

[119] F. Ricci, G. Volpe, L. Micheli and G. Palleschi, "A review on novel developments and applications of immunosensors in food analysis," *Analytica Chimica Acta,* vol. 605, no. 2, pp. 111-129, 19 December 2007.

[120] H. Wang, Y. Liu, C. Liu, J. Huang, P. Yang and B. Liu, "Microfluidic chip-based aptasensor for amplified electrochemical detection of human thrombin," *Electrochemistry Communications,* vol. 12, no. 2, pp. 258-261, February 2010.

[121] Y. Ko, J. Maeng, Y. Ahn, S. Y. Hwang, N. Cho and S. Lee, "Microchip-based multiplex electro-immunosensing system for the detection of cancer biomarkers," *Electrophoresis,* vol. 29, no. 16, pp. 3466-3476, August 2008.

[122] S.-W. Wang, C.-H. Lin, Y.-S. Yang and M. S.-C. Lu, "A CMOS capacitive dopamine sensor with Sub-nM detection resolution," in *Proceedings of the 2009 IEEE Sensors Conference*, Christchurch, Canterbury, New Zealand, pp. 400-404, 25-28 October 2009.

[123] M. Abdelgawad, S. L. Freire, H. Yang and A. R. Wheeler, "All-terrain droplet actuation,"

Lab on a Chip, vol. 8, no. 5, pp. 672-677, May 2008.

[124] Y.-J. Liu, D.-J. Yao, H.-C. Lin, W.-Y. Chang and H.-Y. Chang, "DNA ligation of ultramicro volume using an EWOD microfluidic system with coplanar electrodes," *Journal of Micromechanics and Microengineering,* vol. 18, no. 4, p. 045017, April 2008.

[125] H.-C. Lin, Y.-J. Liu and D.-J. Yao, "Core—shell droplets for parallel DNA ligation of an ultra-micro volume using an EWOD microfluidic system," *Journal of Laboratory Automation,* vol. 15, no. 3, pp. 210-215, June 2010.

[126] L. Malic, T. Veres and M. Tabrizian, "Biochip functionalization using electrowetting-on-dielectric digital microfluidics for surface plasmon resonance imaging detection of DNA hybridization," *Biosensors and Bioelectronics,* vol. 24, no. 7, pp. 2218-2224, 15 March 2009.

[127] L. Malic, T. Veres and M. Tabrizian, "Nanostructured digital microfluidics for enhanced surface plasmon resonance imaging," *Biosensors and Bioelectronics,* vol. 26, no. 5, pp. 2053-2059, 15 January 2011.

[128] E. R. F. Welch, Y. Lin, A. Madison and R. B. Fair, "Picoliter DNA sequencing chemistry on an electrowetting-based digital microfluidic platform," *Biotechnology Journal,* vol. 6, no. 2, pp. 165-176, February 2011.

[129] E. Wulff-Burchfield, W. A. Schell, W. E. Eckhardt, M. G. Pollack, Z. Hua, J. L. Rouse and V. K. Pamula, "Microfluidic platform versus conventional real-time polymerase chain reaction for the detection of Mycoplasma pneumoniae in respiratory specimens," *Diagnostic Microbiology and Infectious Disease,* vol. 67, no. 1, pp. 22-29, May 2010.

[130] Y.-H. Chang, G.-B. Lee, F.-C. Huang, Y.-Y. Chen and J.-L. Lin, "Integrated polymerase chain reaction chips utilizing digital microfluidics," *Biomedical Microdevices,* vol. 8, no. 3, pp. 215-225, 20 May 2006.

[131] E. A. Ottesen, J. W. Hong, S. R. Quake and J. R. Leadbetter, "Microfluidic digital PCR enables multigene analysis of individual environmental bacteria," *Science,* vol. 314, no. 5804, pp. 1464-1467, 1 December 2006.

[132] P. S. Dittrich and A. Manz, "Lab-on-a-chip: microfluidics in drug discovery," *Nature Reviews Drug Discovery,* vol. 5, no. 3, pp. 210-218, March 2006.

[133] H. Moon, A. R. Wheeler, R. L. Garrell, J. A. Loo and C.-J. Kim, "An integrated digital microfluidic chip for multiplexed proteomic sample preparation and analysis by MALDI-

MS," *Lab on a Chip,* vol. 6, no. 9, pp. 1213-1219, September 2006.

[134] A. R. Wheeler, H. Moon, C. A. Bird, R. R. Ogorzalek Loo, C.-J. Kim, J. A. Loo and R. L. Garrell, "Digital microfluidics with in-line sample purification for proteomics analyses with MALDI-MS," *Analytical Chemistry,* vol. 77, no. 2, pp. 534-540, 17 December 2005.

[135] W. C. Nelson, I. Peng, G.-A. Lee, J. A. Loo, R. L. Garrell and C.-J. Kim, "Incubated protein reduction and digestion on an EWOD digital microfluidic chip for MALDI-MS," *Analytical Chemistry,* vol. 82, no. 23, pp. 9932-9937, 1 December 2010.

[136] M. Abdelgawad and A. R. Wheeler, "The digital revolution: a new paradigm for microfluidics," *Advanced Materials,* vol. 21, no. 8, pp. 920-925, 23 February 2009.

[137] G. J. Shah, J. L. Veale, Y. Korin, E. F. Reed, H. A. Gritsch and C.-J. Kim, "Specific binding and magnetic concentration of CD8+ T-lymphocytes on electrowetting-on-dielectric platform," *Biomicrofluidics,* vol. 4, no. 4, p. 044106, December 2010.

[138] G. J. Shah, A. T. Ohta, E. P.-Y. Chiou, M. C. Wu and C.-J. Kim, "EWOD-driven droplet microfluidic device integrated with optoelectronic tweezers as an automated platform for cellular isolation and analysis," *Lab on a Chip,* vol. 9, no. 12, pp. 1732-1739, 21 June 2009.

[139] G. Wang, D. Teng and S.-K. Fan, "Digital microfluidic operations on microelectrode array architecture," in *Proceedings of the 2011 IEEE International Conference on Nano/Micro Engineered and Molecular Systems (NEMS)*, Kaohsiung, Taiwan, pp. 1180-1183, 20-23 February 2011.

[140] A. Quinn, R. Sedev and J. Ralston, "Influence of the electrical double layer in electrowetting," *Journal of Physical Chemistry B,* vol. 107, no. 5, pp. 1163-1169, 8 January 2003.

[141] K. Chakrabarty and F. Su, "Design automation challenges for microfluidics-based biochips," in *Proceedings of the Design, Test, Integration and Packaging of MEMS/MOEMS (DTIP '05)*, Montreux, Switzerland, pp. 260-265, 01-03 June 2005.

[142] J. H. Song, R. Evans, Y. -Y. Lin, B. -N. Hsu and R. B. Fair, "A scaling model for electrowetting-on-dielectric microfluidic actuators," *Microfluid Nanofluid,* vol. 7, no. 1, pp. 75-89, 12 November 2008.

[143] L.-S. Jang, C.-Y. Hsu and C.-H. Chen, "Effect of electrode geometry on performance of EWOD device driven by battery-based system," *Biomedical Microdevices,* vol. 11, pp.

1029-1036, 29 May 2009.

[144] R.-F. Yue, J.-G. Wu, X.-F. Zeng, M. Kang and L.-T. Liu, "Demonstration of four fundamental operations of liquid droplets for digital microfluidic systems based on an electrowetting-on-dielectric actuator," *Chinese Physics Letters,* vol. 23, no. 8, pp. 2303-2306, August 2006.

[145] P. Zhao, Y. Li, X. Zeng, J. Zhou, Y. Huang and R. Liu, "EWOD using P(VDF-TrFE)," in *Proceedings of the 4th IEEE International Conference on Nano/Micro Engineered and Molecular Systems, NEMS 2009*, Shenzhen, China, pp. 202-205, 5-8 January 2009.

[146] K. Chakrabarty and F. Su, *Digital microfluidic biochips: synthesis, testing, and reconfiguration techniques*, Boca Raton: CRC Press, 2007.

[147] M. Cho and D. Z. Pan, "A high-performance droplet routing algorithm for digital microfluidic biochips," *IEEE Transactions on Computer-Aided Design of Integrated Circuits and Systems,* vol. 27, no. 10, pp. 1714-1724, October 2008.

[148] T.-W. Huang and T.-Y. Ho, "A fast routability-and performance-driven droplet routing algorithm for digital microfluidic biochips," in *Proceedings of the 2009 IEEE International Conference on Computer Design, ICCD 2009*, Lake Tahoe, CA, USA, pp. 445-450, 4-7 October 2009.

[149] K. F. Bohringer, "Towards optimal strategies for moving droplets in digital microfluidic systems," in *Proceedings of the 2004 IEEE International Conference on Robotics & Automation*, New Orleans, LA, USA, pp. 1468-1474, 26 April-1 May 2004.

[150] F. Su, W. Hwang and K. Chakrabarty, "Droplet routing in the synthesis of digital microfluidic biochips," in *Proceedings of the Design, Automation and Test in Europe, 2006. DATE '06*, Leuven, Belgium, pp. 1-6, 6-10 March 2006.

[151] Z. Chen, D. Teng, G. Wang and S.-K. Fan, "Droplet routing in high-level synthesis of configurable digital microfluidic biochips based on microelectrode dot array architecture," *BioChip Journal,* vol. 5, no. 4, pp. 343-352, 20 December 2011.

[152] H. Yang, V. N. Luk, M. Abelgawad, I. Barbulovic-Nad and A. R. Wheeler, "A world-to-chip interface for digital microfluidics," *Analytical Chemistry,* vol. 81, no. 3, pp. 1061-1067, 30 December 2008.

[153] T. Grotjohn and B. Hoefflinger, "A parametric short-channel MOS transistor model for subthreshold and strong inversion current," *Solid-State Circuits, IEEE Journal,* vol. 19, no.

1, pp. 100-112, February 1984.

[154] K. Roy, S. Mukhopadhyay and H. Mahmoodi-Meimand, "Leakage current mechanisms and leakage reduction techniques in deep-submicrometer CMOS circuits," *Proceedings of the IEEE,* vol. 91, no. 2, pp. 305-327, February 2003.

[155] Z. Parpia, C. A. T. Salama and R. A. Hadaway, "Modeling and characterization of CMOS-compatible high-voltage device structures," *IEEE Transactions on Electron Devices,* vol. 34, no. 11, pp. 2335-2343, November 1987.

[156] P. M. Santos, A. P. Casimiro, M. Lanca and M. C. Simas, "CMOS compatible HV gate-shifted LDD-NMOS," *IEEE Transactions on Electron Devices,* vol. 48, no. 5, pp. 1013-1015, May 2001.

[157] R. B. Fair, A. Khlystov, T. D. Tailor, V. Ivanov, R. D. Evans, P. B. Griffin, V. Srinivasan, V. K. Pamula, M. G. Pollack and J. Zhou, "Chemical and biological applications of digital-microfluidic devices," *Design & Test of Computers, IEEE,* vol. 24, no. 1, pp. 10-24, February 2007.

[158] J. A. Geen, S. J. Sherman, J. F. Chang and S. R. Lewis, "Single-chip surface micromachined integrated gyroscope with 50/h Allan deviation," *IEEE Journal of Solid-State Circuits,* vol. 37, no. 12, pp. 1860-1866, December 2002.

[159] J. Berthier, P. Clementz, O. Raccurt, D. Jary, P. Claustre, C. Peponnet and Y. Fouillet, "Computer aided design of an EWOD microdevice," *Sensors and Actuators A: Physical,* vol. 127, no. 2, pp. 283-294, March 2006.

APPENDIX A. THREE-DIMENSIONAL DIGITAL MICROFLUIDICS AND APPLICATIONS

Droplet delivery system was discussed in Section 6.1.3. This appendix provides the details of the three-dimensional digital microfluidics and applications as published in [73].

Digital microfluidics, by the electrowetting-on-dielectric (EWOD), is a promising way to manipulate biological targets like DNA, proteins, or cells in very small liquid volumes. Conventionally, digital microfluidic operations are performed on a two-dimensional electrode array. This research expands the two-dimensional conventional digital microfluidic architecture into a three-dimensional architecture. The concept relies on the possibility that back and forth droplet motion between the open and covered region is possible under the EWOD actuation. Two face-to-face plates based on the "microelectrode dot array" (MEDA) architecture form the foundation of the two-layer microfluidic operations and a dual open/covered hybrid design adds the inter-layer microfluidic connection to complete the three-dimensional system. By combining the advantages of open/covered systems, a three-dimensional digital microfluidics may achieve better droplet routing capabilities and fit more functions into a given footprint.

A.1. Introduction

A three-dimensional digital microfluidic system that can perform microfluidic operations on stacked layers has many advantages over the two-dimensional systems. This research leverages the flexibility of the Microelectrode Dot Array (MEDA) architecture [90] and droplet motion between the covered and open region of EWOD microsystems [72] by extending the two-dimensional conventional digital microfluidic architecture into a three-dimensional architecture. In covered EWOD microsystems, droplets are confined between two plates. In open systems, the sessile droplet is sitting freely on a horizontal solid substrate. Each one of these systems has its own advantages. Droplet dispense, motion and slitting are easier in covered EWOD systems,

whereas mixing and evaporation are preferably performed in the open configuration [72, 159]. The three-dimensional architecture combines the advantages of the open and covered EWOD systems, a dual open/covered system.

A three-dimensional digital microfluidic system is fundamentally constructed by two face-to-face plates based on the MEDA architecture. Different physical arrangements of the two plates provide inter-plate connecting solutions for different applications. Two fundamental three-dimensional microfluidic systems are studied in this research. The first one is the "Dual-Layer System", which enables microfluidic operations on dual layers. As the complexity of the digital microfluidics-based "lab-on-a-chip" (LOC) systems is increasing, the droplet routing capability of the system has significant impact on its performance. This dual-layer system has better capabilities to route droplets to blocked locations or to avoid unwanted path contaminations. Naturally, more functions can also fit into a given footprint in a three-dimensional system.

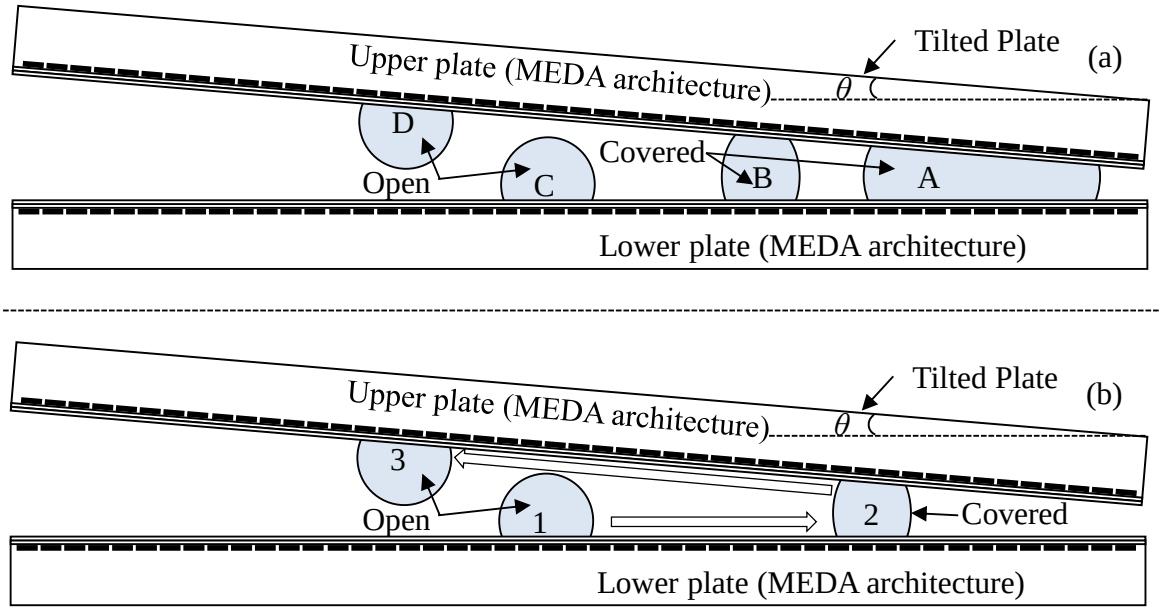

Figure A-1. Sketch of the dual-layer digital microfluidic system constructed by two face-to-face MEDA plates: (a) droplet B is created from reservoir A in the covered region and sessile droplets C & D (open) are formed by moving droplet B from the covered region to the open region.

The second three-dimensional microfluidic system is the “Inter-Chip Bridge”. This inter-chip bridge provides a viable modular LOC design solution before a monolithically integrated LOC can be achieved. In a modular system design, the LOC system can be partitioned into different function modules, which are then packaged together by the inter-chip bridge. This modular LOC system design has advantages in flexibility and reliability. Moreover, incompatible modules can be combined into a LOC microsystem for heterogeneous integration. Consequently, the microsystem can be optimized (technical or cost wise) to a much greater degree than if it were built on a single fabrication technology.

The rest of the paper is organized as follows. Section II covers the analytical model and the experiment results of the Dual-Layer System. The Inter-Chip Bridge is discussed in Section III, and, the conclusion of the study is in Section IV.

A.2. The Dual-Layer System

A.2.1. The System Structure and Microfluidic Operations

As illustrated in Figure A-1, a coplanar microelectrode array based on the MEDA architecture is designed as the bottom plate, and another MEDA coplanar microelectrode array is used as the top plate. The coplanar structure of the microelectrode array plus the tilted top plate that provides the flexible gap adjustment capability forms the three-dimensional microfluidic system.

The concept relies on the possibility that back and forth motion between the open and covered region is possible under the EWOD actuation. Microfluidic operations of the dual-layer system leverage the best of the dual open/covered hybrid design, where droplet transporting and mixing are performed on the open region of the stacked dual-layer system and droplet creation and cutting are performed at the closed region. As illustrated in Figure A-1(a), droplet B is created

from reservoir A under covered configuration. At the closed region, the MEDA architecture provides the flexibility of switching microfluidic actuations between the top and bottom plates. While the droplet actuation is on the top plate, the bottom plate is configured into a zero potential plate and vice versa. If the top-plate actuation of droplet B moves to the left, it will eventually result in a sessile droplet D by breaking up from the bottom plate when the gap is wide enough, as indicated in Figure A-1(a). Similarly, a bottom-plate actuation will result in a sessile droplet C on the bottom plate. A coplanar actuation of the sessile droplet is then provided to move the sessile droplet around. The inter-layer connection is illustrated as the droplet motion from position 1 (open) through position 2 (closed) into position 3 (open), as shown in Figure A-1(b). The MEDA architecture allows dynamic configurations and activations of the identical basic microfluidic unit called the "microelectrode cells" to actuate the droplets. This architecture has flexibilities in performing open (coplanar) and closed (top or bottom) actuations that take into consideration the droplet sizes and overall system integration variables.

The tilted angle (θ) of the top plate can be one dimensional or two dimensional. If it is one dimensional, the gap differences are only along one axis (x- or y-axis), whereas, if it is two dimensional, both the x-axis and y-axis have different gaps. To simplify the analysis, one dimensional tilting was used in our studies.

A.2.2. Analytical Model of The Dual-Layer System

For the dual-layer system, there are two directions of droplet motion between the open region and the closed region. As illustrated in Figure A-2, the first motion is from the covered region to the open region. Suppose that the droplet starts from the closed region by actuating electrodes toward the left side as shown in Figure A-2(a). When the droplet has reached the point where the

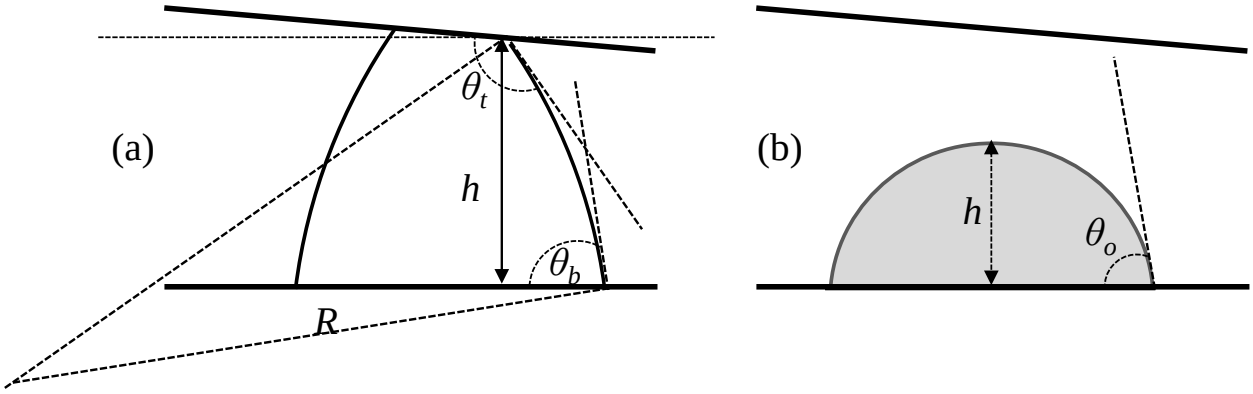

Figure A-2. Droplet motion from (a) the closed region to (b) the open region.

droplet internal pressure of Figure A-2(a) is greater than Figure A-2(b), the droplet breaks up from the top plate and becomes a sessile droplet in the open region.

To simplify our analysis, the covered droplet pressure is approximated by removing the tilted angle. Due to a small Bond number and the flat top and bottom surfaces, the profile of the droplet is nearly a spherical cap. From this, we can derive a formulation for the calculation of the volume of the droplet. Droplet pressure in each region can be calculated by using Laplace's law. First, for a droplet of volume *V*, confined between two horizontal plates separated by a distance *h*, internal pressure is given by [12]

$$P_c = \gamma\left(\frac{-\cos\theta_t - \cos\theta_b}{h} + \sqrt{\frac{\pi h}{V}}\right), \tag{A-1}$$

where θ_t and θ_b are the contact angles with the top and bottom plates and γ the surface tension in the covered and the open regions. In (B.1), the right hand side relates to the curvature *R*, and the horizontal curvature. For a sessile drop of the same volume, using Laplace's law, the droplet pressure is given by [12]

$$P_o = 2\gamma\left(\frac{3V}{\pi(2 - 3\cos\theta_o + \cos^3\theta_o)}\right)^{-\frac{1}{3}}, \tag{A-2}$$

where θ_o is the contact angle with the bottom plates. The condition for the motion from the covered to the open region is

$$P_{\text{covered,actuated}} > P_{\text{open,actuated}}. \quad \text{(A-3)}$$

Let θ_a be the actuated contact angle and θ_n the open (non-actuated contact angle), so that

$$P_c(\theta_t = \theta_n, \theta_b = \theta_a) - P_o(\theta_o = \theta_a) \geq 0 \text{ and} \quad \text{(A-4)}$$

$$\gamma\left(\frac{-\cos\theta_n - \cos\theta_a}{h} + \sqrt{\frac{\pi h}{V}}\right) - 2\gamma\left(\frac{3V}{\pi(2 - 3\cos\theta_a + \cos^3\theta_a)}\right)^{-\frac{1}{3}} \geq 0\,. \quad \text{(A-5)}$$

The second motion is from the open region to the covered region. When the droplet motion moving towards the right as shown in Figure A-3(a) continues, the droplet touches the top plate, and the transition from the open region into the covered region can be easily completed. Also, as shown in Figure A-3(b), the de-actuation of the droplet could speed up the transition with increased height of the non-wetting sessile droplet. In the non-wetting case, the height of a sessile droplet is

$$h = R + Rcos(\pi - \theta_n) = R(1 - cos\,\theta_n). \quad \text{(A-6)}$$

A.2.3. Experimental Results of The Dual-Layer System

A number of prototypes are fabricated on ITO glasses to conduct experiments of the dual-layer system. The test system is shown in Figure A-4. Deionized (DI) water is used to form the

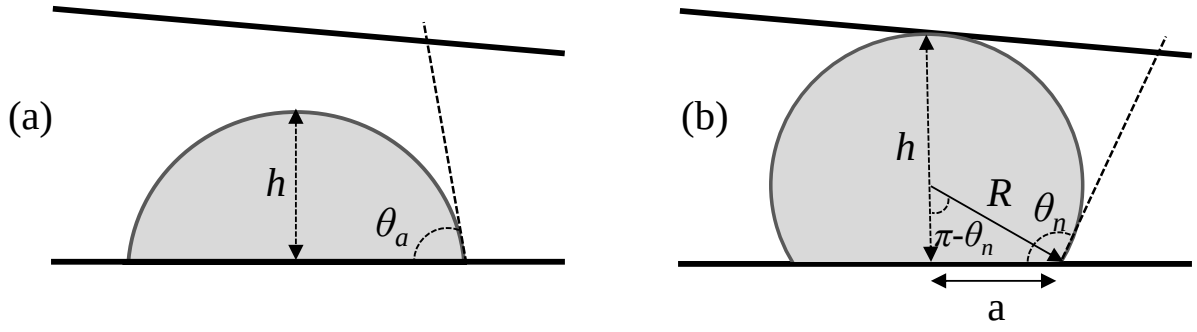

Figure A-3. Droplet motion from (a) the open region to (b) the closed region.

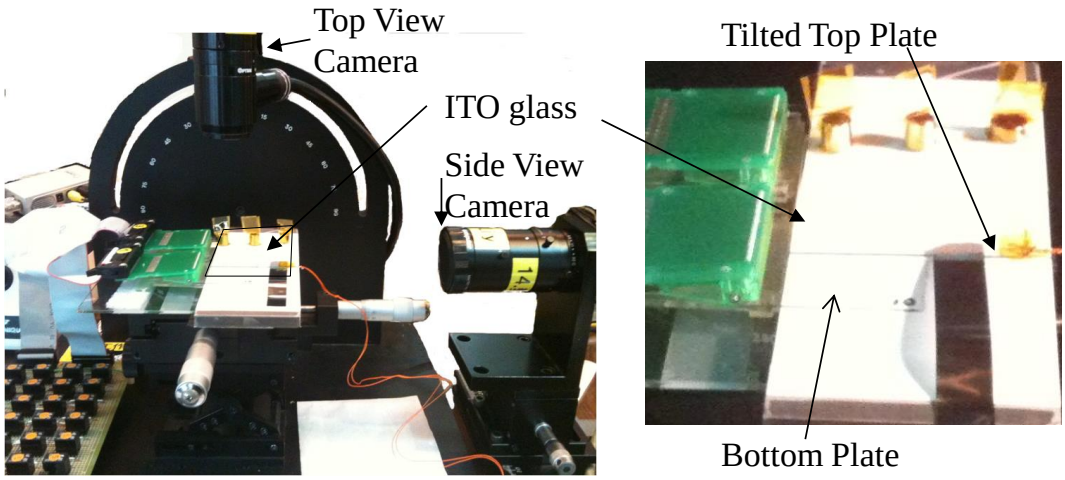

Figure A-4. The experiment setup for the dual-layer system.

droplet, and the air is the medium. The non-actuated contact angle is close to 115˚, and the electrode activating voltage was chosen so that the actuated contact angle is about 80˚.

Figure A-5 shows that the motion from the covered to the open region is possible. The lighter circle in Figure A-5(a) clearly shows the cross section on the top plate, and the dark outline indicates the cross section of the bottom plate. Figure A-5(b) and (e) show top view and side

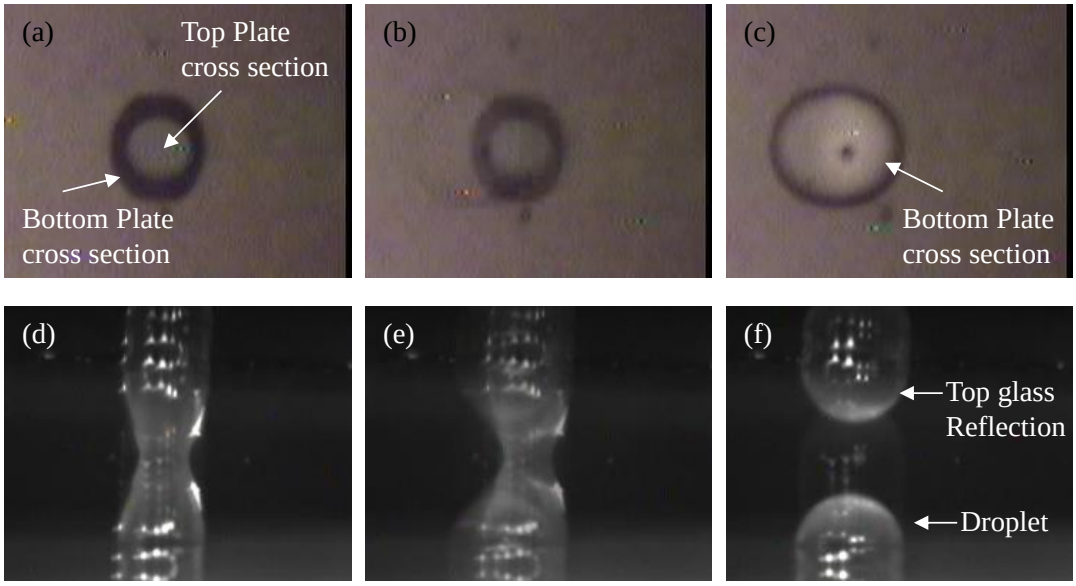

Figure A-5. From left to right, top and side experimental views show the droplet motion from the covered droplet into the open sessile droplet for the tested dual-layer system.

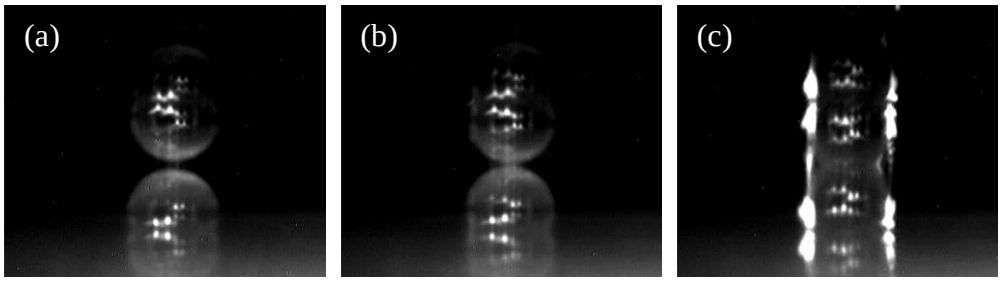

Figure A-6. From left to right, side experimental views show the droplet motion from the open sessile droplet into the covered droplet for the tested dual-layer system.

view of the moment before the breaking-up of the droplet from the top plate occurs. Figure A-5(c) and (f) illustrate the cross section and the side view of the sessile droplet.

From left to right as shown in Figure A-6, the side experimental views illustrate the droplet motion from the open sessile droplet into the covered droplet of the dual-layer system. Figure A-6(b) shows an actuated droplet that moved into the position where the top of the droplet almost touched the top plate. Then, the de-actuation made the droplet touch the top plate as shown in Figure A-6(c), and the droplet shifted into the covered region. The gap height is an important parameter of the motion. The gap height needed for the covered-to-open transition (*h* in Figure A-2(a)) is greater than the required height of the open-to-covered transition (*h* in Figure A-3(b)). Different droplet volumes also change the transition heights. To assure the smooth back-and-forth transitions between the covered and open regions, the MEDA architecture is leveraged to provide the flexibility of the droplet manipulations for varied transition positions between the covered and open regions.

A.3. The Inter-Chip Bridge

A.3.1. The System Structure and Microfluidic Operations

Another design of the three-dimensional structure is the inter-chip bridge. This design is based on the concept of the dual open/covered EWOD microsystem developed by Berthier et al.

[72]. It has been shown that back and forth motion between the open and covered region is possible under the EWOD actuation, even though it is closely related to the difference internal pressure of droplet between the covered and open regions. Droplet motion from the covered to the open region is not possible if the gap is too large relative to the droplet volume. Similarly, droplet motion from the open to the covered region is not possible if the gap is too small [12, 72].

In the inter-chip bridge system, droplet A moves from LOC #1 (open region) into the covered region formed by the bridge plate and LOC #1, which is illustrated as droplet B in Figure A-7. Then droplet B continues moving to the left into the open region on the bridge illustrated as droplet C. Again, droplet C moves into the covered region between the bridge plate and LOC #2 as droplet D. The droplet motion from position A on LOC #1 to position D on LOC #2 completes the inter-chip bridging function of a droplet. The most critical element of the inter-chip bridge design is the working range of the gap height in which the droplet motions in both directions are possible and the working range is sufficiently large so that there is enough room to build the system. To ensure the smooth inter-chip bridging operations, electrodes at the boundaries of the covered/open region must be specifically designed according to the liquid droplet volume. The flexibility of the field-programmability of electrodes in the MEDA architecture [90] is a great help in designing reliable and effective inter-chip bridges.

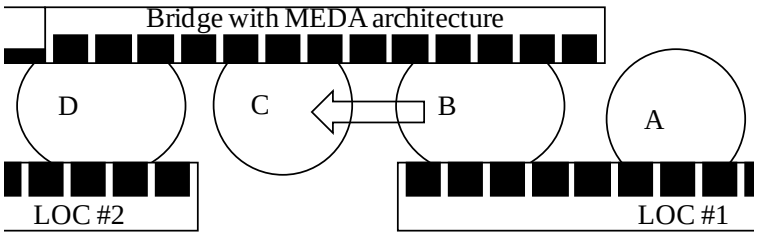

Figure A-7. Sketch of the inter-chip bridging based on the three-dimensional structure. The back and forth motion between the open and the covered region make it possible to transfer droplets from one LOC to another.

A.3.2. Analytical Model of The Inter-Chip Bridge

The motion from the open region to the covered region starts from de-actuating electrodes in the open region and actuating electrodes in the covered region. The droplet then moves towards the covered region. When it has crossed the boundary and is located in the covered region, the actuation is switched off. The actuation in the open region is then switched on, and the droplet moves back to the open region. The condition for the motion from the open to covered region is

$$P_o(\theta_o = \theta_n) - P_c(\theta_t = \theta_n, \theta_b = \theta_a) \geq 0, \tag{A-7}$$

and conversely, for the motion from covered to the open region

$$P_c(\theta_t = \theta_n, \theta_b = \theta_n) - P_o(\theta_o = \theta_a) \geq 0. \tag{A-8}$$

The motion from the open to the covered region derived from (B.1), (B.2) and (B.7) is

$$2\gamma\left(\frac{3V}{\pi(2-3\cos\theta_n+\cos^3\theta_n)}\right)^{-\frac{1}{3}} - \gamma\left(\frac{-\cos\theta_n-\cos\theta_a}{h}+\sqrt{\frac{\pi h}{V}}\right) \geq 0 \quad . \tag{A-9}$$

Also, the motion from the open to the covered region derived from (B.1), (B.2) and (B.8) is

$$\gamma\left(\frac{-\cos\theta_n-\cos\theta_n}{h}+\sqrt{\frac{\pi h}{V}}\right) - 2\gamma\left(\frac{3V}{\pi(2-3\cos\theta_a+\cos^3\theta_a)}\right)^{-\frac{1}{3}} \geq 0 \quad . \tag{A-10}$$

A.3.3. Experimental Results of the Inter-Chip Bridge

Experiments have been performed on prototypes fabricated from ITO glasses. For a droplet of DI-water in air, motion from the open to the covered region is possible if the gap in the covered region is large enough, and the motion from the covered to the open region is possible if the gap is small enough as shown in Figure A-8. The actuated contact angle θ_a is about 80˚. The contact angle at the top plate θ_t (115˚) is an important parameter of the motion. If the angle is below 90˚, the droplet will have difficulties exiting the covered region due to the hydrophilic grip on the top

Figure A-8. Experimental view of a droplet crossing the frontier between the covered region and the open region. The droplet can move on both directions.

plate, and if the angle is greater than 120˚, the hydrophobic repulsion will make the motion towards the covered region difficult [12]. A vertical distance of about 200 microns seems to work well for liquid drops of 0.03 to 0.05 μl on Teflon hydrophobic layer with electrodes of 600 μm × 600 μm. Our experiment data showed no droplet motion from the open to covered region when the gap height was below 120 μm, which is in line with Berthier's work. Also, when the gap is wider than 220 μm, the droplet started to have difficulty moving from the covered to open region. In comparison, Berthier's work showed that the gap could be 500 μm, and the motion from the covered to open region should be still working at θ_t = 115˚ [12]. The difference is caused by the actuation of the open region. A catena was used in the droplet motion study by Berthier as a zero potential contact for open EWOD systems. From a system integration point of view, a catena is difficult to implement in real inter-chip bridge applications, so the MEDA architecture is used to provide the dual open/covered droplet actuation capability for the system. The coplanar actuation is achieved by configuring half of the electrode on the bottom plate into the zero potential contact and half of the electrode as the actuating electrode. The reduced size of the actuating electrode would have less of a pulling force for the droplet.

A.4. Conclusions

The mechanism of this three-dimensional architecture is a combination of two face-to-face plates and carefully arranged gaps and electrodes. Two different three-dimensional digital

microfluidic systems are discussed in this research. The inter-chip bridge structure is useful in a wide range of applications in the modular LOC system design and the system integration of biochips. Nonetheless, it also has constraints in the gap height and the size of the droplet. The MEDA architecture can be leveraged to smooth the microfluidic operations and to minimize constraints. The dual-layer system with the tilted top plate provides the flexibility of adjusting the gap height and therefore has fewer constraints than the inter-chip bridge model. This dual-layer system has better capabilities to route droplets and has higher functional density in a given footprint.

Combinations of the two basic structures are possible and could be more powerful in constructing future LOC system structures and advanced multi-chip system integrations.

APPENDIX B. SUPPORTING DATA FOR THE RESEARCH

In this appendix, there are two groups of supporting data. The first group of data supports the proof-of-concept experiments including a summary of ITO glass prototypes (Table B-1) and calculations of effective lengths of contact lines (Figure B-1). The second group contains some numerical simulation results (Figure B-2 to B-6) for the discussions in Section 3.8.

Table B-1. Summary of the accomplished microfluidic experiments by the ITO glass prototypes of the MEDA architecture.

	Droplet	**Bi-planar & Gap**	**Co-planar & Gap**	**Creating**	**Transport**	**Cutting**	**Mixing**	**μFluidic operations**	**μ-Electrode Size**
T0	DI-AIR	80 μm			55 V			T/C	2×2 from 4×12
	DI-AIR	80 μm				55 V		T/C	4×2 from 4×12
	DI-AIR	80 μm			55 V			T/C	2×2 from 2×12
	DI-AIR	80 μm				55 V		T/C	2×2 from 2×12
T1	DI-AIR	100 μm			16 V, 20 V			Column	10×10
	DI-AIR	20 μm			40 V, 46 V			Column	(1,2,3)×10
	DI-AIR	60 μm			22-30 V			Column	1×10
	DI-OIL	80 μm			12-30 V			Column	(1,2,3,5)×10
T2	DI-AIR		No Cover		60 ,110 V			DC/T	10×10
	DI-AIR	100 μm		120 V				DC/T	10×10
	DI-AIR	100 μm			40-56 V			DC/T/C	10×10
	DI-AIR	100 μm				62 V		DC/T/C	10×10
	DI-AIR	20 μm		60 V				DC/T/C	10×10
	DI-AIR		80 μm		50, 54 V			T/C	10×10
	DI-AIR		80 μm			60 V		T/C	10×10
	DI-AIR	80 μm		40,54 V				DC/T/C	10×10
	R-AIR	80 μm		50 V				DC/T/C	10×10
T3	DI-AIR	100 μm		100 V				Catena	2×2
	DI-AIR	20 μm		48 V				Catena	2×2
T4	DI-AIR	20 μm			30-50 V			Diagonal	10×10
	DI-AIR	20 μm			44 V			Diagonal	10×10
	DI-AIR	40 μm				40, 44 V		Diagonal	10×10
T5	DI-AIR	100 μm			45 V			Bridging	10×10
	DI-AIR	20 μm			34 V			Bridging	10×10
T6	DI-AIR	80 μm		50-60 V				DC	3×3
	DI-AIR	40 μm		50 V				DC	3×3
	DI-AIR	20 μm		40-52 V				DC	3×3
	DI-AIR	20 μm		50 V		50 V		Aliquot	10×10
	DI-AIR	20 μm		50 V		50 V		Precise C	1×1

	DI-AIR		No Cover		50 V			CC	10×10
	DI-AIR		No Cover			70-160 V		CC	10×10
T7	DI-AIR	20 µm			40, 44 V			M	10×10
	DI-AIR	80 µm			40 V		44 V	M	10×10
	DI-AIR	20 µm					40 V	M	10×10
	DI-AIR	40 µm			44 V			M-S	10×10
	DI-AIR	80 µm			34,38 V			M-S Dis.	10×10
	DI-AIR	80 µm					44 V	De-shape	10×10
T8	DI-AIR	20 µm					44 V	Circular Uneven	3×3 4×10
	DI-AIR	80 µm					48 V	De-shape	10×10
T9	DI-AIR	80 µm				46 V		Column	(1,10)×10
	DI-OIL	80 µm			20-46 V			Column	1×10
	DI-OIL	80 µm			30-42 V			S-M-S	10×10
	DI-OIL	80 µm			34 V			Step-time	1×10
	DI-OIL	80 µm			10-34 V			Low V	10×10
	DI-OIL	80 µm			5-48 V			SM Low V	10×10
T10	DI-AIR	100 µm	No Cover		60 V			Bridging	Special
	DI-AIR	200 µm	No Cover		59 V			Bridging	Special
	DI-AIR	170 µm	No Cover		60 V			Bridging	Special
	DI-AIR	120 µm-220 µm	Cop -> Bip		55 V, 60 V			Cop<->Bip	Special
	DI-AIR	120 µm-220 µm	Bip->Cop		55 V, 60 V			Cop<->Bip	Special
	DI-AIR	Tilted	Open-> C		45 V, 55 V			C<->Open	Special
	DI-AIR	Tilted	C -> Open		45 V, 55 V			C<->Open	Special
T11	DI-AIR	80 µm					48 V	SAR	10×10
T12	DI-AIR	80 µm					56 V	SAR	10×10
T13	DI-AIR	20 µm			46 V, 48 V, 50 V			T	10×10
	DI-AIR	40 µm			46 V, 48 V, 50 V			T	10×10
	DI-AIR	80 µm			46 V, 48 V, 50 V			T	10×10
	DI-AIR	100 µm			46 V, 48 V, 50 V			T	10×10
T14	DI-AIR	80 µm			20 V, 40 V, 50 V			DC/T/C	Bi-state-switch Driver (Relay)
	DI-AIR	80 µm			10V, 20V, 40V			T	Bi-state-driver Driver (74HC125)

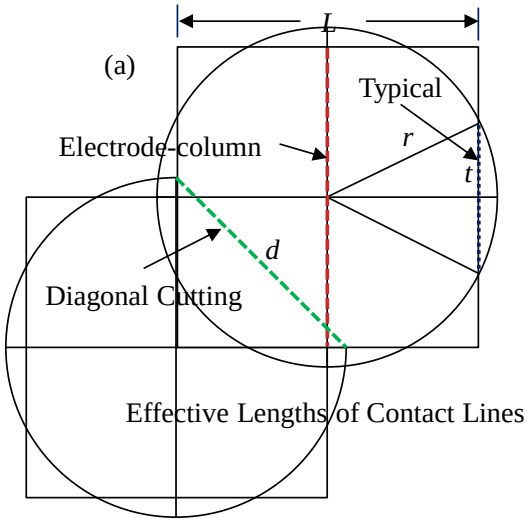

(b) $L^2 = \pi r^2$

$$\left(\frac{L}{2}\right)^2 + t^2 = r^2$$

$$t = \sqrt{\frac{4-\pi}{4\pi}}L$$

$$\frac{L}{2t} = \frac{1}{2\sqrt{\frac{4-\pi}{4\pi}}} = 1.913$$

(c) $d^2 = \sqrt{r^2 + r^2}$

$$d = \sqrt{2}r = \frac{\sqrt{2}}{\sqrt{\pi}}L$$

$$t = \sqrt{\frac{4-\pi}{4\pi}}L$$

$$\frac{d}{2t} = \frac{\sqrt{\frac{2}{\pi}}}{2\sqrt{\frac{4-\pi}{4\pi}}} = 1.526$$

Figure B-1. Calculations of effective lengths of contact lines for typical EWOD actuation, electrode-column actuation and diagonal cutting: (a) geometrical expressions of typical actuation 2*t*, diagonal cutting *d* and electrode-column actuation *L*; (b) calculation of *L*/2*t*; (c) calculation of *d*/2*t*.

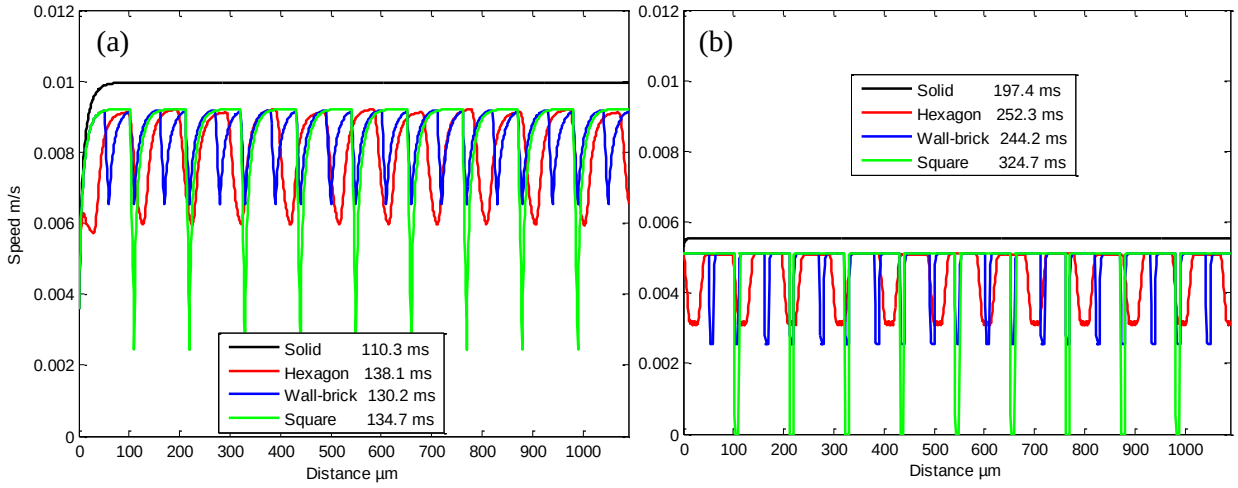

Figure B-2. Aspect ratio *d*/*L* impacts of the droplet motion performance (square droplet with *s*/*L* = 0.1): (a) *d*/*L* = 0.08; (b) *d*/*L* = 0.04.

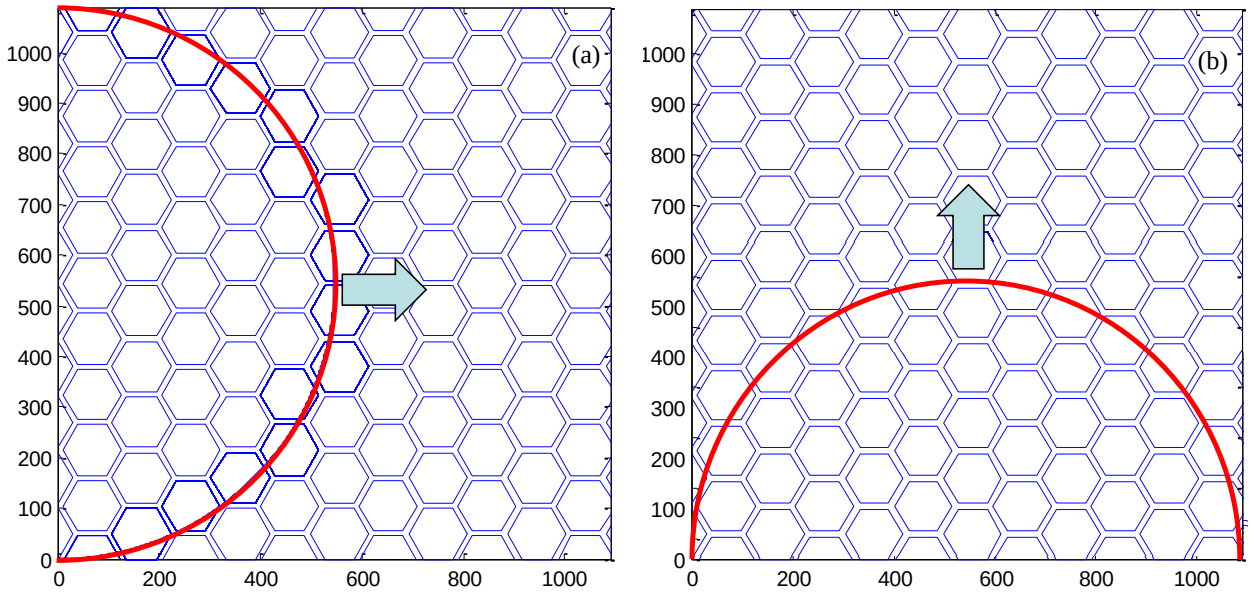

Figure B-3. Two different droplet motion directions have different actuation forces because of physical shape differences on the same hexagon CMA: (a) horizontal droplet motion; (b) vertical droplet motion.

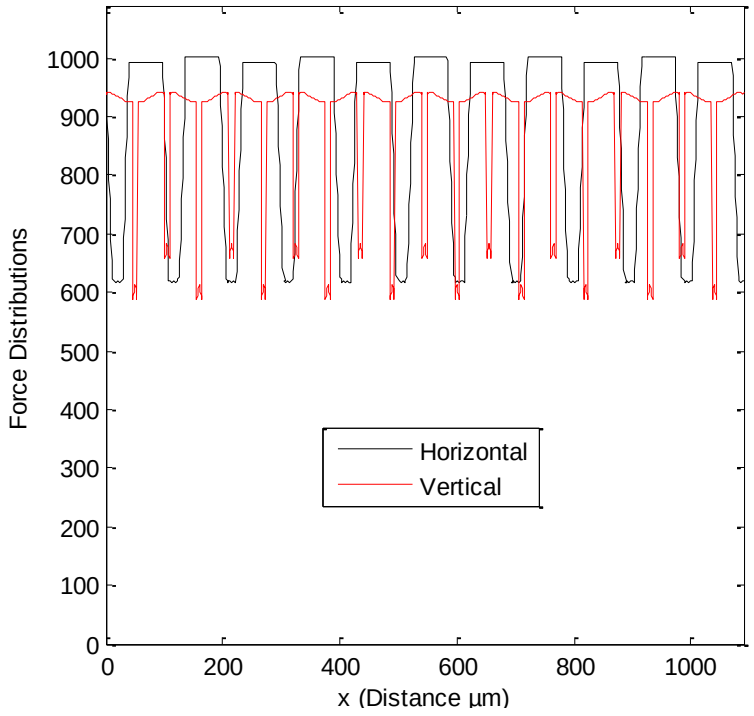

Figure B-4. Actuation force distributions of a square droplet moves in the horizontal direction and the vertical direction of the hexagon CMA.

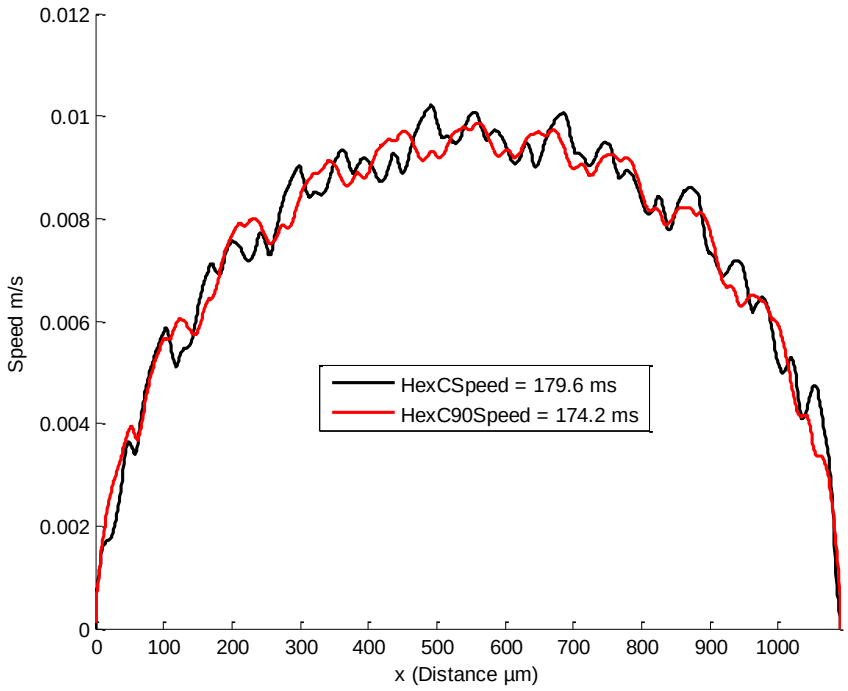

Figure B-5. The comparison of speed distributions of a circular droplet moves in the horizontal direction (HexC) and the vertical direction (HexC90) of the hexagon CMA.

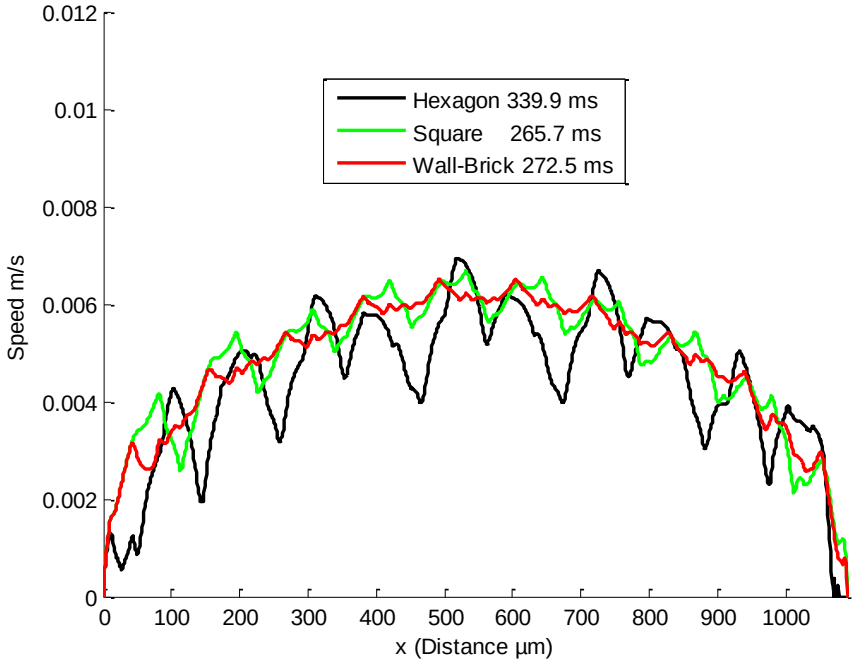

Figure B-6. Droplet motion simulations for s/L = 0.4. The hexagon CMA has significant degradation on the overall speed performance. This is in line with the prediction from Figure 3.15.